9-9-2015

The Nature and Frequency of Outflows from Stars in the Central Orion Nebula Cluster

C. R. O'Dell
Vanderbilt University

Gary J. Ferland
University of Kentucky, gary@uky.edu

W. J. Henney
Universidad Nacional Autónoma de México, Mexico

M. Peimbert
Universidad Nacional Autónoma de México, Mexico

Ma. T. García-Díaz
Universidad Nacional Autónoma de México, Mexico

See next page for additional authors

Notes/Citation Information
Published in *The Astrophysical Journal*, v. 150, no. 4, article 108, p. 1-63.

Digital Object Identifier (DOI)
https://doi.org/10.1088/0004-6256/150/4/108

The Astronomical Journal, 150:108 (63pp), 2015 October doi:10.1088/0004-6256/150/4/108

THE NATURE AND FREQUENCY OF OUTFLOWS FROM STARS IN THE CENTRAL ORION NEBULA CLUSTER*†

C. R. O'Dell[1], G. J. Ferland[2], W. J. Henney[3], M. Peimbert[4], Ma. T. García-Díaz[5], and Robert H. Rubin[6,7]
[1] Department of Physics and Astronomy, Vanderbilt University, Box 1807-B, Nashville, TN 37235, USA; cr.odell@vanderbilt.edu
[2] Department of Physics and Astronomy, University of Kentucky, Lexington, KY 40506, USA
[3] Instituto de Radioastronomía y Astrofísica, Universidad Nacional Autónoma de México, Apartado Postal 3-72, 58090 Morelia, Michoacán, México
[4] Instituto de Astronomia, Universidad Nacional Autónoma de México, Apdo, Postal 70-264, 04510 México D. F., México
[5] Instituto de Astronomia, Universidad Nacional Autónoma de México, Km 103 Carretera Tijuana-Ensenada, 22860 Ensenada, B.C., México
[6] NASA/Ames Research Center, Moffett Field, CA 94035-0001, USA
Received 2015 March 25; accepted 2015 July 29; published 2015 September 9

ABSTRACT

Recent *Hubble Space Telescope* images have allowed the determination with unprecedented accuracy of motions and changes of shocks within the inner Orion Nebula. These originate from collimated outflows from very young stars, some within the ionized portion of the nebula and others within the host molecular cloud. We have doubled the number of Herbig–Haro objects known within the inner Orion Nebula. We find that the best-known Herbig–Haro shocks originate from relatively few stars, with the optically visible X-ray source COUP 666 driving many of them. While some isolated shocks are driven by single collimated outflows, many groups of shocks are the result of a single stellar source having jets oriented in multiple directions at similar times. This explains the feature that shocks aligned in opposite directions in the plane of the sky are usually blueshifted because the redshifted outflows pass into the optically thick photon-dominated region behind the nebula. There are two regions from which optical outflows originate for which there are no candidate sources in the SIMBAD database.

Key words: H II regions – ISM: individual objects (Orion Nebula, NGC 1976, M42, Orion-South) – protoplanetary disks

1. BACKGROUND AND INTRODUCTION

The proximity of the Orion Nebula and its associated Orion Nebula Cluster (ONC) of young stars makes this the best test object for studying regions of massive star formation, examining the structure of the surrounding remaining gas and dust, and testing the assumptions made in the study of more distant H II regions. In the investigation reported on here, we give new and important information on the nebula and on the outflows from the low-mass stars belonging to the cluster.

The 3D structure of the Orion Nebula has been the subject or by-product of numerous studies, the most recent and thorough being those of O'Dell et al. (2008) and O'Dell & Harris (2010). Most of the emission comes from a relatively thin blister of ionized gas on the observer's side of the Orion Molecular Cloud. Since the radial velocity of the ionized gas becomes progressively more blueshifted with increasing ionization state (Zuckerman 1973; Balick et al. 1974), the ionizing source (θ^1 Ori C) must lie between the observer and the molecular cloud. This ionized gas decreases in density as it flows away from the main ionization front (MIF) and toward the observer. In the opposite direction, beyond the MIF, is a thin but high-density photon-dominated region (PDR). In the near foreground are layers of mostly neutral material known as the Veil (see van der Werf et al. 2013 and references therein), which reveals itself through H I absorption lines at 21 cm, its extinction of visible light (the Dark Bay to the east of the Trapezium asterism is the best exemplar), and spectroscopic absorption lines occurring from ultraviolet through radio wavelengths. The optically brightest part of the nebula is the nearly edge-on (Mesa-Delgado et al. 2011) ionization front enveloping a dense molecular cloud (Orion-S) that lies between the MIF and the foreground Veil. The dominant ionizing star θ^1 Ori C lies at the middle of the ONC of stars. Although Orion-S is likely to be a "free-floating" condensed structure (O'Dell & Harris 2010), it is currently impossible to rule out that it is a dense feature with an ionization shadow projecting away from θ^1 Ori C. This would be similar to the "Pillars of Creation" images in NGC 6611 except that in the Orion Nebula we view the pillar at a large angle with respect to the plane of the sky.

The existence of a new set of images of a major portion of the inner Orion Nebula at the highest resolution yet realized and the ability to astrometrically compare those images with some of the earliest images made with the *Hubble Space Telescope* (*HST*) presents the opportunity to determine motions and changes with unprecedented accuracy. Those data can be compared with the results of recent high-resolution radial velocity mapping of the same region. The access to these two sets of complementary data justifies a new study of the inner Orion Nebula.

1.1. Our Basic Approach

The images used in this program were made with the WFPC2 camera of the *HST* and its successor the WFC3 camera. The narrowband emission line filters F487N, F502N, F656N, F658N, and F673N are very similar in both cameras and isolate well emission from Hβ 486.1 nm, [O III] 500.7 nm, Hα 656.3 nm, [N II] 658.4 nm, and the [S II] doublet at 671.6 + 673.1 nm. The intermediate-width filter F547M is free of strong emission lines and is used less frequently. For convenience, we commonly indicate the signal in a filter by the name of the

* Based on observations with the NASA/ESA *Hubble Space Telescope*, obtained at the Space Telescope Science Institute, which is operated by the Association of Universities for Research in Astronomy, Inc., under NASA Contract No. NAS 5-26555.
† Based on observations at the San Pedro Martir Observatory operated by the Universidad Nacional Autónoma de México.
[7] Deceased.

filter, for example, the Hα image is simply called the F656N image and the ratio of the Hα to Hβ images (usually normalized so that each is near unity) as F656N/F487N. We denote as ratio images those that are the ratio of the signal from two filters. F656N/F487N is a good measure of the line-of-sight reddening. Since the Balmer lines originate from throughout any ionized zone, F502N/F487N (or F502N/F656N when the reddening does not vary significantly over the field of view [FOV]) is a good measure of the high-ionization gas, F658N/F656N is a good measure of the low-ionization gas, and F673N/F656N is a good measure of very low ionization gas lying very near an ionization front. F547M/F487N is a good measure of the relative strength of the nebular continuum to hydrogen line emission. Although we did not use Advanced Camera for Surveys (ACS) camera images in this study, they can be compared with those used here. It should be noted that the ACS filter designated as F658N passes both the Hα 656.3 nm and [N II] 658.4 nm lines and the ACS F660N filter isolates the [N II] 658.4 nm line.

The region studied in this investigation is shown in Figure 1. The primary source of new information is from the GO 12543 observations. The northern portion of this FOV was most useful and was extended to the east by using data from GO 5469 and GO 11038. We have added to the figure the positions of several well-known and well-studied Herbig–Haro objects. We have also shown the high-velocity jets identified by Doi et al. (2004) and strong features found in the low-velocity resolution study of the 1083 nm He I line by Takami et al. (2002). They are included here because Henney et al. (2007) established that these features are visible because they are Doppler shifted off the absorption core of this optically thick line.

The irregular structure shown with a thick black line and labeled H I is the H I 21 cm line absorption feature (van der Werf et al. 2013) associated with Orion-S.

A primary aim of this study is to determine the motion and changes of nebular features, jets, and shocks in emission lines. The methodology we use as a guide for identifying motions and changes is to divide an aligned first-epoch image by the aligned second-epoch image. We call this a motion image, and it has the characteristic that a single bright moving object will be dark in the direction of motion and light in the trailing direction. The opposite pattern will be seen in the case of a moving or changed dark object. A motion image will be of constant value of unity (since each image is normalized to unity), and only the moving and changed features will appear.

1.2. Nomenclature and Reference Numbers

Throughout this paper a number of designations, acronyms, and abbreviations will be used. Some are in common usage, and some are not. In this section we identify them.

Herbig–Haro objects will be called HH objects. The molecular cloud to the southwest of the Trapezium stars that is seen in H_2CO and H I absorption (van der Werf et al. 2013 and references therein) will be called Orion-S. The brightest part of the Orion Nebula, NGC 1976, will be designated as the Huygens Region (the region shown in the first published drawing made by Christian Huygens in 1659), while the fainter larger elliptical region to the southwest will be the Extended Orion Nebula (Güdel et al. 2008) or EON. The position angle will be PA, and the field of view will be FOV.

Where positions are given, they are in epoch 2000 and of the form 5:35:16.46, −5:23:22.85 (the coordinates of the dominant ionization source θ^1 Ori C). Radial velocities (V_r) are in the heliocentric system ($V_\odot$), and for easy comparison with the local standard of rest (LSR), one subtracts 18.1 km s^{-1} from $V_\odot$. The radial velocity of the host molecular cloud is 25.8 km s^{-1} (O'Dell et al. 2008). This velocity is used in derivation of the spatial motion (V_{OMC}) of objects with respect to the host cloud. The angle of this velocity vector with respect to the plane of the sky will be θ, and positive values indicate motion toward the observer. This notation for positive values of θ is different from that in other studies but is appropriate here because the optically thick OMC forms an opaque background.

O'Dell & Wen (1994) introduced a position-based designation system that has come into common use. It drew on the fact that most of the objects within the Huygens Region fall near θ^1 Ori C and the designations are simply the abbreviated coordinates. For example, θ^1 Ori C would be designated as 165-323, that is, the R.A. values were rounded to $0^s.1$, with 5:35 deleted, and declination values to 1″, with −5:2 deleted. In many cases we now have positions to better accuracy, and when this is the case, we introduce here a system rounding off to $0^s.01$ and 0.″1, so that θ^1 Ori C becomes 164.6-322.8 instead of 165-323. Usually an object designated as XXX-XXX is a shock or other extended feature.

We have relied on the SIMBAD database for positions of stellar sources. Publications that have been particularly important sources of positions are used with the designations HC (Hillenbrand & Carpenter 2000), MAX (Robberto et al. 2005), and COUP (Getman et al. 2005) where these are more convenient than the position-based designations. Almost always a source has been detected in multiple studies. If it has a COUP designation, we will usually use this, but when the object was already well known by a different name, we use that. Designations of the compact objects discussed in the text are summarized in Table 1. The epoch of the coordinates is 2000.0. Errors in this catalog are noted in Appendix A. The spectral types and spectral type ranges are from Hillenbrand et al. (2013).

Since the positions of large features and regions are often expressed relative to other objects, when the precision of a PA value is not necessary, we use the abbreviations of directions, for example, SSW for south–southwest. All of our images are displayed with 14° along the positive Y axis unless otherwise noted. This orientation reflects that of our new images with the WFC3 in program GO 12543. We will use CW and CCW to indicate clockwise and counterclockwise changes of PA, respectively. The abbreviation PA is usually omitted when expressing angles in degrees of arc.

1.3. A Short Primer on Photoionization Physics

The basic physics of an astronomical photoionized gas is a mature subject and well described in the popular text of Osterbrock & Ferland (2006). In a blister-type nebula one finds, when proceeding from the molecular cloud toward the ionizing star, first a mostly molecular and dust-rich PDR. This is most visible in its radio and infrared emission lines and the scattered starlight that produces a continuum that is much stronger than what is expected of an atomic gas. At the very thin H^o–H^+ MIF one begins to get photoionization of hydrogen atoms, and this continues throughout the ionized zone. [S II] emission arises from very near the MIF because sulfur rapidly becomes doubly ionized when moving away from the MIF toward the star. Immediately beyond the MIF is a low-

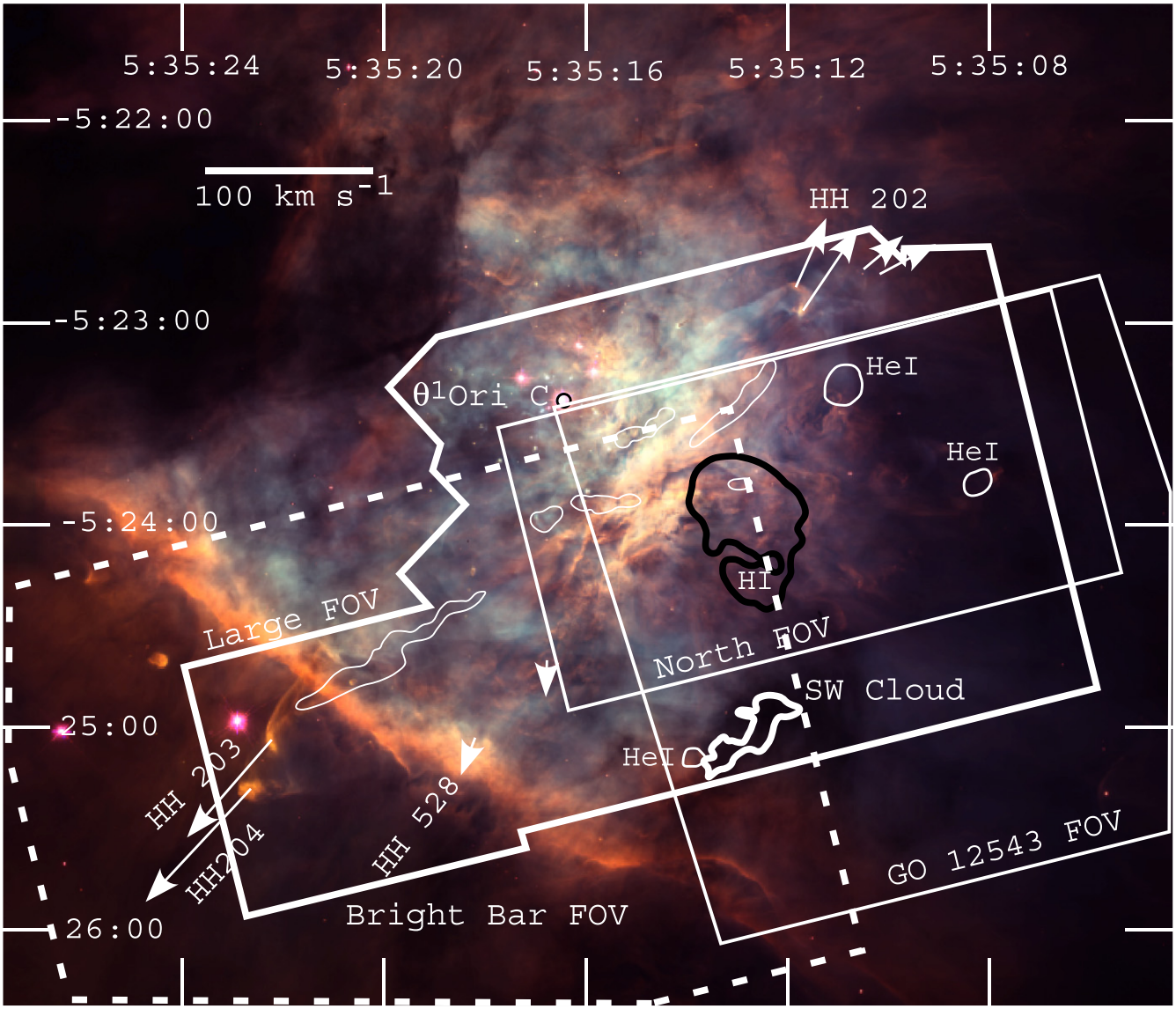

Figure 1. This 348″ × 299″ image with north up is extracted from O'Dell & Wong (1996) and shows the fields, sometimes cropped, examined in this study together with related nearby features. The 2000 coordinates are shown. The full field of the GO 12543 images is shown to the southwest from the dominant ionizing star θ^1 Ori C. The exact locations of the smaller fields overlapping with the north FOV are shown in better detail in Figure 2. The north FOV extends east of the GO 12543 and includes only WFPC2 images, as explained in Section 2.1. The Bright Bar FOV is used for Figure 24. The Large FOV is used for Figures 21–23. Motions of objects lying outside of the present tangential velocity study are shown for HH 203 and HH 204, HH 528, and HH 202 (O'Dell & Henney 2008). The thin lines denote high radial velocity features probably feeding these shocks (Doi et al. 2004) except for the three features labeled He I for reasons addressed in Section 1. The irregular structure shown with a thick black line and labeled H I is described in Section 2.2. The thick white line designated as SW Cloud indicates the region of high and isolated extinction in the study of O'Dell & Yusef-Zadeh (2000).

ionization zone where helium is neutral and nitrogen is singly ionized and easily visible in [N II]. Farther out helium becomes singly ionized, and the easiest way to trace this zone is the coexisting doubly ionized oxygen's [O III] emission. The hottest star in the Orion Nebula is unable to doubly ionize helium, and hence higher ionization states of oxygen are not found. This means that even though the observer of the Orion Nebula is looking at a column that passes through several levels of ionization, we know where the emission originates along the line of sight. When the ionization front is tilted more nearly along the line of sight, as found in the Orion Bright Bar, the ionization layers become even more obvious, with [O III] being closest to the ionizing star, followed by [N II] and finally [S II].

The Huygens Region hosts many stellar jets and outflows, and these may simply be dominated by photoionization. However, in the case of the highest-velocity features, collisional ionization can occur; a useful reference number is that the kinetic energy in eV of a hydrogen atom is $0.00518 \times V_{\rm gas}^2$, where $V_{\rm gas}$ is the gas velocity in km s^{-1}. Anticipating the results of this study, one can say that collisional ionization is important in many HH objects. H_2 emission can arise from the PDR, where it can become quite visible when a jet is passing through and the gas becomes warmer.

There is a nebular continuum that arises from atomic processes such as recombination, two-photon, and free–free emission. In the case of the Orion Nebula, the observed

Table 1
Compact Sources in the Optical Outflow Source Region Mentioned in This Study

Designation in Text	R.A. and Decl. Designation	Spectral Type	Other Designations[a]
COUP 9	[b]	K3III–IVe	JW 46, 2MASS, H 46
V2202 Ori	105.4-416.5	K8–M0	COUP 385, JW 349, MAX 9, MLLA 220, HC 146, HHH 349, LML 52
LQ Ori	107.3-344.6	K2–M1	COUP 394, DRS 21, HC 224, JW 352, MAX 12, MLLA 316, ZRK 4
d109.4-326.7	109.4-326.7	⋯	HC 286, MLLA 379
COUP 419	113.1-426.5	⋯	HC 127, LML 77, MLLA 194
COUP 423	114.9-351.9	⋯	MAX 19, MLLA 289, HC 203, LML 80
COUP 443	117.0-351.3	M0–M3	BOM d117-352, COUP 443, JW 368, MLLA 290, HC 205, HHH 368, LML 91
V1228 Ori	122.8-348.0	K1–M0	MAX 27, SB 8, HC 215, HHH378a
COUP 478	123.4-352.4	⋯	FBG 291, HC 206, LML 108, LR 3, MLLA 292
COUP 480	124.6-404.1	⋯	MLLA 245, HC 169, LML 109
⋯	129.9-401.6	⋯	2MASS
⋯	133.6-359.6	⋯	2MASS
V1398 Ori	134.4-340.2	<M0	COUP 545, JWLR. 409, MAX 41, MLLA 327, HC 240, HHH409
COUP 554	135.6-355.3	⋯	MAX 43, MLLA 276, SB 4, HC 192, LML 139
⋯	135.6-402.6	⋯	2MASS
EC 13	135.7-408.2	⋯	ZRK 137-408
COUP 555	136.0-359.0	⋯	MAX 42, MLLA 263, HC 178, LML 138, SB 5, ZRK 136-359
COUP 564	136.8-345.3	⋯	EC-MM8, HC 222, MLLA 313, LML 141, ZRK 137-347
EC 9	137.2-350.6	⋯	⋯
MAX 46	137.8-340.0	⋯	MLLA 328, SB 1, LM 78, HC 242, LML 144, LR 32, PMF 35
COUP 582	138.6-407.1	⋯	⋯
COUP 593	139.2-320.3	⋯	HC 314, LML 149, MAX 52, MLLA 413, OW 139-320
EC 14	139.3-409.4	⋯	MM14, ZRK 139-409
COUP 602	140.4-338.3	M0–M3	JW 431, MLLA 336, TCC 1, HC 247, HHH 431, LML 152
⋯	140.9-351.2	⋯	F 053246.64-052544.72
COUP 607	141.7-357.0	⋯	⋯
V1328 Ori	142.8-424.6	⋯	COUP 616, JW 437, MAX 57, MLLA 203, HC 135, LML 156
DR 1186	142.9-353.1	⋯	ZRK 15
EC 16	143.6-354.6	⋯	⋯
COUP 632	144.0-350.9	⋯	MAX 61, MLLA 293, SB 2, LM 1, LML 162
H 20051	144.6-353.8	⋯	2MASS
HC193	145.3-355.1	⋯	MLLA 273B
H 20045	145.6-349.4	⋯	⋯
HC 209	145.7-350.8	⋯	FBG 421, LML 170, MLLA 295, ZRK 141-351
H 20044	147.7-352.0	⋯	⋯
COUP 666	148.0-346.0	K6–M4	HBJ 20030, JW 453, HHH 453, MLLA 306,
⋯	⋯	⋯	TCC 14, DR 623, HC 220, LML 181, LR 72, SI 47
H 20041/2	148.3-351.3	⋯	⋯
H 20036	148.6-350.1	⋯	⋯
COUP 679	150.1-354.0	⋯	HC 195, LML 193, LR 83, MLLA 280, MC 20
H 20018	150.7-341.0	⋯	⋯
ZRK 24	150.8-353.0	⋯	⋯
H 20027	151.3-349.7	⋯	⋯
ZRK 25	151.5-353.6	⋯	⋯
EC 17	151.6-340.6	⋯	⋯
⋯	152.3-340.4	⋯	H 20014
COUP 691	152.5-349.9	⋯	MLLA 297, HC 211, LML 204, LR 92
DR 769	153.0-355.8	⋯	⋯
MAX 77	154.9-352.3	⋯	⋯
COUP 717	155.1-337.2	K	BOM d155-338, HC 251, MAX 79, LML 212, ZRK 34
COUP 725	156.8-339.0	⋯	MLLA 334, TCC 37, HC 246, LM 49, LML 221, LR 114
COUP 728	156.8-533.2	K8e	2MASS, DR 241, JW 482, MLLA 56, V2274
HC 236	157.0-341.9	⋯	LML 222, MLLA 38, LR 115
COUP 734	157.3-337.9	⋯	HC 248, LML 224, TCC 41
⋯	157.6-338.4	⋯	Discovered in this study.
θ^1 Ori E	157.7-310.0	mid-G giants	COUP 732, HC 344, MLLA 48, TCC 40
LV 6	157.9-326.7	G4–K5	HC 287, HHH 489, JW 489, MAX 86, MLLA 381, TCC 42, ZRK 40
COUP 747	158.5-325.5	⋯	MLLA 385, TCC 47, HC 291, LML 232, ZRK 43
COUP 757	158.7-337.6	⋯	DR 1007, HC 250, LML 237, LR 128, MLLA 339, TCC 50, ZRK 44
V2279 Ori[c]	159.3-349.9	G4–M2	COUP 758, HC 455, JW 499, HHH 499, MAX 92, MLLA 296
AC Ori	159.8-352.7	F2–K7	COUP 768, JW 503, HC 202, HHH 503, MAX 94, MLLA 288, ZRK 47
LV 4	160.5-324.4	⋯	HC 296, LML 245, LR 134, MAX 98, MLLA 389, TCC 54, ZRK 48
COUP 769	160.7-353.3	⋯	LML 248
LV 3	162.8-316.5	⋯	COUP 787, JW 512, MAX 105, MLLA 422, TCC 63, HC 322, OW 163-317, ZRK 52

Table 1
(Continued)

Designation in Text	R.A. and Decl. Designation	Spectral Type	Other Designations[a]
HC 292	163.2-325.3	···	LML 269, LR 154, MLL 386, TCC 66
HC 341	164.0-311.3	···	DOH 5, MLLA 445, TCC 67
COUP 820	166.1-316.1	···	MLLA 426, TCC 70, HC 325, OW 166-316, ZRK 58
LV 2	167.2-316.6	G5–K5	θ^1 Ori G, COUP 826, JW 524, MAX 116, MLLA 424, HC 323, HHH 524
COUP 827	167.6-328.0	···	MLLA 375, HC 284, OW 168-328, TCC 74, ZRK 60
COUP 900	175.7-324.7	>G6	HC 295, LML 325, LR 207, MAX 131, MLLA 387, TCC 95
HC 271	180.4-330.9	···	LML 347, LR 234, MLLA 363, TCC 106, ZRK 74
COUP 943	180.5-401.0	···	DR 458, JW 575, HC 177, LM 350, LR 235

Notes.
[a] Other Designations: 2MASS, Cutri et al. (2003); BOM, Bally et al. (2000); COUP, Getman et al. (2005); DOH, Doi et al. (2004); EC, Eisner & Carpenter (2006); DR, Da Rio et al. (2009); FBG, Feigelson et al. (2002); F, Felli et al. (1993); H, Rodríguez-Ledesma et al. (2009); HBJ, Herbst et al. (2002); HC, Hillenbrand & Carpenter (2000); HHH, Hillenbrand et al. (2013); JW, Jones & Walker (1988); LM, Lada et al. (2000); LML, Lada et al. (2004); LR, Luhman et al. (2000); LV, Laques & Vidal (1979); MAX, Robberto et al. (2005); MC, McCaughrean & Stauffer (1994); MLLA, Muench et al. (2002); NW, Nutter & Ward-Thompson (2006); OW, O'Dell & Wen (1994); SB, Smith et al. (2004); SI, Simon et al. (1999); PMF, Prisinzano et al. (2008); TCC, McCaughrean & Stauffer (1994); ZRK, Zapata et al. (2004a).
[b] Position 5:34:39.89, −5:26:42.1.
[c] Fainter companion 0.″51 at 47°.

continuum is much stronger than the expected atomic continuum because of starlight scattered by the dust within the PDR. The light in the extended area to the south of the brightest part of the nebula is primarily scattered light coming from the Huygens Region (O'Dell & Harris 2010).

The new observations in this study do not include measurements of the weak auroral transitions of [N II] or [O III], which are needed to determine the electron temperature. However, in the absence of variable extinction, the Hα/Hβ ratio would decrease with increasing electron temperature, and in the absence of strong scattered stellar continuum, one expects that the continuum would grow stronger relative to the Hβ line with increasing electron temperature (meaning that the signal ratio F547M/F487N should increase).

1.4. Outline of This Paper

The order of presentation follows. The observational material and the data processing are presented in Section 2. East–west flows are described in Section 3, large-scale features in the Huygens Region in Section 4, smaller HH systems in Section 5, and ionization shadows in Section 6.

In Section 7 the results are discussed in the following order: the nature and origin of the major flow systems (Section 7.1), a flow system coming from a star in the foreground within the cluster (Section 7.4), the relation of our results with respect to 21 cm absorption line studies (Section 7.5), the large-scale outflows (Section 7.6), outflows coming from blank areas (Section 7.7), shocks that are not the results of collimated outflows (Section 7.9), and individual sources (Section 7.10).

2. OBSERVATIONAL DATA

We are able to draw on both new and existing observational data for both imaging and spectroscopy. Since the ionization range of the Orion Nebula is quite low, we use the high signal-to-noise ratio (S/N) F658N and F502N images in our analysis (although occasionally good-quality F673N images are available and are used). There was already an excellent set of high-resolution (10 km s^{-1}) spectroscopy mapping the Huygens Region (García-Díaz et al. 2008 and references therein). We have been able to supplement these spectra with superior data for the [O III] 500.7 nm line in the highest-ionization part of the nebula.

2.1. New Imaging Observations

Our new imaging observations were made with *HST*'s WFC3 as part of program GO 12543. The FOV covered is shown in Figure 1. Observations were made (2012 January 7) with the narrowband emission line filters F487N (Hβ 409 s), F502N ([O III] 348 s), F656N (Hα 349 s), F658N ([N II]602 s), and F673N ([S II] 700 s), in addition to observations with the continuum sampling intermediate-width filter F547M (348 s). The characteristics of these filters and their calibration have been described by O'Dell et al. (2013a). Although the images are of high quality, the gap between the two detectors in the WFC3 has poorer cosmic-ray event canceling, and these have generally been left in the images, except where hand-editing was necessary. Since the present study does not try to do spectrophotometry, we usually normalized the images to the same signal level.

These are the highest angular resolution (0.″04 pixel^{-1} sampling) optical images of a portion of the Huygens Region. When used alone, we employed the original images in combination with one another. When used for comparison with earlier (undersampled) WFPC2 images (0.″0996 pixel^{-1}), we processed them with IRAF[8] task "Gauss" to match their broader image cores.

2.2. Earlier Imaging Observations

We have been able to use earlier *HST* observations made with the WFPC2. In order to compare these images with the new WFC3 images, we aligned AstroDrizzle processed versions of them with the GO 12543 AstroDrizzle processed images using stars common to both. Table 2 summarizes the data sets we used. For the FOV of the WFC3 we matched the WFPC2 images by magnifying them by 2.5247 as determined from measuring a large set of common stars to an error of

[8] IRAF is distributed by the National Optical Astronomy Observatories, which is operated by the Association of Universities for Research in Astronomy, Inc., under cooperative agreement with the National Science foundation.

Table 2
Data Sets Used in Determination of Tangential Velocities

Program	Camera	Modified Julian Date	Program Pair	Velocity Scale (km s^{-1} pixel^{-1})[a]
GO 5085 (FOV5)	WFPC2	49737	…	…
GO 5469	WFPC2	49797	…	…
GO 11038 (FOV1)	WFPC2	54406	…	…
GO 12543	WFC3	55935	…	…
…	…	…	5085+12543	4.92
…	…	…	5469+12543	4.96
…	…	…	5469+11038	16.46

Note.
[a] Velocity scale was determined using a distance of 440 pc (O'Dell & Henney 2008) and pixel scales of 0.″04 pixel^{-1} (WFC3) and 0.″0996 pixel^{-1} (WFPC2).

±0.0003, to the same pixel scale as the WFC3. In a small region to the east of the GO 12543 FOV we could only use WFPC2 images. The east extension of our primary area of study is shown in Figure 1. Data from the GO 12543 FOV were used whenever possible, with the lower-resolution data from the WFPC2 being used only in the small east extension. The Guest Observer program numbers of the data used are given in Table 2.

2.3. Spectroscopic Observations

The most useful data set of spectra is the compilation of north–south orientation long-slit spectra by García-Díaz et al. (2008). In addition to their original observations (García-Díaz & Henney 2007) in low-ionization lines, they recalibrate the high-ionization spectra of Doi et al. (2004) and present combined results for emission lines from a wide variety of ionization states ([O I] 630.0 nm, [S II] 671.6 nm + 673.1 nm, [N II] 658.4 nm, [S III] 631.2 nm, Hα 656.3 nm, [O III] 500.7 nm) calibrated to 2 km s^{-1} accuracy and a resolution of about 10 km s^{-1}. We will refer to this as the Spectroscopic Atlas, or simply the Atlas.

New observations were made at the San Pedro Martir Observatory in 2013 February in the [O III] 500.7 nm line in essentially the same manner as the earlier low-ionization line observations, except that the slit was oriented east–west. The slit center was at 5:35:15.9. Fifteen spectra were obtained in steps of 1.″4 starting at 23″ south of θ^1 Ori C and proceeding south. Their total exposure time in each slit of 300 or 600 s, depending on the source brightness, with the 2.1 m telescope's MEZCAL spectrograph gave higher-S/N images than the earlier observations made at the Kitt Peak National Observatory with the 4 m telescope's echelle spectrograph by Doi et al. (2004).

2.4. Determination of Changes of Position and Structure

In order to detect changes of position (the tangential motion, which we designate by the tangential velocity calculated with the assumption of a distance to the Orion Nebula of 440 pc; O'Dell & Henney 2008) and changes of the structure, the first and second images had to be aligned. This was done using stars common to both FOVs and the IRAF tasks "geomap" and "geotran," using the GO 102543 images as the reference system. The scatter of the matched images was ±0.5 pixels (2.5 km s^{-1}) for the WFC3-WFPC2 combinations and ±0.2 pixels (3 km s^{-1}) for the WFPC2-WFPC2 combinations used in the east extension of the GO 12543 FOV.

We have chosen to use the ratio of the first-epoch image divided by the second-epoch image to identify the moving and changing features. Figure 2 shows the power of this approach. This figure shows the very different changes in the images of high- and low-ionization gas, and the eye is able to identify large-scale patterns quite well. A bright linear feature moving orthogonally will appear as a dark/light combination of lines, with the dark line being in the direction of motion. The pattern would be the reverse for a linear dark feature. In the event of a mix of bright and dark features, the pattern of light-dark fails to be a guide to changes, and only the measurement of specific features is useful.

The WFPC2 images often have "scars" where CCD boundaries occur. These propagate through to the motion images as straight lines of various forms. Likewise, the motions and ratio images formed from a combination of exposures often show changes of the nebula's "background" signal because of imperfect flat-field corrections. These too propagate through into the motions and ratio images. Rather than make cosmetic adjustments for either the boundaries or the flat-field correction step (because this involves modifying the scientific information), we have left the images in this scarred but rigorous form.

We measured individual features by two methods. The first method was a least-squares image-shifting procedure developed by Hartigan et al. (2001) from an approach originated by Currie et al. (1996). In many cases where the features being measured were very complex, we identified individual small structures and determined their motions by direct comparison of the images. This is the same methodology employed in our earlier studies of the Huygens Region (O'Dell & Henney 2008 and references therein), the brightest LL Ori objects in the Orion Nebula (Henney et al. 2013), and the Ring Nebula (O'Dell et al. 2013b). The results for individual features are given in Appendix B.

2.5. Determination of Radial Velocities

The [N II] 658.3 nm and [O III] 500.7 nm archived spectra had an instrumental FWHM intensity of about 10 km s^{-1}, and the new [O III] spectra's FWHM are slightly smaller. The observed FWHM is the quadratic addition of the instrumental FWHM and the thermal broadening FWHM. The thermal broadening is about 5.7 km s^{-1} for [N II] and 5.4 km s^{-1} for [O III] if the electron temperature is 10,000 K. The quadratic addition of the instrumental and thermal FWHM values gives an expected observed FWHM of 11.5 km s^{-1} for [N II] and 11.4 km s^{-1} for [O III]. In the case of the nebula's background emission, there may also be an additional small broadening due to acceleration of gas away from the nebula's MIF.

Since the radial velocity features corresponding to the high tangential velocity features are usually faint as compared with

Figure 2. This pair of 196.″4 × 91.″8 images isolates the northern region of the images examined in detail. It has PA = 14° up, which is the case for all other images in this paper unless otherwise noted. The region is designated as "north FOV" in Figure 1. Each image is centered at 5:35:11.0, −5:23:53. It shows motion images, with F502N used for the upper panel and F658N for the lower. This will be the pattern in the remaining images in this study. The black and white outlines show the FOVs used for individual flows: HH 269 (Section 3.1), HH 269-west (Section 3.1.2), HH 510 (Section 5.1), HH 625 (Section 4.6), east–west (Section 3), west (Section 3.2.1), east (Section 3.2.2), sources (7.10), HH 529 (Section 3.3.1), HH 530 (Section 5.3), HH 626 (Section 5.4), large-west (Section 5.12), southwest (5.10), and HH 1148 (Section 5.13). In the lower panel the circles designate the shocks argued in Section 5.13 to compose the large-scale flow HH 1148.

the background, how well a radial velocity component can be measured will be determined by its contrast. Those lines of high Doppler shift from the nebula's systemic velocity (18 km s^{-1} for [N II] and 15 km s^{-1} for [O III]) are the most easily detected, with accuracy of measurement of about 2 km s^{-1}. Things get worse as the Doppler shift decreases, with a line of about equal intensity to the nebula's emission resolvable down to about a velocity difference of 3 km s^{-1} and with a comparable uncertainty. These observational biases constrain the results of our radial velocity database analogous to the way that form and change of structure constrain the tangential velocity database.

Our slit spectra were examined visually, and those indicating the presence of a high-velocity feature were analyzed using IRAF task "splot." This task can deconvolve the observed spectra into multiple components. Although the spectral data archive also includes spectra for [O I], [S II], [S III], and Hα, we did not measure those spectra because we have high-quality tangential motion measures for only [N II] and [O III]. Those spectra should be valuable for

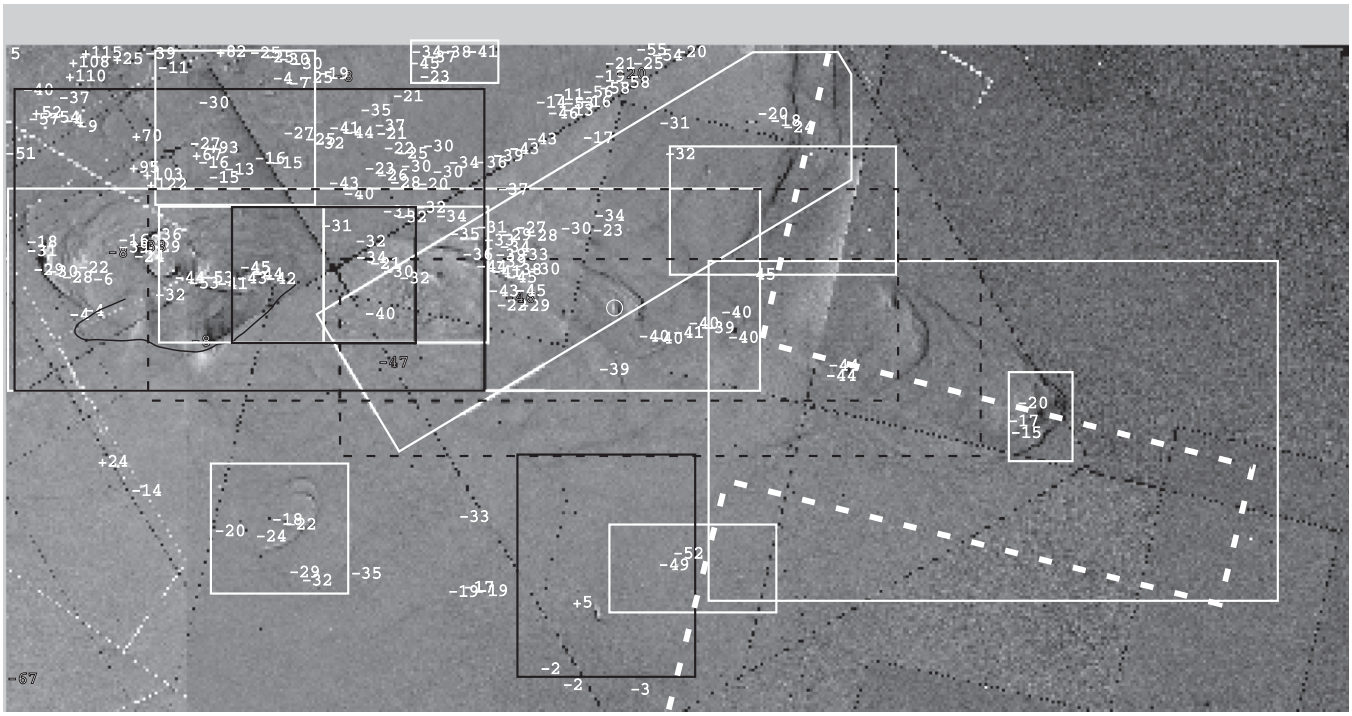

Figure 3. Like Figure 2, except showing only the upper (F502N) panel. Radial velocities in [O III] are shown. The labels of the samples have been removed for clarity. The irregular thick dashed line shows the western boundary of the area covered by the combined archived and new slit spectra.

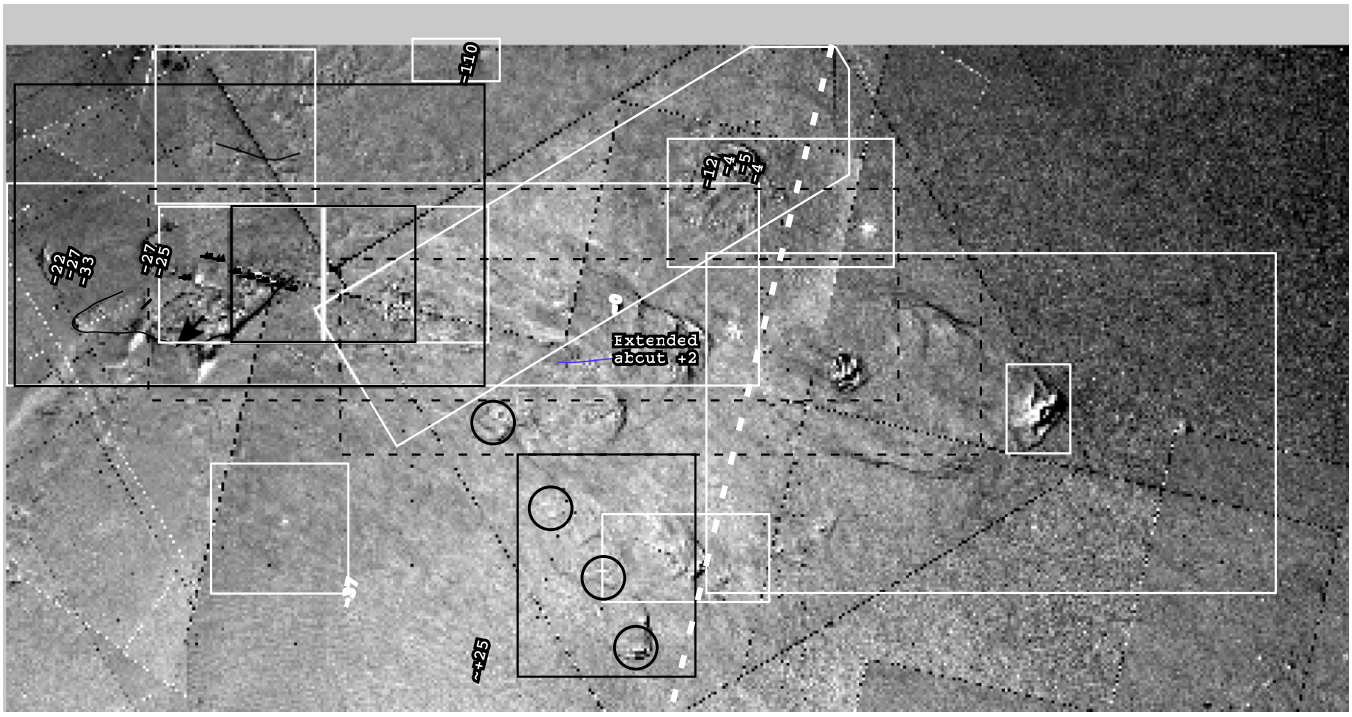

Figure 4. Like Figures 2 and 3, except showing only F658N results. Radial velocities in [N II] are shown. The thick dashed line shows the western boundary of the area covered by the archived slit spectra. The open black circles indicate the position of features associated with HH 1148 that are discussed in Section 5.13. The region identified as "Extended about +2" is a feature seen throughout much of the Huygens Region starting with the study of HH 269 by Walter et al. (1995).

understanding individual objects. The derived radial velocities are presented in Figures 3 and 4. There, as in all places in this article, radial velocities (V_r) are in the heliocentric rest frame. Correction to the LSR rest frame can be obtained by subtracting 18.1 km s^{-1}. The radial velocity of the host molecular cloud is 25.8 km s^{-1} (O'Dell et al. 2008). The velocity of the background molecular cloud can vary in different regions up to a few kilometers per second, which does not have an important impact on this study. The astronomical seeing during the spectroscopic observations and the adjustments made in alignment mean that each velocity sample represents a diameter of about 2″ and a positional

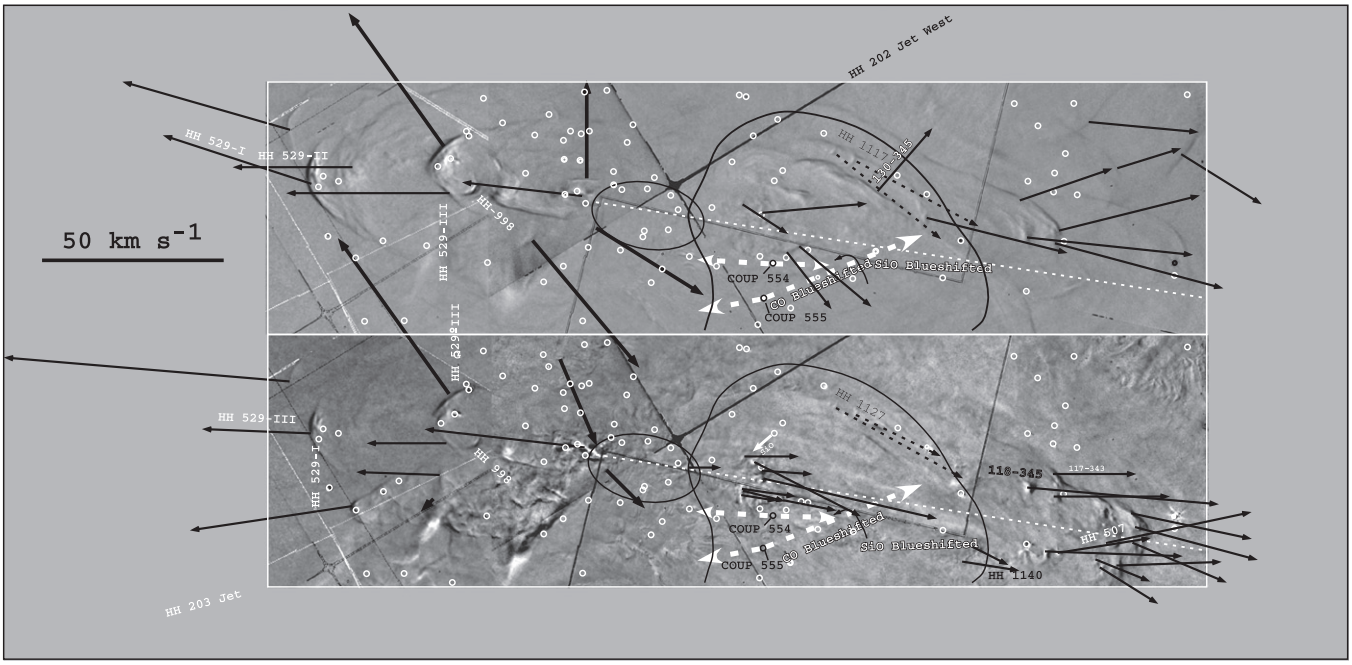

Figure 5. These $103\farcs4 \times 27\farcs8$ panels depict the motion images for the east–west sample in Figure 2. They show the east and west motions as one crosses Orion-S. The ellipse indicates the OOS region (O'Dell & Doi 2003a, 2003b) and the irregular line the outer 21 cm line absorption boundary of the Orion-S cloud (van der Werf et al. 2013). Arrows indicate the tangential velocity vectors of some of the optical features. Circles indicate the position of known point sources taken from the SIMBAD database. The thick white dashed arrows indicate molecular outflows, with their length indicating the distance over which they have been measured (Zapata et al. 2006). The thin white dashed line indicates the direction of the HH 269 features.

uncertainty of slightly less than $2''$. These are given in Appendix C.

3. EAST–WEST FLOWS

Many of the most striking flows in the Huygens Region are oriented east–west, with west-moving objects in the west and east-moving objects in the east. We first define a sample that covers the middle of the Huygens Region, explain the orientation of previously known HH objects with respect to this FOV, and then examine the HH objects within and adjacent to this FOV.

The east–west sample is shown in Figure 2, and comparison with Figure 1 shows that the 21 cm absorption line tracer (van der Werf et al. 2013) of the Orion-S cloud lies in the middle of the sample. This sample was chosen to illustrate the east–west flow from the region, with the west-moving HH 269 being an apparent extension to the west and the east-moving HH 529 to the east. The HH 269 FOV lies to the immediate west, and the HH 625 FOV overlaps the east–west sample and extends to the NW.

The intersection of the line connecting west-moving HH 269 and east-moving HH 529 and the well-defined jets feeding HH 202 to the NW and HH 203 to the SE was pointed out by O'Dell et al. (1997a) and Rosado et al. (2002) from radial velocity mapping. O'Dell & Doi (2003a) used information from all these flows, based on astrometric data, to argue for a common region of origin within an ellipse of $7'' \times 12''$ centered at 5:35:14.56, −5:23:54 and designating it as the optical outflow source (OOS; Figure 5). The OOS was defined in the north–south direction by the approximate axes of the HH 269 and HH 529 flows and in the east–west direction by the region where there is a reversal of tangential motions, which agrees with the intersection of flows leading to HH 202 to the NW and HH 203+HH 204 to the SE. It lies on the east boundary of the core of Orion-S, and Figure 5 shows that it is near the peak surface density of known stars. In the current article we examine the question of the origins of these HH flows. As we will see, it is likely that there are multiple sources of the outflow, all lying nearby but not within the OOS.

3.1. HH 269

The first of the objects now included in the designation HH 269 was noted by Feibelman (1976), and this region was noted to have concentrations of density higher than the local nebula by Walter (1994). A big step in characterizing its components was the study of Walter et al. (1995), which included imaging with the *HST*'s WF/PC and high- and low-resolution spectroscopy. At that point it was considered a single elliptical structure with two enclosed bright knots. These knots were first designated as HH 269-east (hereafter in this section east) and HH 269-west (hereafter in this section west) by Bally et al. (2000), who also derived tangential velocities from images over a short time base.

Stanke et al. (2002) mapped the entire Orion Nebula region in H_2. They found several small aligned features. By comparison with our new *HST* images we find that the H_2 feature in their sample 2–6 corresponds to HH 269-east. In their images we see that there are fainter H_2 features, one associated with HH 269-west, and a hint of others to the west. The study of He I (Takami et al. 2002) shows a high-velocity component at HH 269-west. There is an isolated H_2 knot farther west with $153''$ at 275° (this direction falling along a line from HH 269-east to HH 269-west).

O'Dell & Doi (2003a) and O'Dell & Henney (2008) have derived improved tangential velocities from *HST* images of higher resolution and longer time base, establishing that the

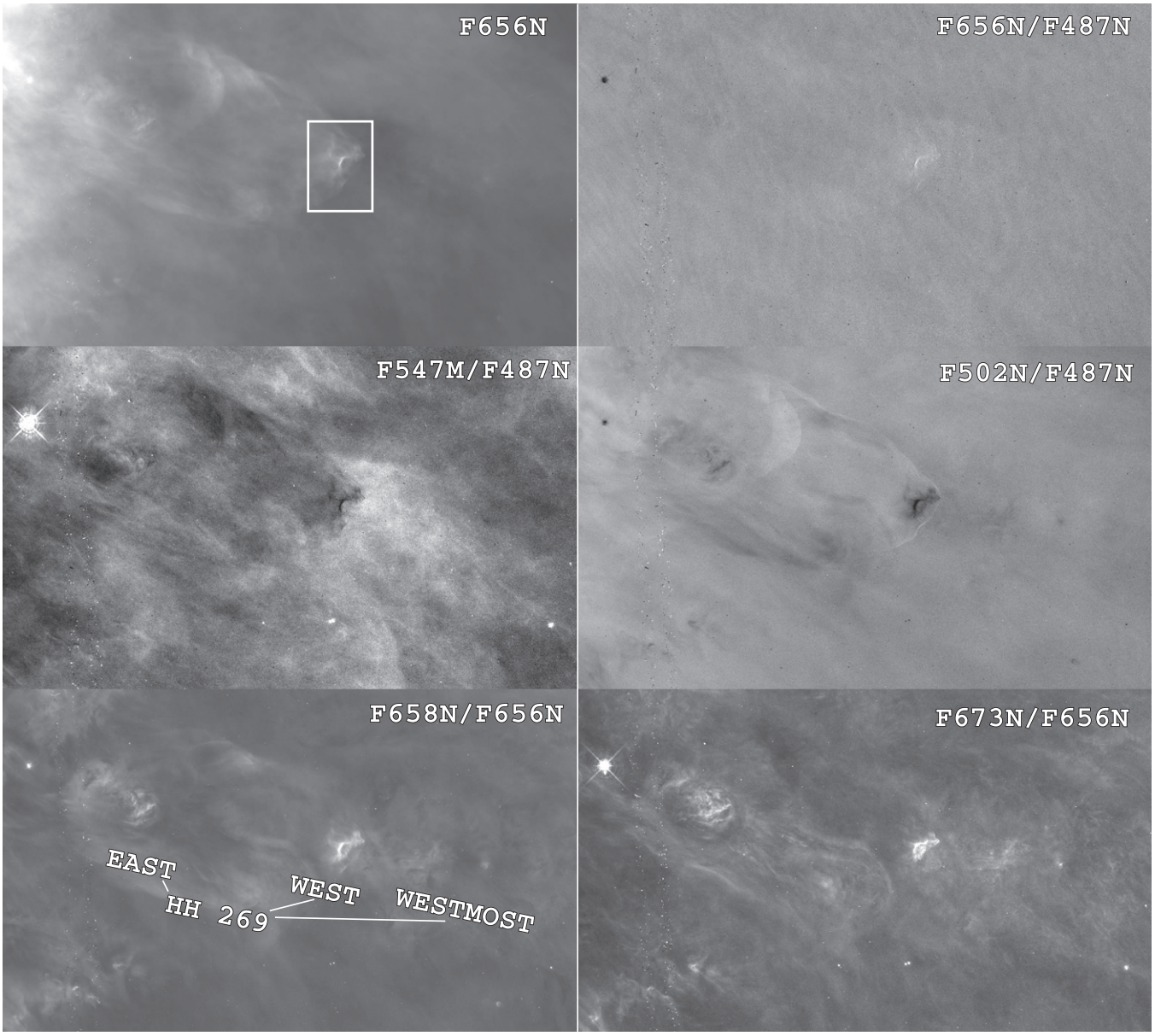

Figure 6. This mosaic of 78.″3 × 46.″7 FOV images is centered on HH 269. The upper left panel is an F656N image, and the upper right panel shows the extinction-sensitive F656N/F487N image. The others are selected to show extinction-insensitive but ionization-structure-sensitive image ratios. The smaller field isolating HH 269-west in Figure 8 is shown in the F656N image.

two bright features were part of a series of low-ionization shocks sharing the same direction and probably also having the same source. The best V_T values using the material in the present study are presented in the next section, as are new determinations of V_r.

We have assembled our images of HH 269 in Figure 6. The F656N panel shows that the object is not conspicuous. However, the structure becomes more obvious in the line ratio images. The F658N/F656N image shows well that the bright east and west components are of low ionization (as shown in the low-resolution spectroscopy of Walter et al. 1995) and that there is an open parabolic shock oriented to the west and with HH 269-west at its tip. This shock contains both high (F502N) and low (F658N) emission. There also appears to be an unrelated high-ionization shock with a larger PA and a tip 12.″4 at 310° from HH 269-east (Figure 7).

The F656N/F487N image shows that interstellar reddening does not vary across HH 269, since the F656N/F487N ratio is nearly constant except at the linear feature in middle of HH 269-west (Section 3.1.2).

3.1.1. HH 269 Motions

We now have up-to-date V_r and V_T values for the HH 269 system. We first summarize here the V_r and then the V_T results.

The radial velocities obtained by Walter et al. (1995) are $V_r = -13$ and $-22.5\,\mathrm{km\,s^{-1}}$ in [N II] for the east and west components, respectively. They did not isolate a component in [O III]. Our new spectra cover portions of both the east and west features as shown in Figure 3. In the west feature our [O III] velocity (average $V_r = -18\,\mathrm{km\,s^{-1}}$) agrees well with the Walter et al. (1995) V_r value for [N II] of $-22.5 \pm 2.4\,\mathrm{km\,s^{-1}}$.

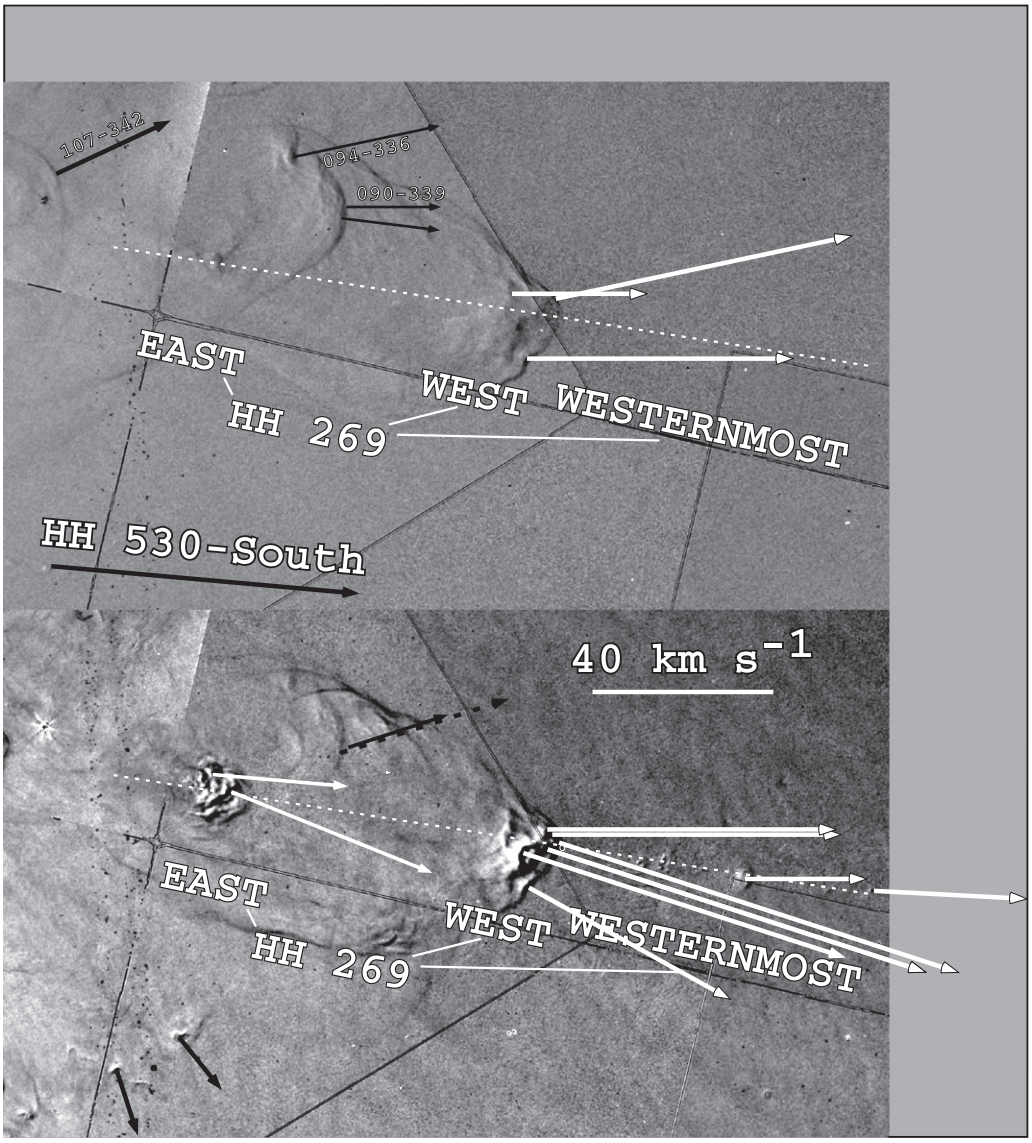

Figure 7. The same FOV as Figure 6 is shown, but now depicting motion images (F502N in the upper panel, F658N in the lower panel). In this image the white arrows depict the motions associated with the primary flow and the dark arrows are motions not associated with it. The dashed white line indicates the line common to the HH 269 east, west, and westernmost [N II] features, pointing toward 275°.

However, the Walter et al. (1995) value of $V_r = -13 \pm 1.4\,\mathrm{km\,s^{-1}}$ derived from [N II] in east is quite different from our value for a very weak component in [O III] of $V_r = -44$ at two points. In [O III] this feature looks quite different than in [N II], and it is likely that we are seeing two different and superimposed objects. Figure 3 shows that the moving objects to its east all have V_r of about $-40\,\mathrm{km\,s^{-1}}$, strengthening the argument that the east [O III] V_r measurements are of a different feature than the [N II] feature.

O'Dell & Doi (2003a) and O'Dell & Henney (2008) have derived improved tangential velocities from *HST* images of higher resolution and longer time base, establishing that the two bright features were part of a series of low-ionization shocks sharing the same direction and probably also having the same source.

In the pair of motion images shown in Figure 7 we see that tangential velocities are well defined in F658N for both the east and west components. We also see in F658N that there are a series of slower-moving small knots to the west. These lie exactly along the line projecting through east, west, and the H_2 observed by Stanke et al. (2002). We call these collectively the HH 269-westernmost features. In F502N there are no features that may be associated with HH 269-east, while the features observed nearby share orientation and placement that identify them with the high-ionization shock NNW of east. In the lower left part of the F502N panel we note the western portion of the HH 1157 bipolar flow discussed in Section 5.3.1. The dark vectors in the F502N panel are discussed in Section 5.12, where they are assigned to a different flow and not from HH 269. Feature HH 269-east is highly structured and resembles the well-studied HH 204 shocks (O'Dell et al. 1997b).

Both the east and west components are moving toward the observer with respect to the plane of the sky. Adopting the Walter et al. (1995) [N II] radial velocity and our average [N II] $V_T = 13\,\mathrm{km\,s^{-1}}$ for the east shocks gives $V_{OMC} = 57\,\mathrm{km\,s^{-1}}$ at 43°. Adopting the Walter et al. (1995) [N II] radial

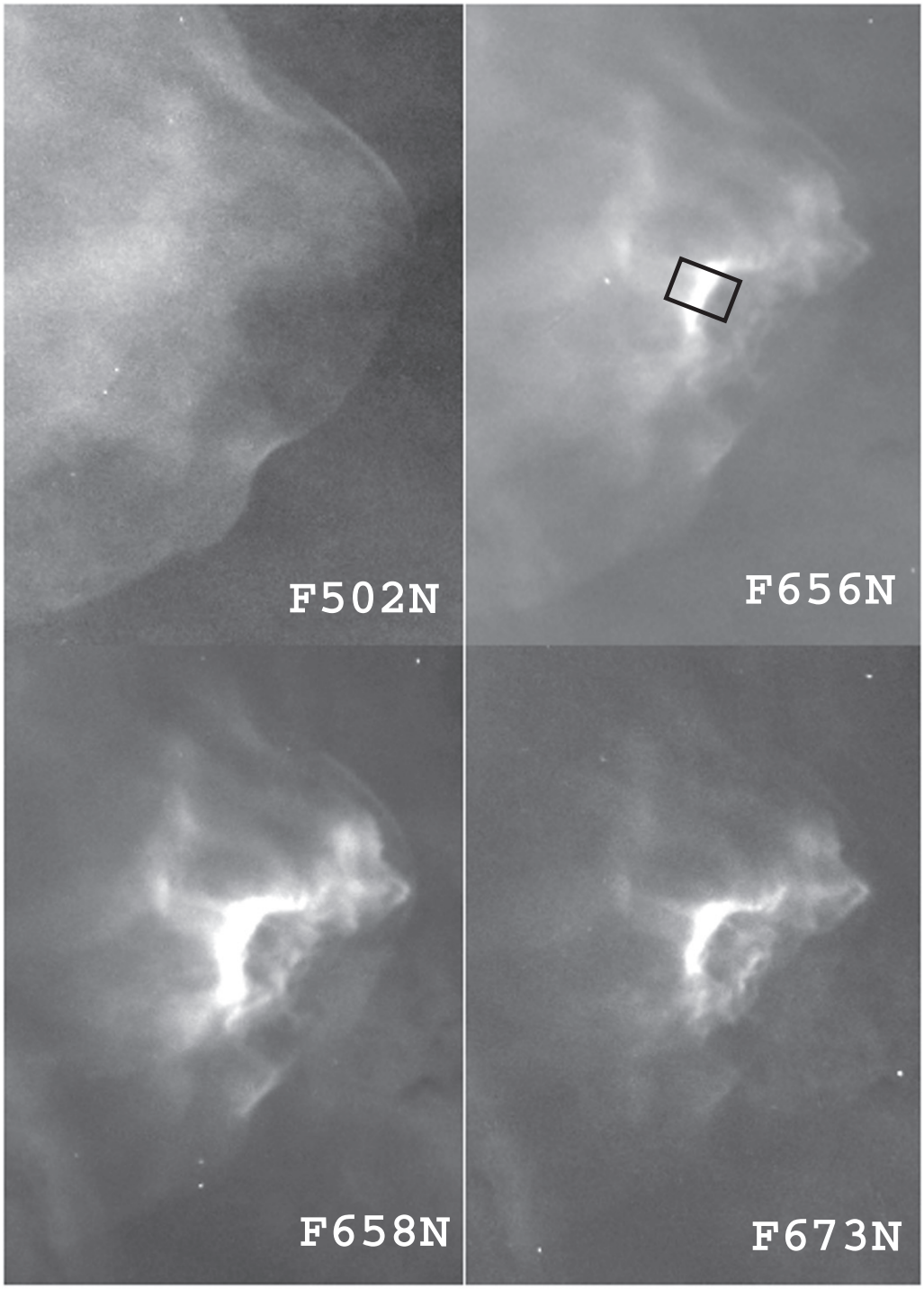

Figure 8. This mosaic of 8.76 × 12.″24 single-filter images isolating the HH 269-west feature again has 14° up. The small box within the F656N image shows the area sampled in the profiles shown in Figure 9.

velocity and our average of both the [N II] and [O III] components of $V_T = 66\,km\,s^{-1}$ yields $V_{OMC} = 82\,km\,s^{-1}$ at 36° for the west shocks. If the difference of the angle of approach of these two figures is accurate, then their origin is probably not as far east as is argued in Section 3.2.1; however, the derived angles are quite sensitive to the observational data, and the 7° difference is probably within the error of determination. The difference in velocity is more likely to be real.

3.1.2. HH 269-west

We show a fine-scale image of HH 269-west in the mosaic of images in Figure 8. The F502N image shows that west contains a bow shock feature oriented to the west. Within the boundaries of the bow shock the lower ionization emission is highly structured, with the dominant feature being the bright north–south oriented nearly linear feature that appears to be quite different from the nearby gas. This feature must be related to the shock caused by a collimated jet, but we have not addressed

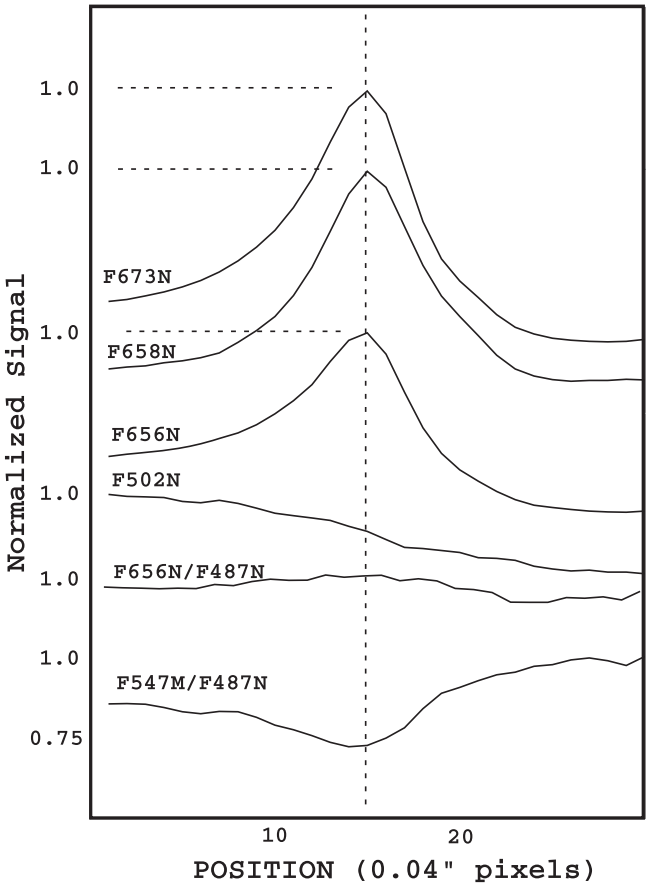

Figure 9. This series of profiles is from left to right in the small box within Figure 8 and is an average along the short dimension of the box. In each case the maximum value has been normalized to 1.0. The scale is the same for each, but they have been shifted for clarity. The vertical dashed line is drawn at a fixed pixel in the sample.

particularities of this complex structure. Previous studies of HH objects have argued that similar structures are Mach disks (Morse et al. 1992, 1993).

As part of an effort to understand the bright nearly linear feature, we show in Figure 9 the results of averaging the signal in the 1.″1 wide box shown in Figure 8. It is remarkable that the signals from F656N, F658N, and F673N all peak at exactly the same time (within a fraction of an 0.″04 pixel), although the widths are different. F502N does not seem to be produced in the feature. The F656N/F487N ratio increases at the peak of emission, and the F547M/F487N ratio decreases there. The ground-based spectra of Walter et al. (1995) indicate that the HH 269-west feature has about twice the local density. Since those spectra had low spatial resolution, the density enhancement in the locally bright linear feature is probably even greater. This is almost certainly true because the peak surface brightness in F656N is much higher than the local region, even though its width is very small. The feature is certainly a thin density feature. The drop in the F547M/F487N ratio indicates that either the scattering of stellar continuum is less important (in contrast with the expectation that the dust would have higher density where the gas density is higher) or the electron temperature is lower. A lower electron temperature is also consistent with the F656N/F487N ratio being higher.

3.2. Motions near the OOS Region

In this section we discuss outflows in the vicinity of the OOS, beginning with a region west (Section 3.2.1) and then a region east (Section 3.2.2).

3.2.1. Motions in the Region West of the OOS Region

The region we designate here as west (Figure 2) is a complex region already known to be of considerable interest. The northern portion contains a predominant feature designated in Figure 10 and in previous studies as the Dark Arc. The 3D structure of this feature remains undetermined in spite of attempts to explain it (O'Dell & Yusef-Zadeh 2000). It is almost certainly part of the Orion-S cloud and must lie on the observer's side of Orion-S (otherwise, it would be invisible owing to the high extinction in Orion-S).

The conundrum is that the sharp north edge of the Dark Arc has a narrow rim of bright F658N and F673N emission, indicating that we are seeing an ionization boundary. However, as we see in Figure 10, the high-ionization (south) side of this front is in the opposite direction of θ^1 Ori C, which lies to the NE. A clue to the structure may lie in the fact that the series of shocks forming HH 1127 (see Section 5.6) become visible starting at the rim after passing from the obscured source (either MAX 46 or COUP 602) across the north rim of the Dark Arc. This indicates that the south side of the Dark Arc's sharp northern boundary is an open space.

The thin and irregular low-ionization feature designated as the west-jet has been the subject of multiple studies and has been argued (O'Dell et al. 2008 and references therein) to be the easternmost component of the collimated material driving HH 269. It has an orientation of 276°. It lies almost on the symmetry axis of the HH 269 features, and there are 10 low-ionization features nearly along the symmetry axis. The axis of the west-jet is essentially parallel to the symmetry axis of the HH 269 features. If the HH 269 axis was adjusted to 276°, rather than the best value from the HH 269 components of 275°, then the east end of the HH 269 axis would be raised north and be in exact alignment with the west-jet, sharing both the alignment angle and position. Such a small change to the value of the HH 269 axis is allowable because determination of the HH 269 axis is imperfect and we know that jet flows can curve. Figures 10 and 11 show the adjusted HH 269 axis.

However, this putative jet lacks a continuous structure and shows large tangential motions only along its west end. The middle panel of Figure 10 shows that the putative jet is low ionization. There are no identified [N II] V_r sources associated with this feature. The only two nearby tangential [O III] motions are displaced from this feature, although they do move approximately along the HH 269 axis. In [N II] there are a host of motion features whose northern boundary is along the west end of the west-jet, but they many lie 4″ south, and only two lie exactly on the west-jet. An additional isolated moving [N II] feature lies to the east right on the west-jet. The three [N II] V_T features lying on and moving along the axis of HH 269 argue that the west-jet is an actual collimated outflow. The presence of similar features above and below the axis indicates that either not all of the features are related to the west-jet or we are seeing the superposition of two flows of different origin by similar location and movement on the plane of the sky. In any event, the easternmost moving feature must belong to a flow that originates to the east of star 140.9-351.2.

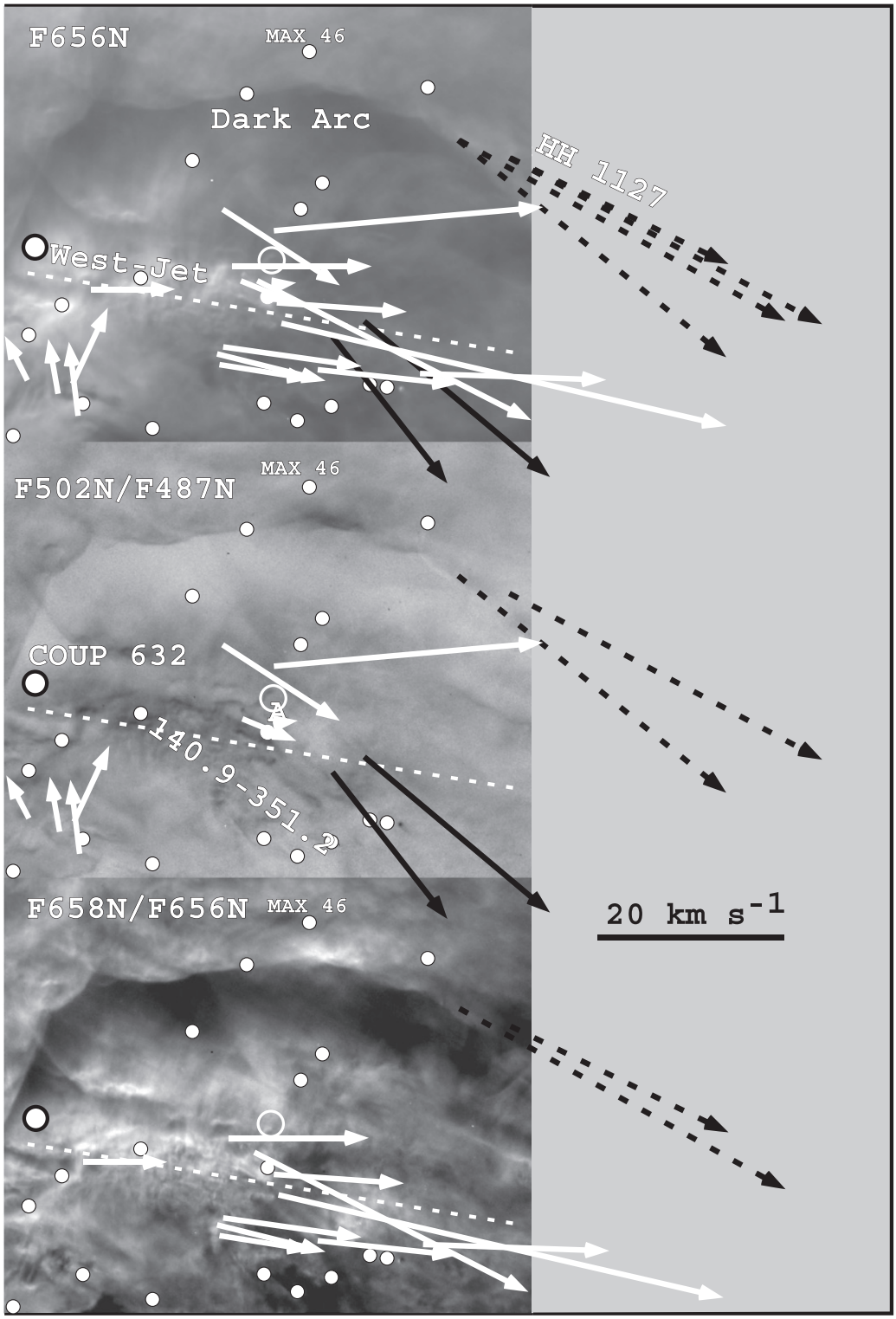

Figure 10. These three line and ratio images show the 22.″6 × 18.″7 FOV designated as west in Figure 2. The F656N image has had the velocity vectors for both F502N and F658N added from Figure 11. The F656N image also shows the location of the possible west-jet. The other panels show extinction-insensitive ratio images that highlight ionization differences, and the appropriate motion vectors have been added. SIMBAD stars are shown with filled circles in this and following figures. Flows from near MAX 46 have been labeled as HH 1127. This object is discussed in Section 5.6. The dashed white line indicates the adjusted projection of the axis of HH 269.

The shocks and [O III] radial velocity features in the upper right of Figure 11 are discussed in Section 5.6.

The concentric rings shown in the F502N motion image (the upper panel of Figure 11) and their central point are discussed in Section 7.7.1. The [O III] radial velocity features toward PA = 67° start at this spot, after consideration of the size of the spectroscopic samples, and it is possible that they represent an otherwise undetected collimated flow from the invisible source.

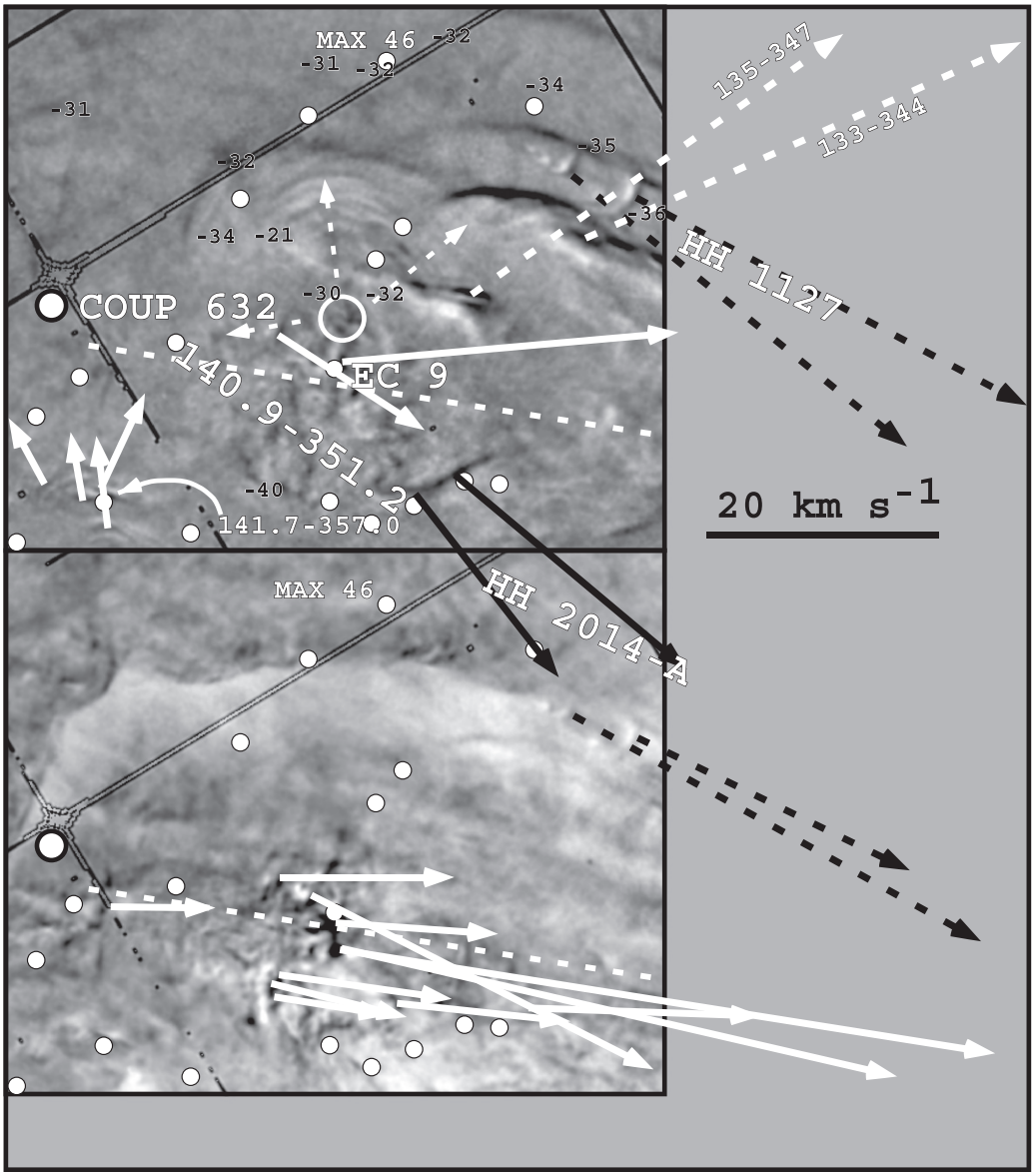

Figure 11. The same FOV as Figure 10 is shown, except now the motion images are shown. The dark dashed arrows indicate motions in two portions of HH 1127, while the thick white arrows indicate motions that are likely to be part of the system driving HH 269. The thin white arrows indicate the symmetry axis of faint concentric expanding features seen in F502N. The thin dashed white lines with arrows show the direction of motion of concentric rings of motion visible in F502N. The dashed white line without arrows indicates the adjusted projection of the axis of HH 269. The open white circle indicates the point of convergence of them as discussed in Section 7.7.1. [O III] radial velocities are shown as small negative numbers with black centers and white borders. The four [O III] vectors in the lower left of the lower panel are not shown for clarity in Figure 10 and are discussed in Section 5.8.

3.2.2. Motions in the Region East of the OOS Region

Many earlier studies have established that the east–west flow centered on Orion-S reverses in or near the OOS. Figure 12 demonstrates that there is a well-defined, irregular, mixed ionization jet there.

The changes of position and of structure of the features constituting the east-jet are illustrated in the F658N images in Figure 13. The complexity of the region works to make determination of changes of position more difficult; but, fortunately and for the most part, the large size of the motions balances this limitation.

Figure 14 demonstrates the velocity vectors in this region. The center of the east-jet is at 5:35:15.04, −5:23:53.1. The orientation of the east-jet is toward 108°, while a similar appearance feature to its north is oriented at 101°. The fact that most of the north feature is not moving rapidly makes it likely that is an ionization front viewed edge-on and is labeled "Edge-on Ionization Front" in Figure 12.

The F658N motion image in Figure 14 shows that the motion of the east-jet is along its axis of symmetry and that an east–west feature about 1.″2 south has a similar motion in F658N. In the F502N panel we see that there is motion or change on this south-lying feature, but on the north side of the east-jet there is clear northerly motion of F502N-emitting material. One moving F502N feature near the center of the ellipse has been measured and has a similar velocity but different direction of the F658N features. There are multiple

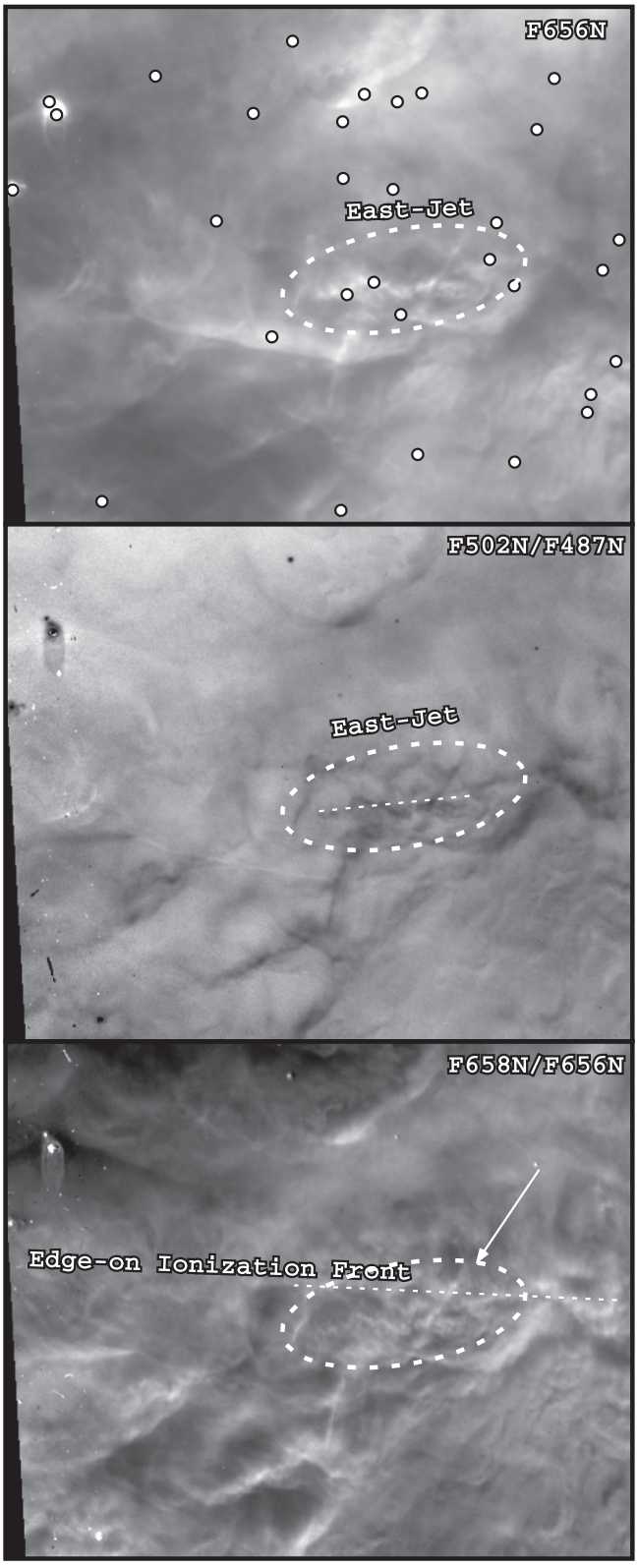

Figure 12. This figure shows the line and line ratio images for a 22.″6 × 18.″7 FOV immediately east of the west FOV and designated as east. A well-defined low-ionization filamentary structure is easily seen and is designated as the east-jet. The axis of the jet is shown with a thin dashed white line in the F502N/F656N ratio image, while the axis of a nearby edge-on ionization front is shown in the F658N/F656N ratio image. The region including the east-jet is shown by the white dashed ellipse. The thin vector points to the linear feature arising from COUP 666.

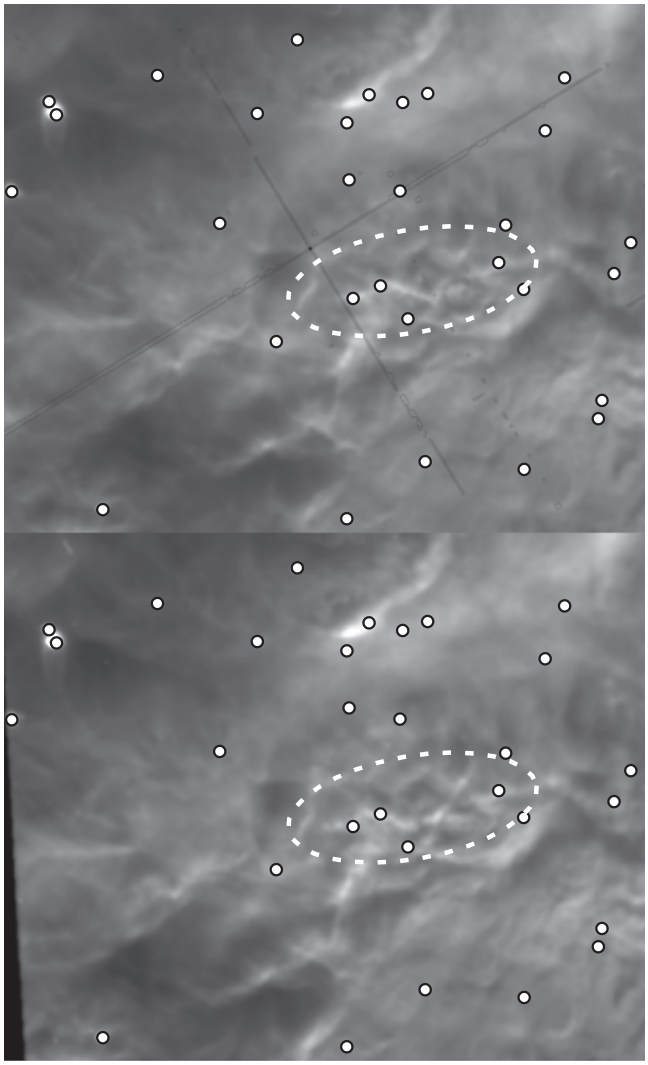

Figure 13. First (upper, GO 5469) and second (lower, GO 12543) F658N images of the east FOV are shown. The region including the east-jet is again shown by the white dashed ellipse. Examination of the jet feature demonstrates both its rapid motion to the east and also changes in its structure.

other moving F502N features, but they have not been measured because there have been significant changes in their structure. Examination of the moving features indicates that the bulk motion of the east-jet may be a few degrees smaller in PA than that suggested by the symmetry of the irregular filament. Like the west-jet, there are both F502N and F658N features, although the F502N features are relatively stronger in the east-jet.

The radial velocity results shown in Figure 14 define two patterns of high radial velocity features. The [O III] features align toward PA = 107°, which agrees with the symmetry axis of the east-jet (PA = 108°). These high radial velocity [O III] features extend well beyond the ellipse containing the west-jet. The seven [N II] high tangential velocity features have PAs of 83° on the east end and 87° on the better-defined west end. The pattern of positions of the [N II] high radial velocity features has PA = 94° and intersects the [O III] pattern on the east end of the outline of the east-jet features.

Although the velocities are similar in the two ions, it appears that we are observing two different series, the east-jet

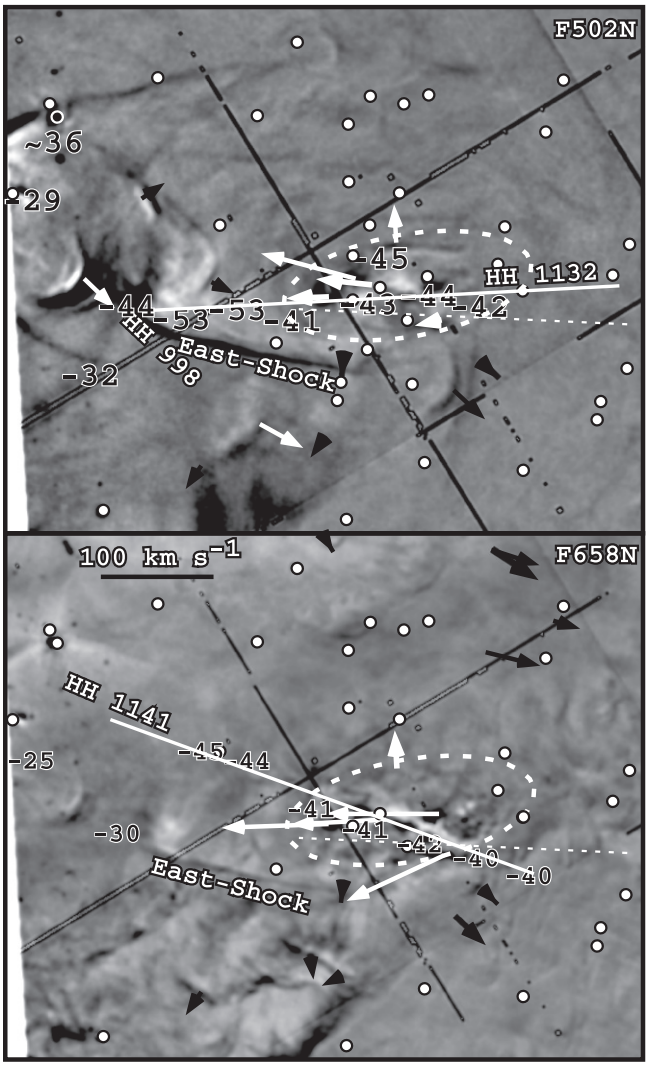

Figure 14. These east FOV motion images have the motions of the jet and features possibly associated with it as solid white arrows, except for the pair of F502N shocks associated with HH 998 (see Section 5.5). Features not associated with either system are shown with black arrows. The region including the east-jet is again shown by the white dashed ellipse. The thin dashed lines indicate the position of the approximate projection of the axis of the HH 269 features. The white line in the upper panel follows the symmetry axis of the east-jet along its full extent. The white line in the lower panel follows the symmetry axis of the east-second-jet in two segments. The black numbers indicate radial velocities.

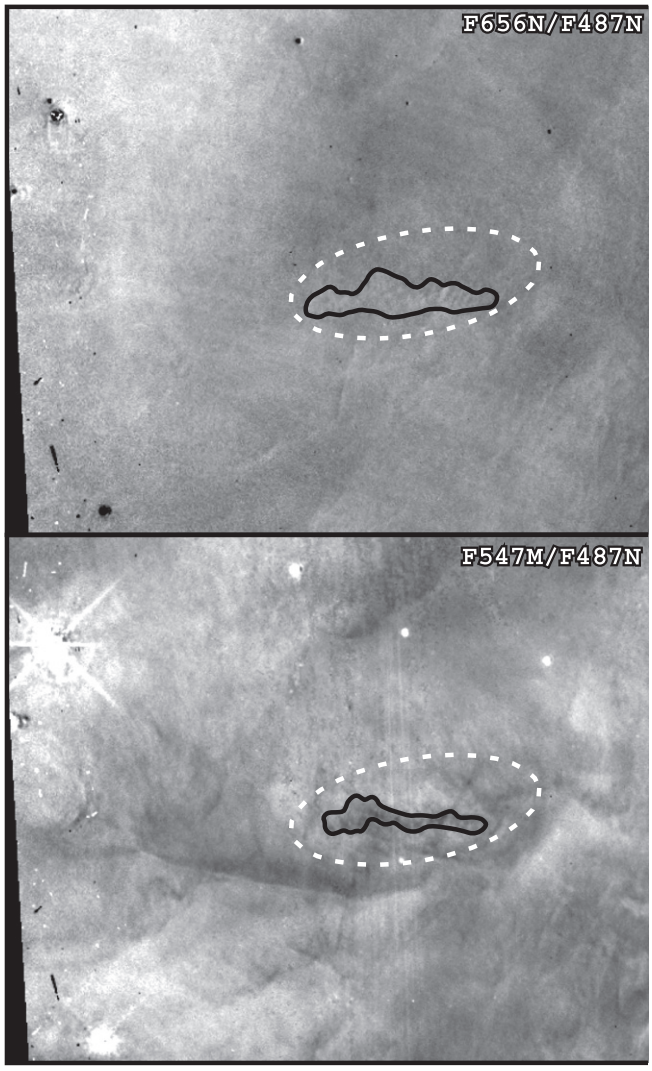

Figure 15. Local variation in the F656N/F487N ratio image is shown in the upper panel and the F547M/F487N ratio image in the lower panel. These are discussed in Section 3.2.2. The ellipse defines the same area as in Figures 13 and 14. The irregular dark-line outline in the upper panel identifies the area of fine-scale variations in the F656N/F487N image. The similar outline in the lower panel indicates the areas of low and structured values of the F547M/F487N images.

(best defined in [O III] radial velocities and [N II] tangential velocities) and an east-second-jet (defined by a single [O III] tangential velocity feature and seven [N II] radial velocity features). Using the east-jet [O III] V_r values and the [N II] V_T values gives a spatial velocity $V_{OMC} = 116\,km\,s^{-1}$ with $\theta = 32°$. Using the east-secondary-jet [O III] V_T values and the [N II] V_r values gives a spatial velocity $V_{OMC} = 114\,km\,s^{-1}$ with $\theta = 35°$. It appears that the east-jet is crossed in the plane of the sky by a similar jet (the east-second-jet).

The $-45\,km\,s^{-1}$ feature in the top part of the ellipse is probably associated with the expanding elliptical pattern that one sees in the [O III] tangential motion images. This pattern on the north and south sides of the ellipse enclosing the east-jet indicates that the geometric configuration is that the jet is breaking out from a source embedded within the Orion-S cloud. The identification of the probable source is discussed in Section 7.10, and the possible relation to the large high-ionization shocks composing HH 529 is discussed in Section 3.3.1.

Physical conditions within the east-jet are suggested by examination of Figure 15. The upper panel indicates that no big changes occur across the east-jet's region. However, one sees a pattern of subarcsecond changes within the ellipse enclosing the east-jet. The axis of those fluctuations is a fewer degrees lower (104°) and is similar to the PA suggested for the motions. These fine-scale changes in F656N/F487N may be caused by differences in T_e within the jet or small-scale changes in the extinction (in which case this would mean that the jet lies closer to the observer than the material causing the surrounding extinction). In the lower panel one sees that the value of F547M/F487N is lower along the same 104° region. This probably indicates that the light from the jet is mostly gaseous material (which has a low F547M/F487N emission)

superimposed on the high scattered light continuum radiation coming from the background PDR. These combined considerations indicate that the changes in F656N/F487N are due to the temperature in the east-jet being different from that of the nebular gas.

3.2.3. Properties of the East and West Regions

Definitive discussions of the stellar sources of the flows are presented in Sections 7.1–7.3.

In a parallel study led by co-author Henney we have isolated the auroral (575.5 nm) and nebular transitions (658.3 and 654.8 nm) of [N II]. The ratio of these line intensities I (575.5 nm)/I(658.3 nm + 654.8 nm) is mostly electron temperature dependent, with larger values indicating higher temperatures. The FOV covered includes the east-jet and the west-jet, and in both cases the jets have much larger values than the surrounding nebula. In the case of the east-jet the high-temperature features closely mimic the object as seen in F658N. In the case of the west-jet the high-temperature features resemble the west-jet in F658N until about 1″ west of the star 140.9-351.2. At that point the squiggly primary feature that defines the western end of the west-jet is no longer a well-defined high-temperature feature; rather, the high-temperature region is extended with many high-temperature knots. This region falls into a triangle defined by about 5:35:14.03, −5:23:51 on the east, 5:35:13.77, −5:23:49 on the north, and 5:35:13.72, −5:23:55 on the south. The western end of the west-jet lies along the middle of this extended region of high temperature.

3.3. The Eastern Systems

This section presents and examines the results for the region immediately east of the Orion-S molecular cloud. It is shown as HH 529 in Figure 2. It includes the OOS region originally identified as the common centers of several outflows (O'Dell & Doi 2003a, 2003b). Our new data have allowed a more accurate determination of tangential velocities and detection of patterns of motion. We begin with a discussion of HH 529, a well-known series of shocks moving east, and a new system designated as HH 1149. We then present the likely connection of this region to the large-scale objects HH 202, HH 203, HH 204, and HH 528. Where possible, the tangential velocities were determined from the combination of GO 5469 and GO 12543 images. East of the boundary passing through about AC Ori we used WFPC2 images from GO 5469 and GO 11038.

3.3.1. HH 529

The system called HH 529 was introduced in Bally et al. (2000) and was subsequently divided into three components (I, II, and III) by O'Dell & Henney (2008).

Our merged GO 12543 and GO 11038 images are shown in Figures 16–18. Examination of these figures shows that shocks HH 529-I, HH 529-II, and HH 529-III share a very similar structure in F502N, but HH 529-II is much fainter, and in contrast, none of these three shocks are visible in F658N. The spectroscopic study of HH 529-III by Blagrave et al. (2006) concluded from its ionization balance that this was a shock formed in fully ionized gas, thus accounting for the object's lack of visibility in F658N. The symmetry axis of HH 529-I and HH 529-III shocks is 109°, which passes through the less well defined crest of the HH 529-II bow shock.

In contrast with the single-epoch filter images, shocks HH 529-I and HH 529-III appear in both the F502N motion image (Figure 19) and the F658N motion image (Figure 20).

3.3.1.1. Features near the Newly Identified HH 529-east Shock

Our new analysis shows that there is an additional nearby shock that we designate as HH 529-east. The symmetry axis of it is about 84°.

The F502N motion image (Figure 19) also shows a faint series of moving knots centered 8.″3 east of COUP 769. The axis of these knots is about 82°.

3.3.1.2. Other Shocks near HH 529

There are other features that are associated with sources in this area, but they cannot be identified exactly. The shock 150-337 lies at 12.″2 from AC Ori toward 309°. There are no intervening candidate sources, although COUP 769 lies only 1.″8 beyond AC Ori.

F502N/F656N and F658N/F656N ratio images covering the entire Huygens Region show that there is an additional large high-ionization shock to the east of the OOS region. This may belong to one of the HH 529 outflows and is discussed in Section 4.5.

3.3.1.3. 3D Motion of HH 529-III

Of the several components of HH 529, we have combined V_T and V_r velocities for HH 529-III. Taking the average of the V_T values (7 km s^{-1}) and the average of the V_r values (−28 km s^{-1}) yields $V_{OMC} = 54$ km s^{-1} at $\theta = 83°$.

4. LARGE-SCALE FEATURES IN THE HUYGENS REGION

In addition to the HH 269 and HH 529 systems, there are several other large-scale flows that appear to originate in the same vicinity. In the following sections we will present (in the following order) the results for HH 202, HH 203+HH 204, and HH 528. We address their origins in Section 7.1.

4.1. HH 1149

The feature that we have labeled as HH 1149-CW in Figure 20 is a well-defined shock lying at the SE end of an extended region of moving shocks seen clearly only in F658N motion images. The symmetry axis of this easternmost shock is shown in Figure 20 and is about 120°. Although this shock lies near a line projected from the redshifted SiO flow arising from COUP 554 (Zapata et al. 2006), that flow has PA = 100°, and it cannot be driving this shock. There are a series of other shocks lying CCW from the HH 1149-CW feature that show a pattern of motion and symmetry with progressively larger PA, and they end abruptly at a complex linear feature (at 154°) in the lower right of the pattern. The CCW boundary is ill defined and can be drawn as segmented with the upper boundary at 160° and the lower at 168°. We designate this series of shocks as HH 1149.

The HH 1149 feature lies in a region of enhanced [N II] emission. An enhanced F658N/F656N ratio this close to θ^1 Ori C is an indication of viewing an ionization front nearly edge-on (Mesa-Delgado et al. 2011). This is why the eastern side of optical Orion-S images has high F658N/F656N and the west side does not. The abrupt CCW end of the fan of

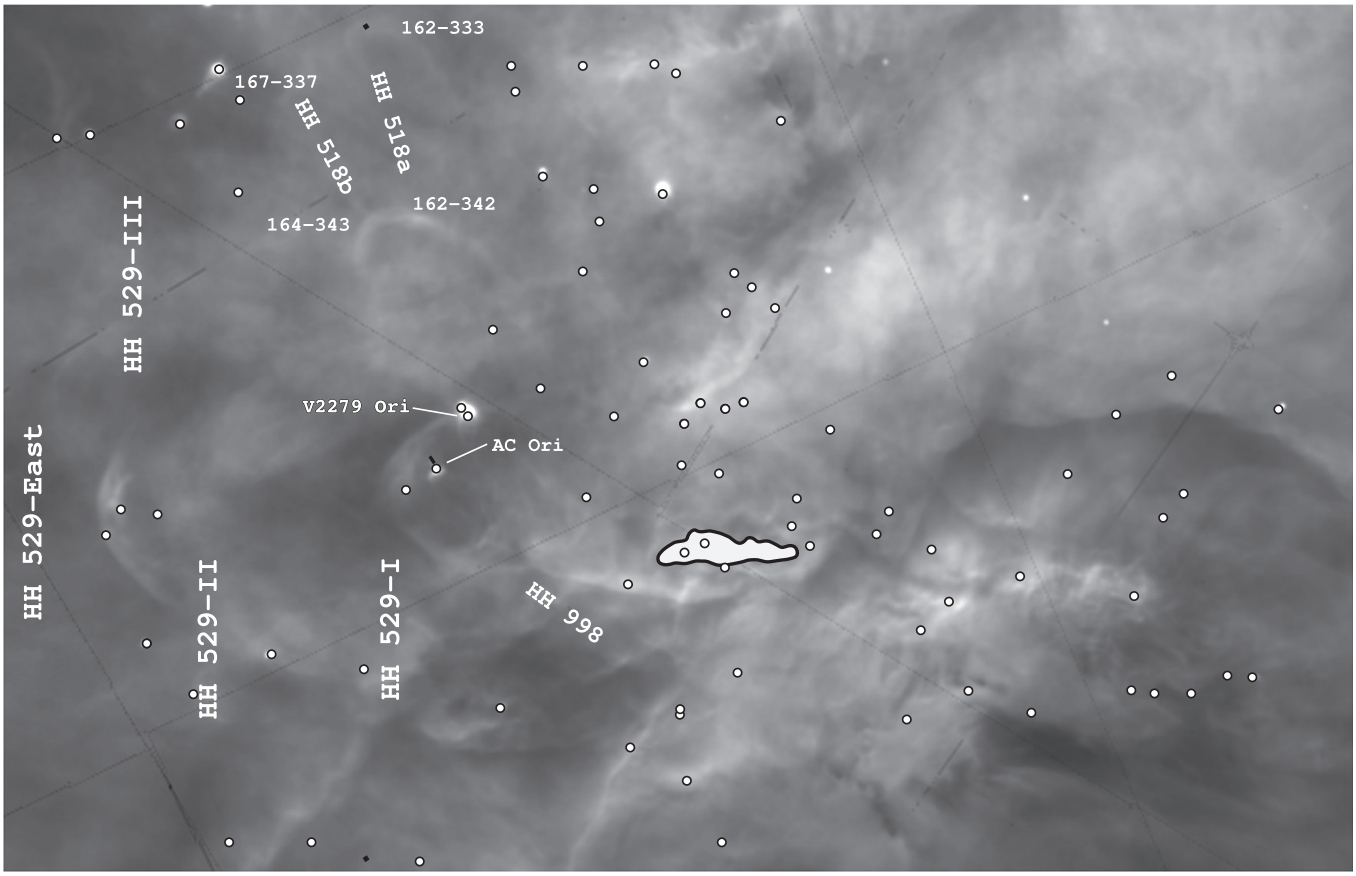

Figure 16. This $64\farcs6 \times 41\farcs5$ FOV is taken from the east boundary of the north FOV shown in Figure 2. It shows the F656N image. The breakdown of HH 529 into three regions (O'Dell & Henney 2008) is labeled, and a newly identified HH 529-east feature is added. The irregular closed bright line figure outlines the east-jet region identified in Figure 15 as having either fine-scale F656N/F487N or F547M/F487N changes. Two key stars (V2279 Ori and AC Ori) are labeled. The filled circles are compact sources from the SIMBAD listing.

HH 1149 shocks may indicate that they are overlaid by a step of material on the Orion-S east side. A problem with this interpretation is that one sees what may be an extension of the HH 1149 southern edge extending beyond the HH 1149-CCW boundary in the [N II] component of Figure 43.

The northern end of the CCW boundary (marked as HH 1129) may be due to structure in the west side of Orion-S, but the lower part (marked as HH 1129-Jet) lies on an extension of a linear feature arising from the star COUP 666 at an angle of 160° (Section 7.1.3). It is likely that the CCW boundary is part of a linear flow, hence the designation as HH 1129. There is a similar feature (marked HH 1149-Mid). Its axis is at 162°. It may be unrelated to the fan of bow shocks defining HH 1149.

In the material presented below we give the results of an analysis of the tangential velocities and in more detail the radial velocities. An analysis similar to that of the radial velocities but of the relative line intensities is given in Appendix D.

4.1.1. Tangential Velocities in and near HH 1149

HH 1149 appears only on the F658N motion images (Figure 20) owing to its low ionization and the presentation of multiple bow shocks. The tangential velocities of most of the features composing HH 1149 are low. Changes in structure prevent determination of tangential motions from the study of large-scale samples, but a few objects do have individual determinations, and these are never large. The five measured features have an average of only $V_T = 5\,\mathrm{km\,s^{-1}}$, and these are the larger motion features. The series of shocks are real, but the tangential motions are small.

4.1.2. Radial Velocities in and near HH 1149

No radial velocity features are seen in the Atlas, so that the radial velocities too must be small. Area-averaged spectra across the entire feature have been used to increase the S/N of the data. These area-averaged spectra have been compared with other area-averaged spectra within the Huygens Region. Henceforth we will call the area-averaged spectra "samples." The results of this comparison are presented later in this section.

4.1.2.1. The Area-averaged Spectra and Selected Results

We investigated the radial velocity properties in [O III] and [N II] of the HH 1149 object and the region just beyond it, labeling them as SHOCKS and Near HH 1149 (henceforth "NEAR"), respectively, in Figure 21. The SHOCKS sample was best fit into three components: a low-velocity component (henceforth BLUE) described in most detail by Abel et al. (2006), a component (henceforth MIF) identified with the MIF, and a high-velocity component (henceforth Red) due to backscattering from dust in the PDR behind the MIF (O'Dell et al. 1992; Henney 1994; Doi et al. 2004; Abel et al. 2006). The results are shown in Table 3.

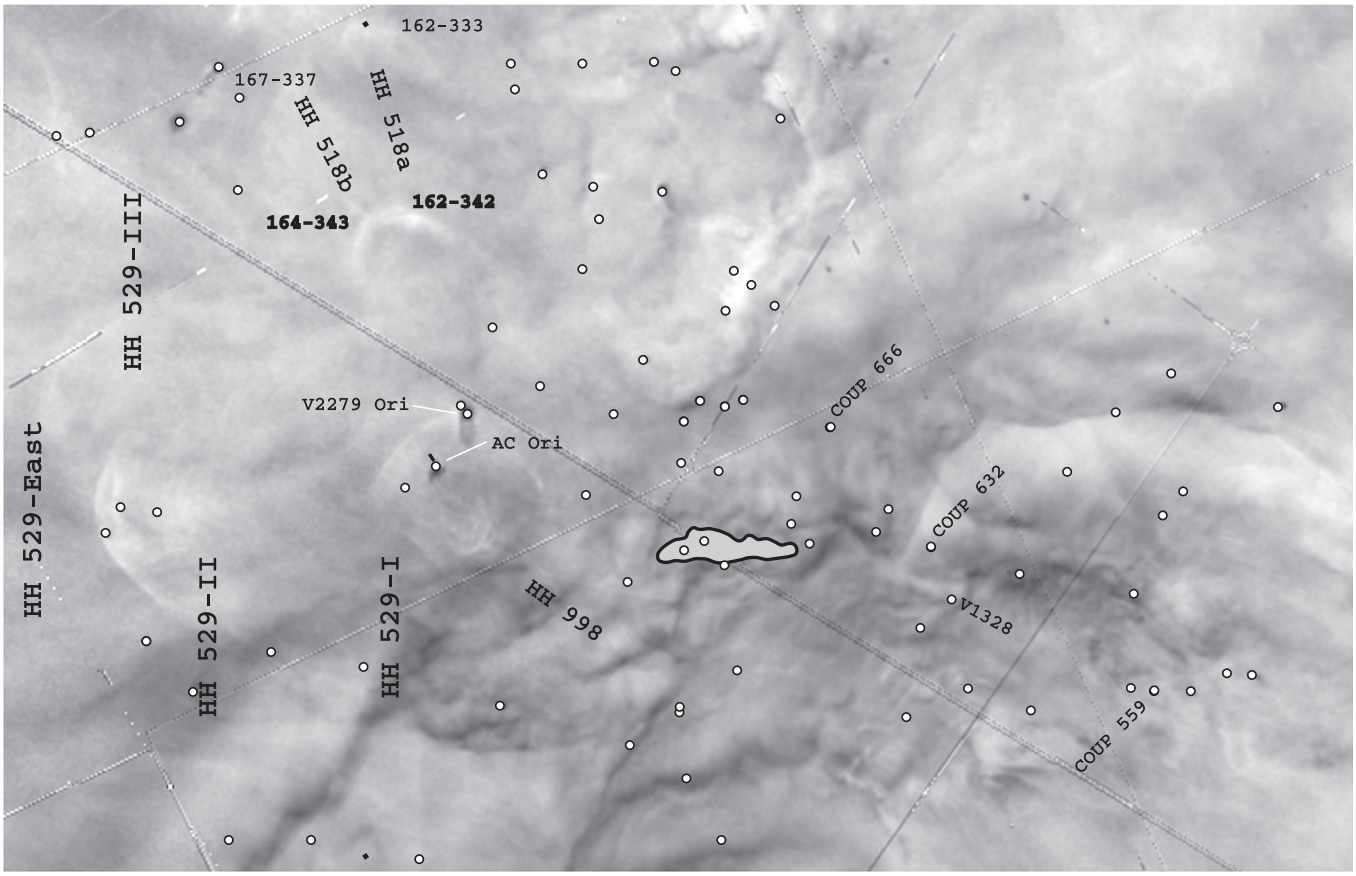

Figure 17. Like Figure 16, except that it shows the ratio image F502N/F656N.

We also created seven large area-averaged spectra as shown in Figure 21 within the Huygens Region for comparison with our SHOCKS and NEAR samples. The results for them are also given in Table 3. Some results were very different from the others and were not used in deriving averages. The [O III] MIF velocity for Sample-A was 14.7 km s^{-1}, and the [O III] MIF for Sample-G was 12.7 km s^{-1} (both of these are within the probable errors of the other samples, but as we'll see below, the [O III] emissions in these regions are anomalous). Sample-D was not used because its unusual value (7.8 km s^{-1}) for [O III] may be the result of blending with the blueshifted flow that drives HH 202.

The sample F [N II] BLUE velocity was not used because of contamination of that sample by proplyds and shocks. For comparison, the most complete compilation of radial velocities in the Huygens Region is that of García-Díaz et al. (2008), who find average velocities of V_r([O III]) = 16.3 ± 2.8 km s^{-1}, V_r(Hα) = 16.8 ± 3.0 km s^{-1}, V_r([S III]) = 19.7 ± 3.0 km s^{-1}, V_r([N II]) = 20.5 ± 2.9 km s^{-1}, V_r([S II]) = 21.2 ± 2.4 km s^{-1}, and V_r([O I]) = 25.7 ± 3.4 km s^{-1}.

4.1.2.2. The Most Important Radial Velocity Results

The purpose of the V_r study was to see whether there were detectable velocity differences in HH 1149. Since this object is only seen in [N II] and any differences will be near the MIF values, it is these velocities that were compared. For [N II] the large samples gave an average V_r(MIF) = 20.0 ± 1.9 km s^{-1}, the NEAR sample gave V_r(MIF) = 21.0 km s^{-1}, and for the sample on the object V_r(SHOCKS) = 21.9 km s^{-1}. This means that the NEAR sample's velocity was well within the scatter of the large samples and the SHOCKS sample's velocity was only at one standard deviation. The conclusion is that any systematic difference in radial velocity of HH 1149 must be very small (a few km s^{-1}); however, an alternative interpretation is that the HH 1149 shocks contribute little to the signal near the MIF velocities. The latter interpretation would be consistent with the fact that we only see HH 1149 clearly in the motion [N II] image and not the F658N image. In summary, we can only say that we cannot determine HH 1149 V_{OMC} values.

In the case of the analysis of the [O III] NEAR sample spectra the strongest velocity component (9.7 km s^{-1}) is similar to the typical blue component velocities, as discussed in Appendix D.

4.2. HH 202

The mixed ionization structure known as HH 202 was found by Cantó et al. (1980). It has been the subject of many studies since then, starting with early *HST* imaging (O'Dell et al. 1997b). It has a detailed, multi-shock structure that has been the subject of several radial velocity, tangential velocity, and physical condition studies (Doi et al. 2002, 2004; Rosado et al. 2002; O'Dell & Doi 2003a; García-Díaz et al. 2008; O'Dell & Henney 2008; Mesa-Delgado et al. 2009b, 2009a; O'Dell et al. 2009). The highly blueshifted [O III] jet delineated by Doi et al. (2004) also shows up in the He I study of Takami et al. (2002), although the source of the strength of the 1083.0 nm line was incorrectly explained there (Doi et al. 2004). It has already been established that the apex

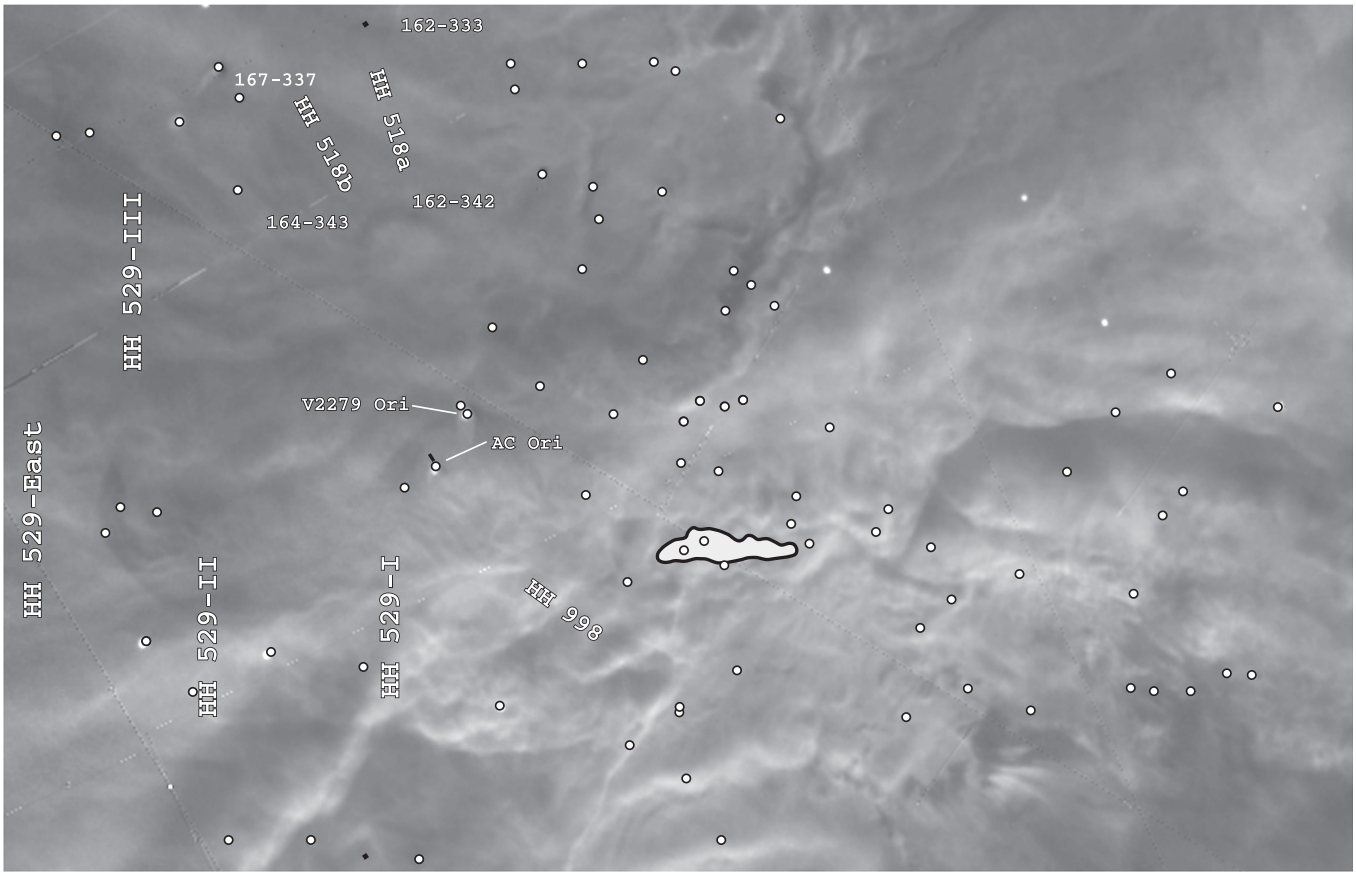

Figure 18. Like Figure 16, except that it shows the ratio image F658/F656N.

region of HH 202 is a composite of multiple shocks. We see in Figures 22 and 23 that the jet is pointed at the middle of a number of shocks. There are several clearly defined shocks extending NNW beyond the group usually identified as HH 202. The average of the four major components (O'Dell & Henney 2008) gives 68 km s^{-1} and $\theta = 51°$.

The jet that currently drives one or more features of HH 202 curves, and it is hard to extrapolate back accurately enough to identify the source. However, at an extrapolation of the jet's average path of 137° 18″ one finds COUP 666, which upon this criterion is a much more likely source than COUP 632. The rather approximate symmetry axes of the shocks slightly favor COUP 666. The apexes of the several shocks fall over a range of PA values (310°–319°). If the shoulders on the broadest shocks are taken as directions of other related shocks, the PA range increases (296°–327°).

4.3. HH 203 + HH 204

HH 203 and HH 204 were found by Munch & Wilson (1962). They appear as two overlapping but incomplete low-ionization parabolic shocks with quite different structures near their apexes. Henney et al. (2007) established from combinations of radial and tangential velocities that they have different (18°) angles with respect to the line of sight (HH 203, $V_{\rm OMC} = 104$ km s^{-1}, $\theta = 45°$; HH 204, $V_{\rm OMC} = 103$ km s^{-1}, $\theta = 27°$). This pair of objects has had their structure, radial velocities, and tangential motions well determined (Walsh 1982; Hu 1996; O'Dell et al. 1997a, 1997b; Doi et al. 2002, 2004; Henney et al. 2007; García-Díaz et al. 2008). HH 204 clearly shows that the volume behind the moving shock is photoionized by θ^1 Ori C. Their tangential motions are closely along their symmetry axes, and those axes point back to the vicinity of the OOS, although the distance to that region does not allow an association with a specific source. As indicated before, an association with the Orion-S region was made quite early (O'Dell et al. 1997a; Rosado et al. 2002), and the case became more compelling with the identification of jets of high-velocity material streaming toward them (Takami et al. 2002; Doi et al. 2004).

In Figures 22 and 23 we have drawn the high-velocity jet determined in [O III] by Doi et al. (2004), omitting the portions of high-velocity material that must be part of the shocks. The [O III] jet (124°) lies slightly CCW from a projection of the symmetry axis of the most CW shock belonging to HH 1149. Doi et al. (2004) also presented some evidence in [O III] for a much shorter jet feeding into the apex of HH 204.

Study of *HST* images and the location of the [O III] jet show that HH 203 is actually two parabolic shocks, with the brighter HH 203 shock (124°) being a partial shock front and a fainter component being more complete. Whenever relevant, these components will be designated as HH 203a (the brighter, partial shock) and HH 203b (the more complete, fainter shock fed by the high-ionization jet). The [O III] jet as delineated by Doi et al. (2004) does not exactly align with the brighter shock (HH 203); rather, it aims at a slightly more northerly position but with the same PA. Examination of Figure 23 shows that there is a well-defined smaller shock at the end of the jet; this is HH 203b.

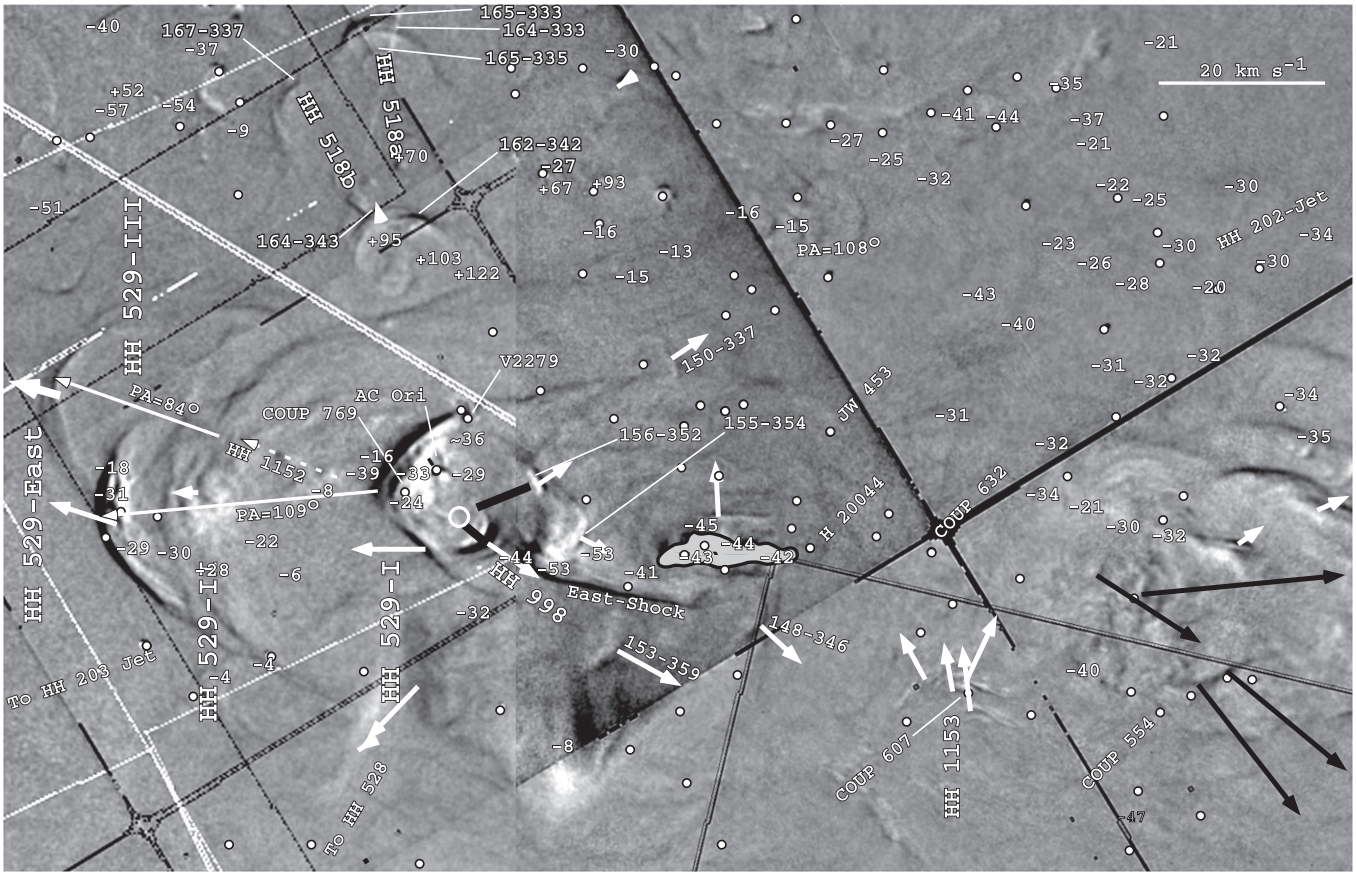

Figure 19. Like Figure 16, but showing the motion image for F502N. Motion vectors for F502N are shown. The solid thin white lines represent the several axes of the four HH 529 components, as discussed in Section 3.3.1. The thick black lines to the SW of AC Ori lie along the symmetry axes of three corresponding shocks, and the circle indicates the point of convergence of them as discussed in Section 7.7.2. The scale of the two rightmost velocity vectors is truncated in order to fit onto the figure. The numbers indicate the radial velocities in [O III], although not all are drawn in crowded areas that are subjected to detailed examination. The dashed line west of COUP 769 is a series of moving knots discussed in Sections 5.5 and 7.7.2. The trapezoidal dashed boxes indicate the regions likely to contain the sources of HH 529-I–III and HH 529-east.

HH 204 has a very different form (O'Dell et al. 1997b) from that of HH 203, the apex appearing as a mottled grouping of shocks. However, its sides are well defined, and the symmetry axis is 127°.

Henney et al. (2007) discovered that there is a larger shock (now designated here as HH 204b) feature with a PA slightly greater than that of HH 204, this fainter shock is large enough to include HH 203 within its CW boundary, and its CCW boundary extends to almost the PA of HH 528's Cap (Section 4.4). Its boundaries are shown as a white dashed line in Figure 24. It is not clearly seen in any of our Figures 22–24, but it is easily seen in Figure 7 of Henney et al. (2007).

Figure 23 shows an ellipse around the intersection of the axes of HH 203a and HH 204. This is in the same region of an inferred source found previously for other sources.

4.4. HH 528

HH 528 was discovered on early *HST* images (Bally et al. 2000), and its radial and tangential velocities have been documented (Bally et al. 2000; O'Dell & Doi 2003a; Henney et al. 2007; O'Dell & Henney 2008). It manifests itself by a series of small low ionization shocks (see the [O I] image in Figure 21 of Bally et al. (2000), the [S II] images in Figures 10 and 11 of Doi et al. (2002), and lower-resolution images in multiple ions in García-Díaz et al. (2008)) called in Henney et al. (2007) the jet.

O'Dell & Henney (2008) point out that the original nomenclature for HH 528 presented by Bally et al. (2000) is better, where the broad array of small low-ionization shocks are analogous to the "base" of a mushroom and the broad shocks lying just inside the Bright Bar to the "Cap" of the mushroom. The "Cap" feature is difficult to see in the much higher surface brightness of the Bright Bar. O'Dell & Henney (2008) report that the "Base" is oriented toward 155° (we judge it to be 169°) and moving toward 178° and the "Cap" is oriented approximately toward 146° with its components moving toward 159°. Figure 23 illustrates the direction but not magnitudes of the motions and some of the PA values for groups of features. Henney et al. (2007) determined that $V_{\rm OMC} = 11 \pm 3\,{\rm km\,s^{-1}}$ and $\theta = 24° \pm 8°$ for the feature that we call the HH 528 Base (illustrated well in O'Dell & Doi 2003a).

Figure 4 of O'Dell & Henney (2008) and our Figure 23 show new features SE of the base that we now separate and identify as part of two different systems of flow.

SSE of the HH 528 "Base" shocks we see multiple larger shocks aligned at about 163°, and a dashed white line is shown connecting them. They are labeled as the HH 528-west shocks. The location of the HH 528-west shocks with respect to the HH 528 Base and their similar PA values indicate that they may be

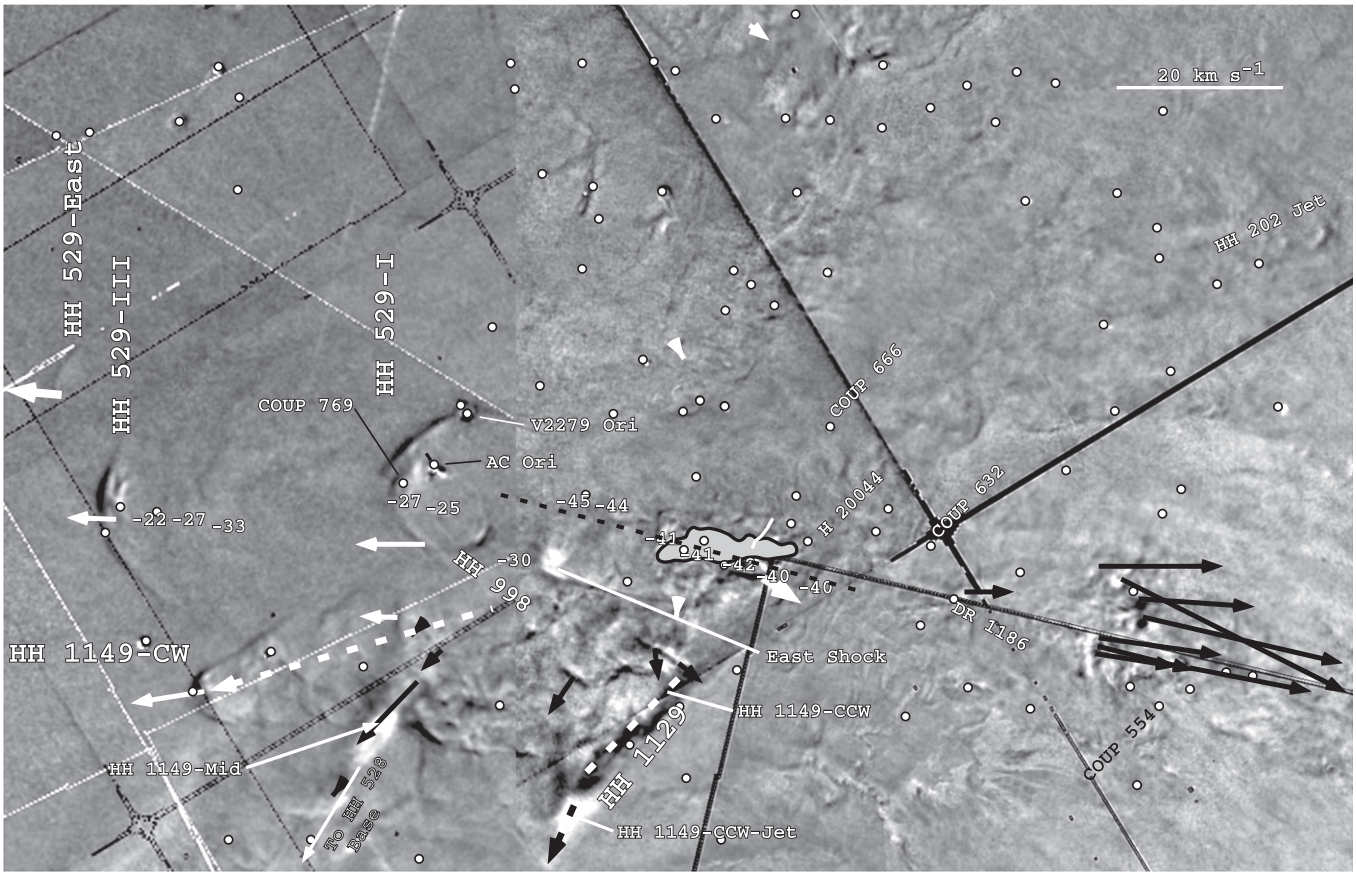

Figure 20. Like Figure 16, but showing the motion image for F658N. Motion vectors for F658N are shown. The dashed lines represent the boundaries of HH 1149, as discussed in Section 4.1. The dashed thin black line shows the average PA for the east-second-jet (89°). The scale of the rightmost three velocity vectors is truncated in order to fit onto the figure. The nearly linear white line crossing the east-jet is the [N II] strong feature seen in the lowest panel of Figure 12. The numbers indicate the radial velocities in [N II].

two parts of a common flow. The north end of the Base feature lies on the extension of the linear feature HH 1149-Mid (Section 4.1). To the east of the HH 528-west shocks we see two well-defined large shocks with a symmetry axis pointing both toward the "cap" feature and back toward the north end of the Base. The HH 528 east shocks and the "cap" feature are probably part of a common flow, which we'll call here HH 528-east. A line projecting NW from the HH 528-east flow passes (after crossing the HH 528 Base feature) several small moving features and then passes a few arcseconds south of the CCW boundary of HH 1149. With a slow CW change of PA over this track it points to star COUP 632.

4.5. Large-scale Shocks near and beyond the Bright Bar

The Bright Bar is well established to be a tilted region in the MIF, where one is looking almost along the MIF. This explains that we see a narrow streak of low ionization (F502N weak) that is bright in F658N. Most of the Bright Bar is marked by very sharp ionization boundaries with dimensions of about 0.″2. Farther from the Trapezium the MIF flattens out, but not so much that it is not illuminated directly by θ^1 Ori C. This means that the features we see beyond the Bright Bar are probably seen in projection on the MIF, rather than being formed in the MIF.

4.5.1. The HH 203 and HH 204 Shocks

It has been argued that the HH 203 and HH 204 shocks are produced when collimated flows from the OOS region strike the upper part of the escarpment caused by the tilt of the MIF (Doi et al. 2004). The original interpretation was that it was the result of collimated flows striking the foreground Veil (Doi et al. 2004), which became unlikely when it was argued that the Veil was about 1 pc from θ^1 Ori C (Abel et al. 2006; Henney et al. 2007). Now the pendulum has swung, and van der Werf et al. (2013) have presented evidence that the Veil is sufficiently close that the shocks must arise there.

There is a large irregular form (similar to two parallel but shifted parabolas) that is outlined with long-dashed lines encompassing HH 203 and HH 204 in Figure 24. It is of high ionization, being bright in F502/F656N and faint in F658N/F656N. There is a shorter and less clearly bounded adjacent region of high ionization just beyond the CCW edge of the SW-Gap (see Section 4.5.2). The CW form agrees well in position along the Bright Bar with the 21 cm absorption feature L in the study of van der Werf et al. (2013), but the optical feature extends farther away from the Bright Bar.

At the CW edge of the above feature there is a well-defined partial shock, shown as a short-dashed curved line in Figure 24. It is too incomplete to argue for an orientation except to say that its axis points somewhere between the OOS and the Trapezium.

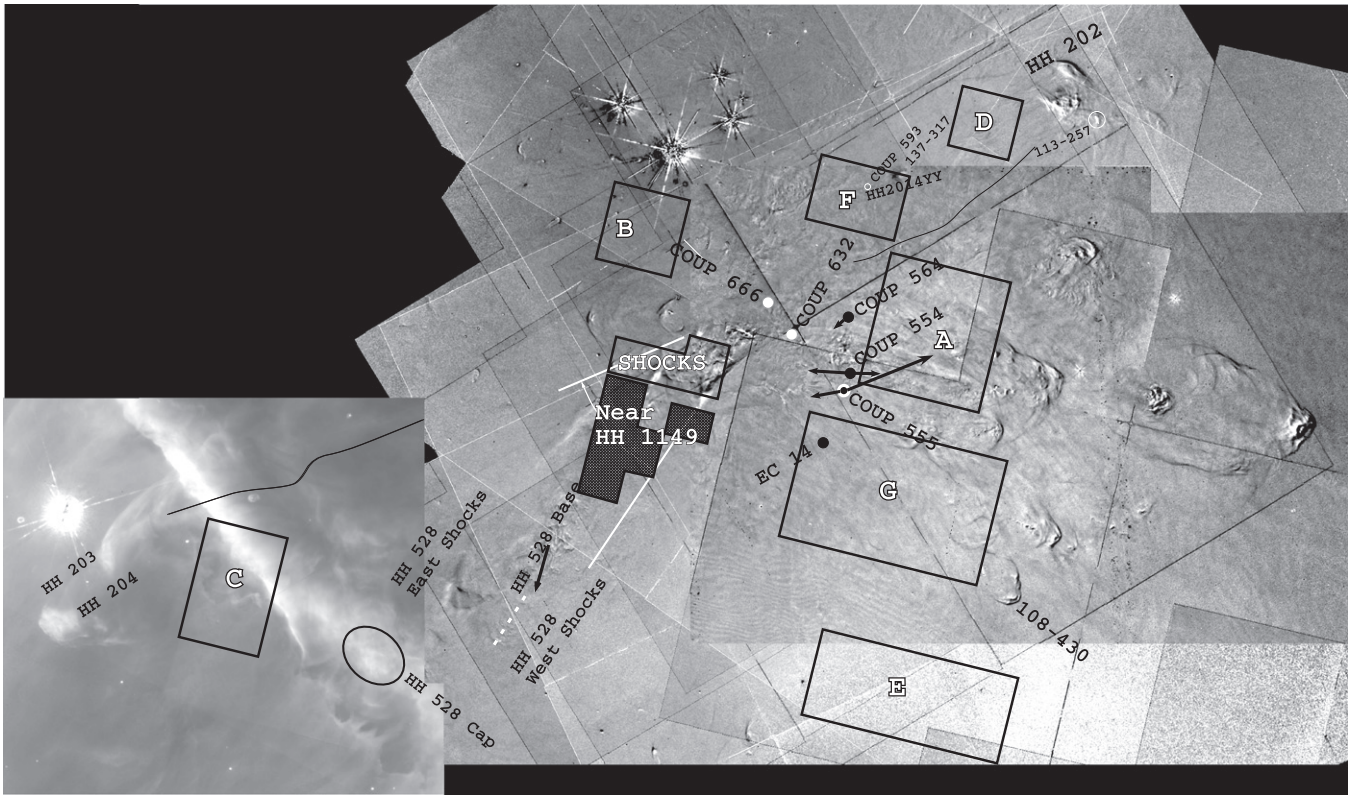

Figure 21. This 260.″1 × 120.″5 FOV (see Figure 1, where this FOV is shown) shows the region sampled in F658N, numerous individual features, and area-averaged spectra samples (A through G) used in Section 4.1 for comparison with the irregular samples used for analysis of HH 1149. The "SHOCKS" sample includes only an area within HH 1149, and the "Near HH 1149" sample includes an area immediately outside of HH 1149. The arrows indicate known molecular outflows. The filled white circles near the center represent the positions of the stars COUP 666 (upper left) and COUP 632 (lower right).

Table 3
Data for the HH 1149 Samples and the Large Samples[a]

Sample Name	Component	V_r [N II] (km s^{-1})	V_r [O III](km s^{-1})	$\frac{S(\text{MIF}-\text{O III})}{S(\text{MIF}-\text{N II})}$	$\frac{S(\text{BLUE}-\text{N II})}{S(\text{MIF}-\text{N II})}$	$\frac{S(\text{BLUE}-\text{O III})}{S(\text{MIF}-\text{OIII})}$
Large Samples	MIF	20.0 ± 1.9 (7)	15.5 ± 2.6 (4)	0.60 ± 0.11	0.07 ± 0.05(6)	0.17 ± 0.09(4)
…	BLUE	1.3 ± 2.5 (6)	2.6 ± 2.2 (5)	…	…	…
SHOCKS	MIF	21.9	17.0	0.29	0.02	0.06
…	BLUE	−4.7	1.1	…	…	…
NEAR	MIF	21.0	9.7/20.9	…	0.06	…
…	BLUE	2.9	…	…	…	…

Note.
[a] Numbers in parentheses indicate the number of samples used in deriving the averages.

4.5.2. Crenellations

Beyond the Bright Bar (to the SSE) we see a number of crenellated structures that lack the bow shock form of HH 203b, HH 203a, and HH 204a but are likely to be shocks driven by flows from the region of the OOS.

The first group occurs just beyond the HH 528-Cap feature and is easily visible in both the F502N/F656N image and the F658N/F656N image shown in Figure 24. These features occur in a region where the Bright Bar lacks a crisp SE boundary, a region labeled "SW-Gap" in Figure 24. The most visible of these features occur between the projection of the CCW edge of HH 1149 (160°), which points back toward the vicinity of COUP 666, and a wide high-ionization linear feature (HH 1149-Mid) with 162°. Given the wealth of shocks in HH 1149 within this PA range, it is very likely that these are bow shocks forming in the tilted portion of the Bright Bar or the foreground Veil.

Proceeding NE along the bright bar, we see that there are a series of similar features that begin at 135° and extend to the axis of HH 204b (127°). Again, the Bright Bar lacks a crisp boundary along most of this region.

There are a group of features similar to the crenellated features that are found inside the Bright Bar. These are designated as the SW-Group in Figure 24. They have individual designations of 147-532, 144-523, and 137-519. They lie at 184° from COUP 666 as shown in Figure 24.

4.5.3. Features inside the Bright Bar

Inside the Bright Bar we see a thick and wide arc that is probably a bow shock. It appears to have two peaks, one in the direction of HH 203 and the other in the direction of HH 204. It is almost certainly related to those shocks and the outflow in this direction arising from near the OOS. It is outlined with a thick short-dashed line in Figure 24.

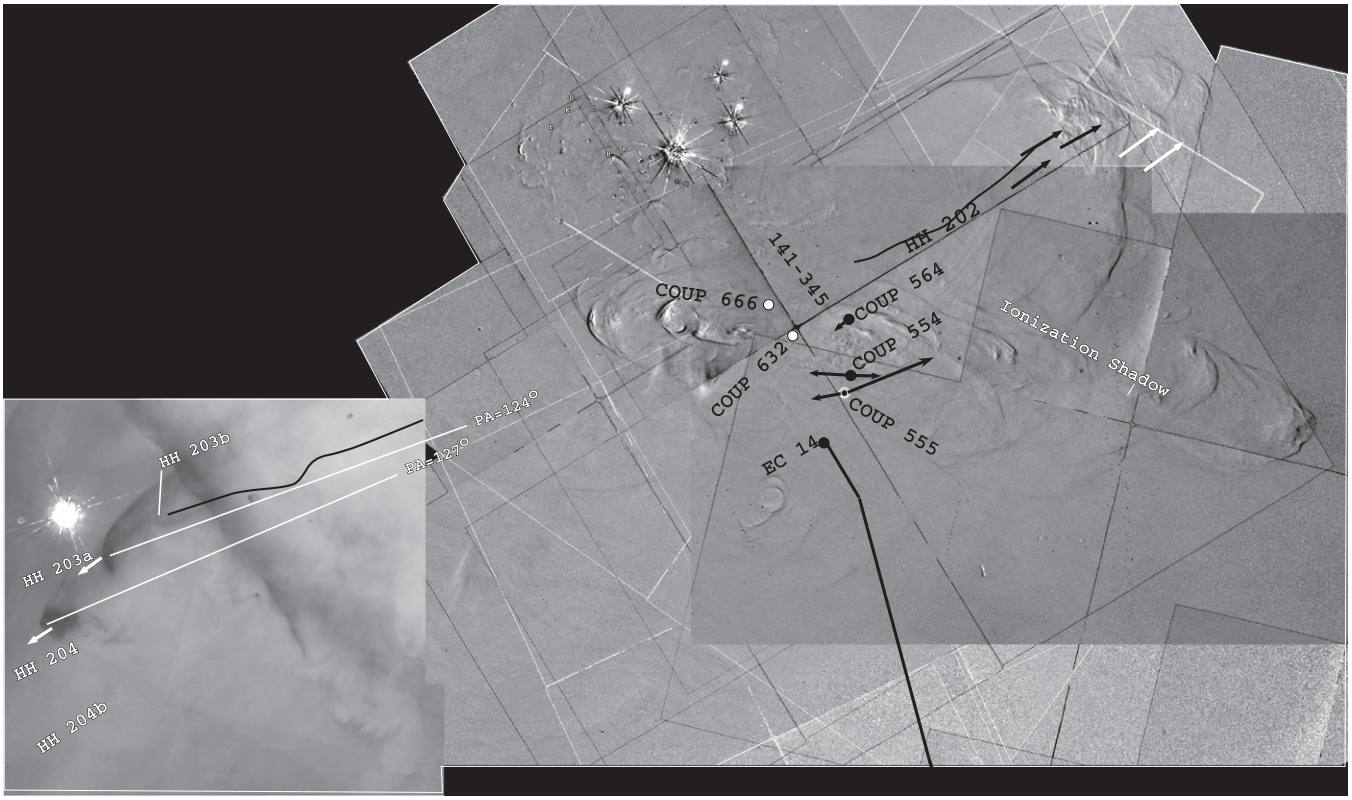

Figure 22. This 260″.1 × 120″.5 FOV (see Figure 1 where this FOV is shown) shows an F502N motion image, except for the inset at the lower left, which is a ratio image of F502N/F656N. The irregular dark lines leading to HH 202 and HH 203 are the blueshifted jets reported in Doi et al. (2004). Candidate stars for the major optical outflows (COUP 632) are shown with white filled circles, and the candidate sources for the major molecular outflows (COUP 554, COUP 564, and EC 14) are shown with black filled circles. The star COUP 555 that is the source of both a molecular outflow and the HH 625 optical HH object has a white circle. The molecular outflows are shown with straight thick vectors, except for EC 14, where it is known that the molecular jet (Zapata et al. 2013) changes PA near the source. The letters A–F refer to shocks that are part of the HH 518a and HH 518b flows (Section 5.2). The HH 1149 shock is too faint to be seen on this image, but its position is shown.

An isolated high-ionization shock labeled "East Shock" in Figure 24 may be related to the outflows associated with the HH 529 components, but it is impossible to determine its direction because only part of the bow shock is seen. The feature is on the east side of a broad bow shock formed feature that continues to the south, reaching an apex at about 80°.

4.5.4. The SW Spoked Feature (SWSF) Pointing inside the Bright Bar

Along the SW portion of the Bright Bar imaged in Figure 24 is an unusual object that we label as the "SWSF." It is a region with a concave feature that resembles a composite of three bow shocks pointed NNW, and with a base of 49″. Within the concave feature there are five nearly linear features, best seen in the F658N/F656N panel of Figure 24. These features converge on 5:35:13.7, −5:25:56 with a scatter of only a few arcseconds. There are no features in SIMBAD there. The sharp boundary of the Bright Bar continues below the east portion of the SWSF but then has a gap of 12″. It resumes and continues with decreasing brightness to the SE. Just beyond the west boundary of the SWSF, a new sharp boundary begins (off the FOV in Figure 24; see O'Dell & Wong 1996) and becomes the brighter sharp boundary during the region when the Bright Bar has two, nearly parallel sharp fronts.

Although it is tempting to assign the origin of the SWSF to the point of convergence of the projection of the eponymous spokes, the source may be more distant. There may be an association with the NNW components of HH 540. The NW center of the SWSF lies at 182″ toward 325° from the proplyd 181-826 (Bally et al. 2005), which is the source of the HH 540 flows, and close to the symmetry axis of the SWSF shocks (323°). Bally et al. (2005) assigned two shocks to the NNW of 181-826 as part of its system. The nearer shock (HH 540 N2) is the better defined and lies at 46″ and 337°. There are two shocks lying farther NNW from HH 540 N2 at smaller position angles (the closer called HH 540 N1). These angles are very similar to the symmetry axis (about 341°) of the curved rings that give 181-826 the descriptive nickname (if one recalls mid-twentieth-century cartoons) the Beehive (Bally et al. 2006a). Bally et al. (2006b) demonstrate that shocks from long collimated flows commonly are curved away from the Trapezium and/or the center of the Huygens Region. If the position of the HH 540 N2 and its farther companion are at smaller PA values because of curvature, there is no relation of the SWSF and 181-826. Of course, the association may still be valid if the SWSF is the result of a different period of collimated outflow under conditions where the curvature is less (e.g., higher-velocity collimated flow from 181-826).

There may be another feature that is related to the NNW outflow in HH 540. It clearly appears in the first *HST* (WFPC2) mosaic of Huygens Region images (O'Dell & Wong 1996) and the more recent ACS mosaic (Henney et al. 2007) as a parabolic high-extinction area lying to the NNW from the SWSF. It stands out in the high-resolution extinction map of O'Dell & Yusef-Zadeh (2000), where it was first called the SW Cloud. The tip of its parabolic form is at 112-436, and the axis of symmetry is about 343°. The tip lies at 480″ and 348° from

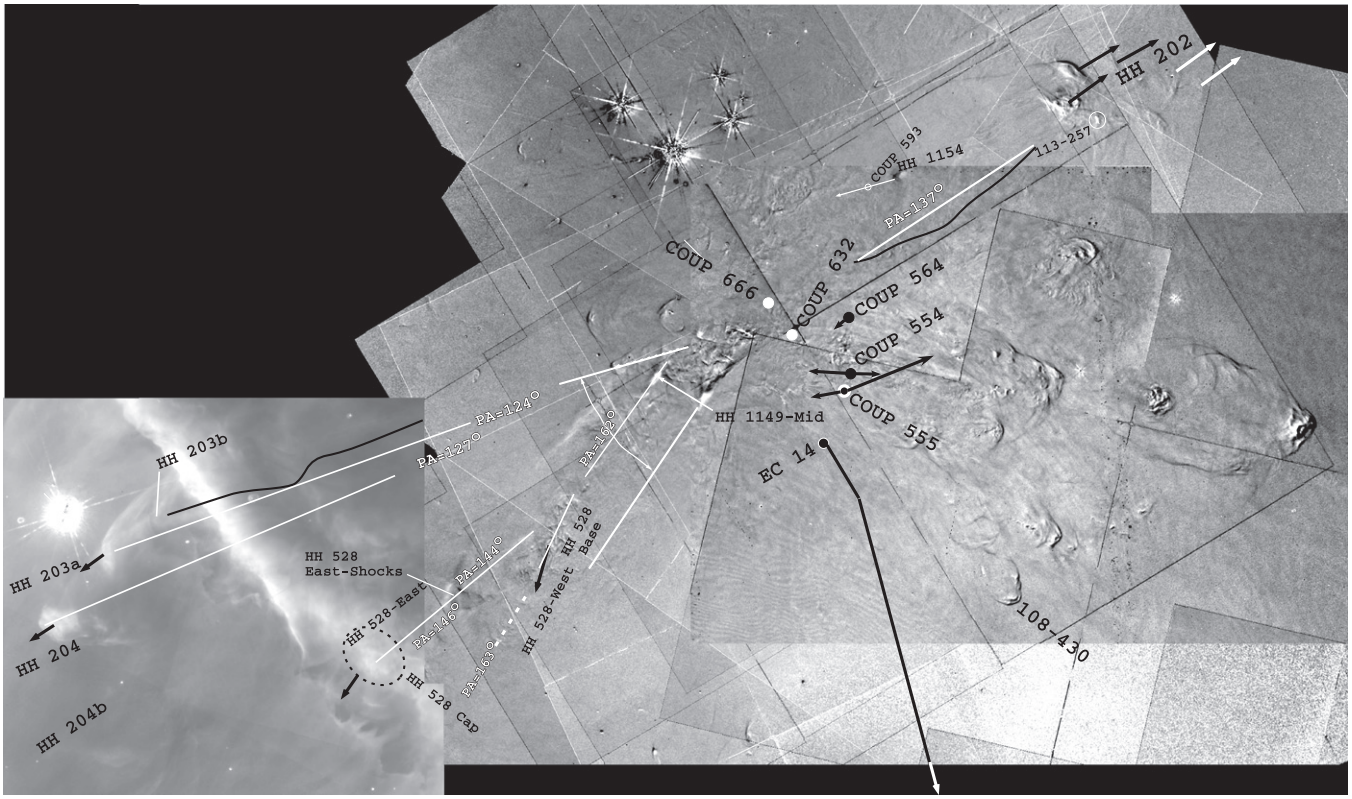

Figure 23. Same as Figure 22, except for depicting F658N data. The thick white lines with an enclosed arc identify the boundaries of the series of low-ionization shocks that include HH 203 and HH 204. The thin white arrow shows the motion of object shock with a tip at 136.5-317.5 (designated as HH 1154) near the proplyd 139.2-320.3 (COUP 593). HH 1154 is discussed in Section 5.9. The irregular dark lines aimed toward HH 202 and HH 203 are high-velocity jets (Doi et al. 2004). The white lines with PA values are reference lines discussed in the text. The HH204B shock is too faint to be seen on this image, but its position is shown. The white dashed ellipse shows the region of the intersection of the symmetry axes of HH 203a and HH 204a.

the HH 540 source 181-826. Although its PA and symmetry axis are not as close to the HH 540 features as SWSF's, this may be due to the fact that the velocity and angle of the 181-826 outflows have changed with time.

A caveat arguing against the association of the SW Cloud and HH 540 is that one sees within it a series of narrow arcs of high extinction over 40″ along 277° and ending at 102-453. These are similar to features seen within and at the west end of the Dark Bay high-extinction feature east of the Trapezium (O'Dell & Yusef-Zadeh 2000).

4.5.5. Opposite Flow through a Gap in the Bright Bar

There is an additional gap in the sharp boundary of the Bright Bar that is labeled in Figure 24 as the NE-Gap. There is a set of shocks nearby whose alignment is indicated by a short-dashed straight line (unfortunately, there is a scar from combining the early WFC CCDs nearby, and it is indicated by a long-dashed straight line). These shocks, together with several less obvious and smaller shocks between the two ends, indicate motion away from a source at 87°. There are no obviously good candidate sources nearby in this direction. The diffuse feature shaped like a seahorse (looking left in Figure 24) is low ionization and is not in alignment with the NE-Gap shock system; however, it is likely that this feature is caused by the same flows producing the NE-Gap shocks.

The NE-Gap does not appear upon a projection of the axis identified for HH 529-east or for HH 529-III (Section 3.3.1), and the forms of its features all indicate a motion in the opposite direction (west).

The van der Werfs (2013) 21 cm absorption feature D is a C-shaped configuration oriented toward the WNW. The optical features of the NE-Gap system fall into the middle of this structure. It appears that the optical parts are impinging on neutral material in the foreground Veil, producing the high-density, high negative radial velocity component observed at 21 cm.

4.6. HH 625

HH 625 was identified as a structured, moving feature that could be identified as an HH object by O'Dell & Doi (2003a), who first measured its tangential motion (as 26 km s^{-1}) at a point on the farthest extent of the leading edge. Our new observations (Figures 25 and 26) show that the symmetry axis is toward 324° ± 3° and that the tangential velocity is 30 ± 9 km s^{-1} toward 311° ± 21° as measured at the leading three points. In Figure 1 we see that there is a high-velocity He I feature at the leading edge of the object. O'Dell & Henney (2008) give $V_r = -8$ km s^{-1}. Combining this radial velocity with our new tangential velocity gives $V_{OMC} = 45$ km s^{-1} and $\theta = 49°$.

O'Dell & Doi (2003a) made an association of the brightest portion with H_2 features to the southeast (Kaify et al. 2000) (Figure 26), where we have added outlying curved features in the Kaify et al. (2000) images and the series of H_2 knots identified by Stanke et al. (2002). The Stanke and McCaughrean knots begin at a direction of 313° and curve slightly CW out to a distance of 204″.

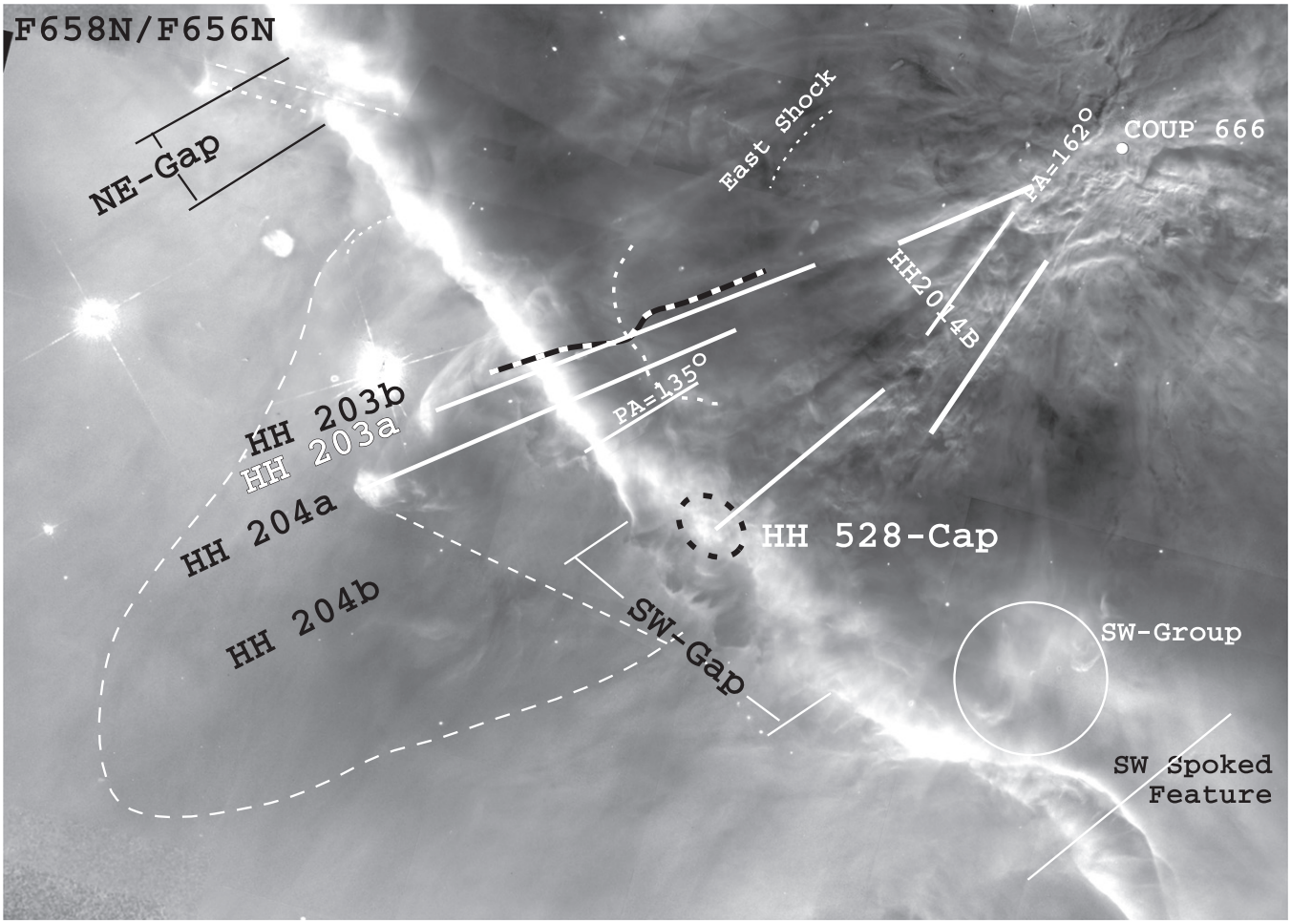

Figure 24. This ratio image samples a 232″ × 166″ FOV shown in Figure 1 and is taken from an early mosaic of the Huygens Region using the *HST* WFPC2 (O'Dell & Wong 1996). The two long-dashed straight lines indicate flaws at the intersection of two separate FOVs. The marked features are discussed in Section 4.5. The position of COUP 666 is shown as a white filled circle in the upper right of the image. The alternating black-white line shows the position of the high-ionization jet directed toward HH 203b.

4.6.1. Source

O'Dell & Henney (2008) argued that the bipolar CO flow from the embedded source COUP 555 (136.0-359.0) is the most likely driving source for HH 625. In light of the new data, it is worth examining whether there are alternative driving sources. The strength of the aligned H_2 features and the richness of low-ionization features in HH 625 itself argue that the object is breaking through an ionization front (see Section 1.3), and this favors an embedded source, but it does not exclude an optical source since the optical extinction in a column sufficient to form an ionization front is not great. The first two candidates discussed below must be embedded as they have no detected optical counterparts.

Associating HH 625 with COUP 555 requires that the CO flow curves, a not unusual feature in long outflows and one that can be explained by passage of the collimated outflow through ambient material of differing density (Cantó & Raga 1996). As mentioned above, O'Dell & Henney (2008) used the radial velocity data of (Doi et al. 2004) to determine that the radial velocity of HH 625 was $-8\,\mathrm{km\,s^{-1}}$. In contrast, the CO blueshifted flow (Zapata et al. 2005) from COUP 555 is traced out to $V_r = -36\,\mathrm{km\,s^{-1}}$. If the shocks of HH 625 are driven by COUP 555, then the slower velocities in the shock would require that the HH 625 features are mass-loaded shocks.

COUP 554's blueshifted outflows have heliocentric radial velocities of -62 to $-2\,\mathrm{km\,s^{-1}}$, which makes it a good alternative source for HH 625, but that identification would require an even greater deviation in direction than COUP 555 before reaching HH 625. An association is unlikely.

V1228 lies immediately at the end of the H_2 features that appear to be associated with HH 625. This object is unresolved on our *HST* images, and there is no indication of a microjet. It has an optical image (V1228 Ori) and falls exactly at the end of a curving H_2 feature that leads to HH 625.

The selection between V1228 and COUP 555 depends on one favoring a source (COUP 555) with a known blueshifted molecular flow (but requiring a deflection of the flow) or a closer fainter star (V1228) linked to HH 625 by an elongated H_2 feature. The deciding factor is the fact that HH 625 appears to be breaking through an ionization front, which favors the embedded star COUP 555 as the source.

The tangential motions of HH 625's leading edge are not moving along the line of symmetry of the feature. As one examines the shocks in a CW progression around the leading edge, one sees a progression to smaller PA values, and the feature in the expected position of a Mach disk and another to its east share the direction of motion of the CW portion of the leading edge. At 11.″5 to the northwest from the leading edge

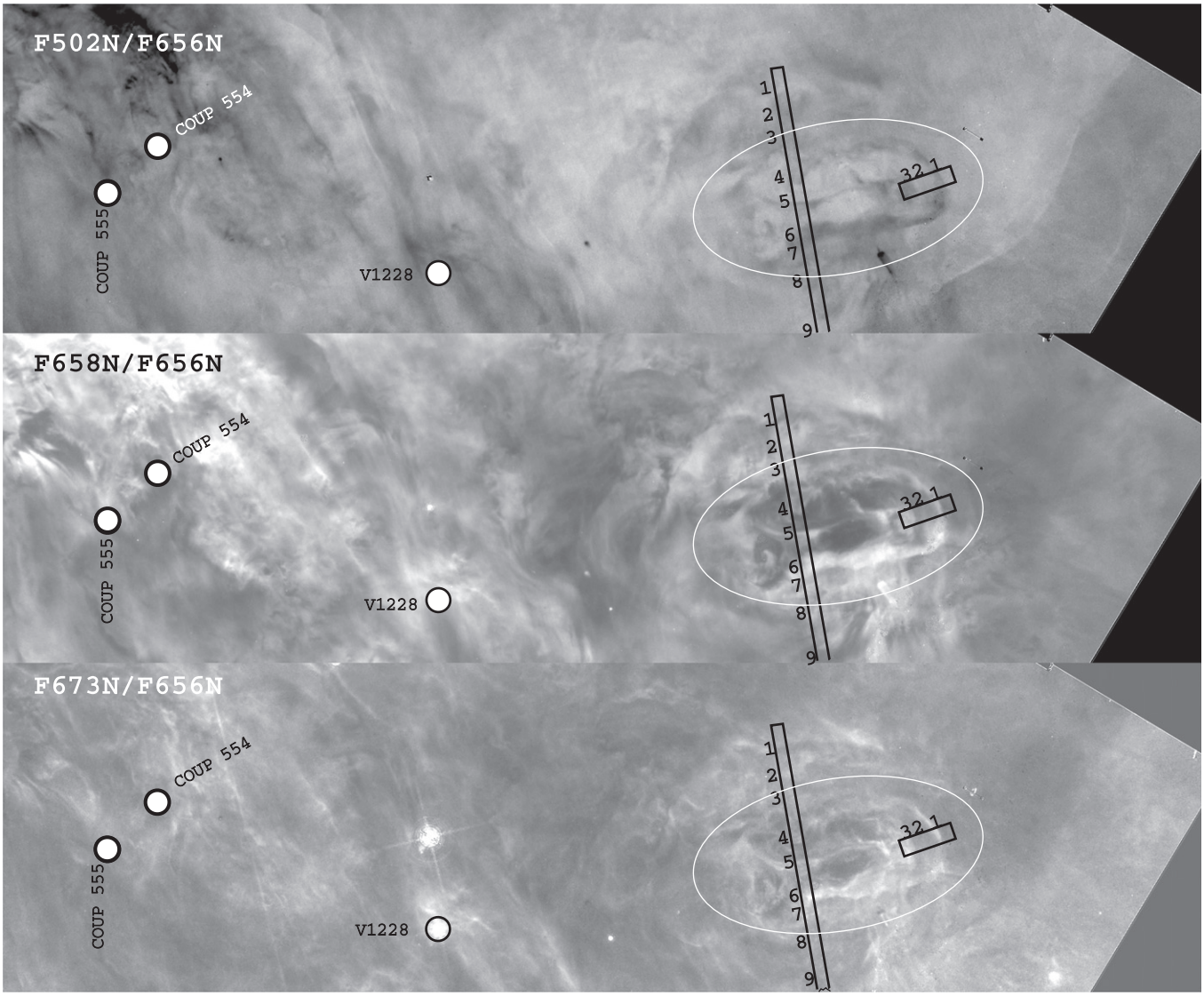

Figure 25. These three ratio images show the ionization structure of HH 625 (designated with a white ellipse here and in the next figure). The irregular FOV is shown in Figure 1 and is 80″ wide and 22″ high, with the positive vertical axis pointed toward 45°. The F656N/F487N (Hα/Hβ) is constant over this FOV to a few percent, indicating that there is little effect of location wavelength-dependent extinction when using the higher-S/N F502N/F656N images as an indicator of low-ionization regions. The positions of the three candidate sources for HH 625 are shown as filled circles. The numbered rectangles shown are where the profile samples discussed in Section 4.6.2 were taken.

there is a large shock, seen in both the F502N and F658N motion images (Figure 26). Its axis of symmetry falls between that of the overall HH 625 feature and the CW components of the leading edge. It may be the product of two flows.

4.6.2. Structure

We see in Figure 25 that HH 625 lies within a region of high ionization (high F502N/F656N, low F658N/F656N). However, its immediate surroundings (a circle of about 20″ diameter centered about the middle of the long profile in Figure 25) are of lower ionization. This indicates that HH 625 is affecting its surroundings. Since it is of low velocity, shock heating on a large scale is unlikely to be important, and it is more likely that the local gas density and the form of the ionization front have been modified by the penetration of the jet's gas column.

Examination of an axial profile of the F656N brightness and various line and continuum ratios, as shown in Figures 27 and 28, is useful in determining the structure of HH 625. In this analysis it must be kept in mind that much of the radiation along a line of sight occurs in the foreground or background, so that small-scale changes probably represent large-scale changes in the object. In Figure 27 feature 1 occurs at the bright leading edge of the object. The profiles show that F656N increases there, while the high-ionization tracer (F502N/F487N) drops and the low-ionization tracers (F658N/F656N and F673N/F656N) increase. This is the behavior that one expects from a tilted ionization front. The measure of the relative strength of the continuum as compared with the Hβ recombination line (F547M/F487N) drops at feature 1. If the continuum was dominated by atomic emission, the recombination coefficients for Hβ and the optical region emissivities of Osterbrock & Ferland (2006) would mean that the electron temperature at this ionization front has decreased, which is the opposite to what is expected from photoionization models that incorporate radiation hardening near the front itself. However, it is well established (O'Dell 2001) that the continuum in the Huygens

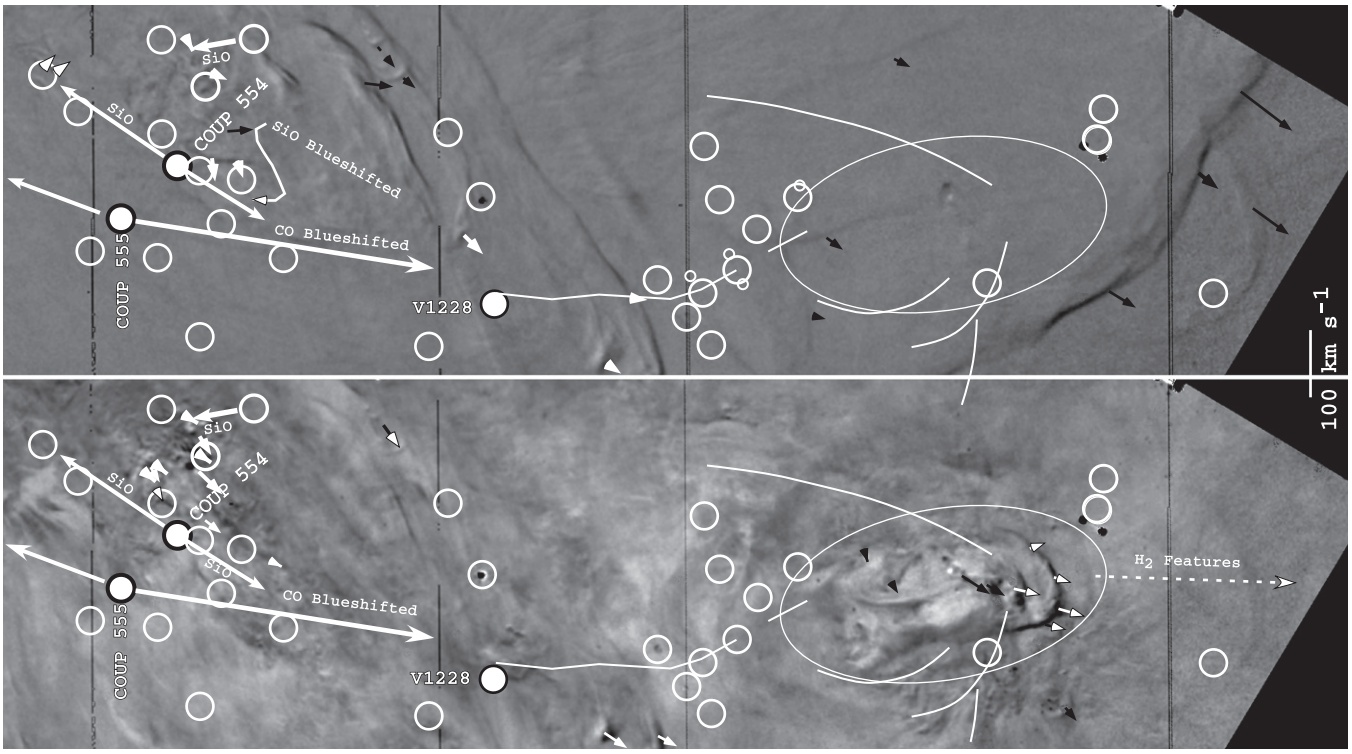

Figure 26. The same FOV as Figure 25 except that now motion images are shown with F502N images in the upper panel and F658N images in the lower panel. Velocity vectors most likely connected with HH 510 (see Section 5.1) have not been shown. Compact sources included in the SIMAD database are shown as circles or filled circles. The candidate sources (two with molecular outflows) are shown as filled circles and have the extent of any outflows shown as thick straight lines (Zapata et al. 2005, 2006). The small open circles are compact H_2 from Kaify et al. (2000). Extended H_2 features in Kaifu et al.'s images are also shown as thin white lines. The dashed line marked as "H_2 features" indicates the direction to the nearest H_2 feature in the chain of knots discovered by Stanke et al. (2002).

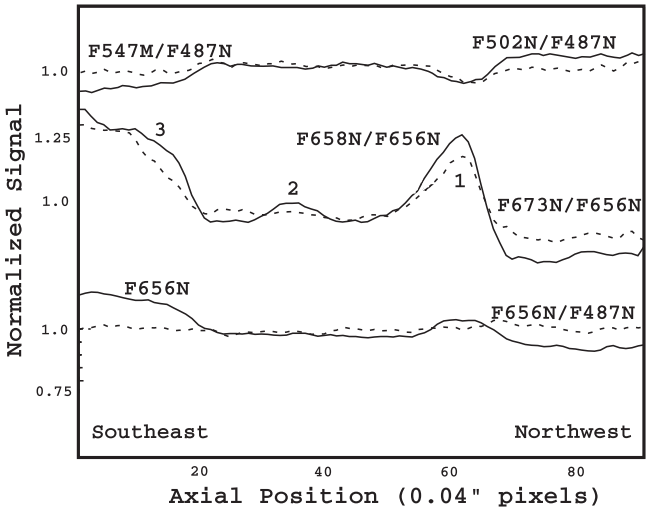

Figure 27. Normalized profiles of 20 pixel (0″.8) width along the short ("axial") line indicated in Figure 25 are presented, with features of particular interest as discussed in Section 4.6.2, numbered. Ratios of images are shown, except for the lowest line, where only the F656N signal is shown.

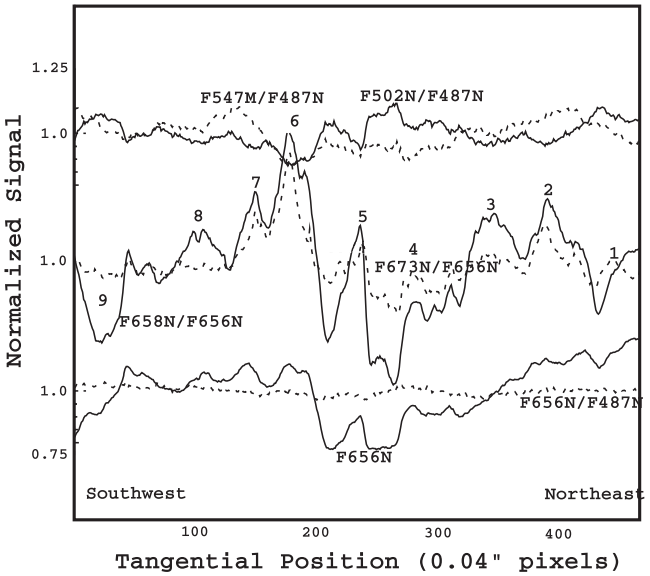

Figure 28. Like Figure 27, except showing results along the long ("orthogonal") line.

Region is dominated by scattered light coming from the dense gas and dust layer lying on the neutral side of the ionization front. In a region where one is looking nearly along an ionization front, one is looking at emission primarily from the ionized gas. This means that a trace across such a tilted ionization front would have dust-scattered light plus atomic continuum (hence a high F547M/F487N ratio) on both sides of the front, but in the immediate direction of the front the continuum would be primarily from ions and the F547M/F487N ratio would drop. This is what is observed.

In Figure 27 there are no big changes in the ratios at feature 2, except for a small rise in F658N/F656N, which means that it is probably a small tilted ionization front. At feature 3 we see the same signatures as at feature 1. However, the characteristics continue off the plot, and examination of Figure 25 shows that

this continues until reaching yet another clearly defined tilted ionization front.

Figure 28 shows a similar profile plot, but in this case giving the profile completely crossing HH 625 perpendicular to the symmetry axis. These profiles are used below to understand features within and near HH 625.

The most striking feature along the symmetry axis within the boundary of HH 525 is a nearly linear feature that begins about 1″ to the southeast of the long sample and extends almost to the southeast end of the axial sample. It is feature 5 in Figure 28. It is clearly not an extinction feature (the F656N/F487N ratio is essentially constant on both profiles). With a dip in F502N/F487N and peaks in F658N/F656N and F673N/F656N, it has the characteristic of a tilted ionization front. However, there is no dip in F547M/F487M, so that it must be very thin. If it is very thin, one does not get an isolated region of solely atomic emission.

Feature 6 has the full set of characteristics of a thicker tilted ionization front viewed nearly edge-on, and with less definition, this pattern is continued to the southwest. This means that there must be a series of ledges.

When reaching feature 9, there is a reversal in the pattern (F502/F487N rises, F658N/F656N drops, and F656N drops). F673N/F656N remains constant at feature 9, unlike the other regions–indicating that all of the peaks in this ratio are due to local features, with the background F673N being nearly constant. The drop in F656N indicates that the local front is tilted away from the photoionizing star (θ^1 Ori C). the strong rise in the low-ionization tracers at feature 6 indicates that this is a tilted front that is narrow as compared with the local Hα-emitting region.

Given that the curving driving jet, as traced by H_2 emission, feeds directly into the symmetry axis where feature 5 lies, it is likely that this causes a deformation in the ionization front. There is no evidence that the jet has emerged, although it must be close to the surface of the Orion-S neutral cloud. Since there are a series of discrete H_2 features along the line of symmetry of HH 625, this information combines to indicate that the molecular outflow from COUP 555 must be intermittent.

5. SMALLER HERBIG–HARO SYSTEMS

The Huygens Region is the host to a large number of HH objects, some identified by jets coming from stars, others from shock forms, and others from two-epoch imaging. In this section we report on a number of previously known HH objects and several new ones discovered on the motion images. We do not report the measurements of the LL 1 object located in the SW corner of the GO 12543 FOV as those results have already been published (Henney et al. 2013).

5.1. HH 510

This young-star jet-driven outflow was first described by Bally et al. (2000) using an *HST*-WFPC2 wide-band filter (F606W) image. The source of the outflow is the edge-on disk proplyd d109.4-326.7 (d119-327, Bally et al. 2000; MLLA 379, Muench et al. 2002; HC 286, Hillenbrand & Carpenter 2000). The Bally et al. (2000) image revealed a monopolar east-pointing microjet beyond which there were two identifiable knots lying on a projection of the jet. Ricci et al. (2008) have published images made with the *HST*-ACS camera using the F435W, F555W, F658N, F775W, and F850LP filters, most

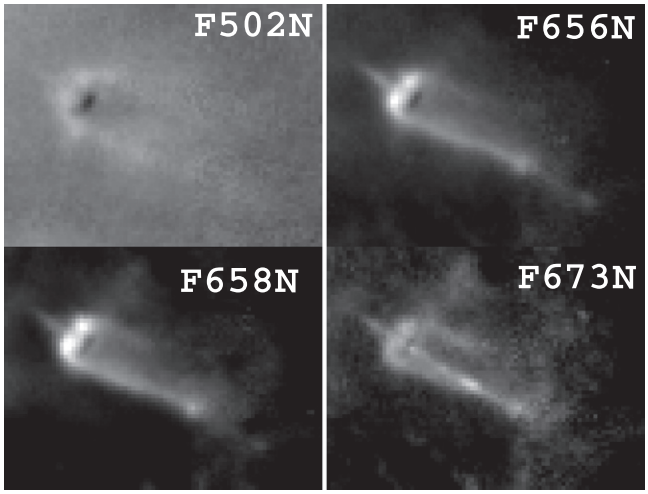

Figure 29. Four 3.″20 × 2.″44 images are presented, each with the vertical axis pointed toward position angle 14°.

of which are most sensitive to continuum radiation, and the narrowband filter F658N of the ACS (which is approximately the same sensitivity at both the Hα 656.3 nm and [N II] 658.3 nm emission lines). The most useful earlier work is that of O'Dell & Henney (2008), who imaged the system in the *HST*-ACS [O III] F502N, F658N, and [N II] F660N filters. These images determined that the jet was extended and knotty and the dominant feature (called s2 by Bally et al. 2000) was rapidly moving, with a dynamical age of about 120 yr.

5.1.1. The Structure of the Proplyd and Its Jets

Our new high-quality WFC3 images have better imaging sampling owing to the 0.″04 pixels and better isolation of emission lines than the earlier studies. Through the availability of AstroDrizzle images of the earlier WFPC2 images, there is the possibility of obtaining improved measurements of tangential motions and changes in the structure. Figure 29 shows a mosaic of four monochromatic images. The F502N, F656N, and F658N images show best the nearly edge-on optically thick circumstellar disk of about 0.″3 width and 0.″1 thickness. Examination of our F547M continuum filter image shows the glow of scattered starlight on the west side of the disk, indicating that the near side of the disk is tilted slightly to the east. In this sense it is like the largest of the pure silhouette proplyds 114-426 (McCaughrean & O'Dell 1996; Shuping et al. 2003) in that the central star is revealed only by scattered light.

We note that the [O III] emission is found on the outer part of the photoionized cap on the side of the disk facing the ionizing star θ^1 Ori C, which lies in the direction 87.°3. The locations of the other emission lines are unresolvable from one another, but they are certainly closer to the disk than the [O III] emission. There is a gap in the ionized cap emission where the east-jet passes through it. The [S II] (F673N) images reveal the west-pointing counter-microjet. Both jets are perpendicular to the plane of the dark disk.

The primary shape of the tail of a photoionized proplyd is determined by photoionization of material on the side of the proplyd not facing the ionizing star, i.e., the shadowed region. Material there has recently been expelled from the photoionized cap and accelerated away from θ^1 Ori C or was expelled from the molecular disk as part of the large-angle flow

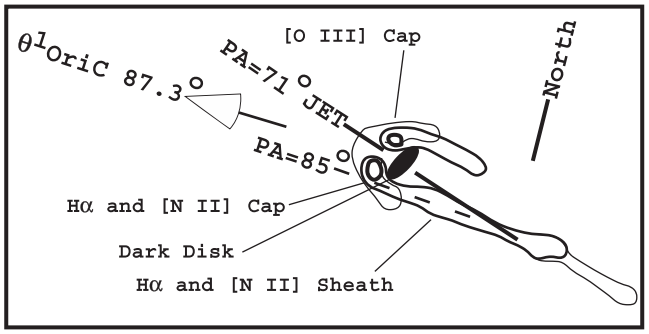

Figure 30. This drawing is based on the images shown in Figure 29 and illustrates the primary features of the proplyd d109.4-326.7 that drives the HH 510 outflows.

from the disk. When the density is high, an ionization front is formed at the outer edges of the shadowed region and the sides of the tails are parallel, as in HH 510. When the density in the shadowed region is low, an ionization front is formed that is in equilibrium with the diffuse Lyman continuum (LyC) produced by the surrounding nebula and the tail shape converges to a point. This shape is often called that of a tadpole.

The boundary of the shadowed zone, which in the case of HH 510 is an ionized sheath, should point back to the ionizing star, which it does, as shown in the drawing that summarizes the primary features of this proplyd (Figure 30). The difference in direction of the ionization boundary (85° ± 5°) and jet (71° ± 2°) means that the east-jet passes through the boundary and one sees an enhancement of the boundary there, and that this boundary curves outward along the track of the jet.

The west microjet is only seen in [S II] emission because it lies within the ionization shadow of the bright cap. The ionization structure of the tail indicates that the tail is ionization bounded. Any illumination within the tail would arise from LyC photons generated as the surrounding photoionized hydrogen recombines. The physics of such objects have been addressed by Cantó et al. (1998). The collisionally excited [S II] doublet emission that we see in the F673N filter requires two major components, singly ionized sulfur and electrons having a few electron volts of energy. Singly ionized sulfur is formed by 10.4 eV and higher-energy photons produced by scattered light of the nebula and its MIF, which freely pass through the tail's ionization boundary. Photons of at least 23.3 eV are necessary to cause ionization to S^{++} and will not pass the layer of neutral helium that must lie outside of the tail's ionization boundary. This means that S^{+} is the preferred state of the jet within the shadowed region. If the jet material has a similar velocity to that of the shocks that it drives (about 100 km s^{-1}), then electrons within the jet have energies of about 52 eV, sufficient to ionize neutral sulfur and to excite the levels producing the observed [S II] doublet.

5.1.2. Shocks Driven by the HH 510 Proplyd

The HH 510 features are shown in Figure 31. The previously known east microjet arising from proplyd d109.4-326.7 is seen in [O III] to be a series of clumps starting at about 2.″4 from the proplyd and ending with a bow shock feature of about 0.″8 width at 6.″6 from the proplyd. The knotty outer portions of the jet are most easily seen in [O III] and Hα, being weak or absent in [N II] and [S II]. The shock is clearly seen in all filters except [S II], and its faint appearance in the F673N may be due to the larger width of that filter, which admits much more continuum than the other emission-line filters.

The newly discovered west microjet is not traced beyond where the [S II] jet intersects and distorts the west ionization boundary of the tail. Only a few hints of structure are present, once in [O III] and once in [N II]. These features are described below in the discussion of the motions.

We present in Figure 32 the results of two-epoch ratio images in F502N and F658N. We have drawn in a bright ellipse over the position of the dark disk of d109.4-326.7. This overlying feature is twice the dimension of the true disk. Arrows represent the velocities measured either by the ZSQ method or from direct measurement of the features. One sees clearly the effects of the collimated jet interacting with ambient material along the projection of both the east-jet and the west-jet. The direction of the jet's flow (71°) is shown as a thin white line in Figure 32. In the upper (F502N) panel we have added the positions of 10 knots, and in the lower (F658N) image we have added two features, one of which (sw2) is common to both filters (O'Dell & Henney 2008). The tangential velocities are presented in Table 4. Using the tangential angular velocity (μ) and the distance of the feature from the proplyd (θ), we have derived a characteristic age (T) from the relation $t = \theta/\mu$. It appears that increases in the jet outflows have been occurring at intervals of about 150 yr. Such episodic outflows are not unprecedented (Reiperth et al. 1986) and have been recently discussed by Raga & Noriega-Crespo (2013) in the context of HH 34.

We do not have V_T and V_r values in the same ions for either of the series of shocks associated with HH 510. However, for [O III] the V_T for the ne6 feature is 96 km s^{-1} and the average V_r in [N II] for the other ne shocks is -6 km s^{-1}. Within the assumption that these velocities are related, the shock ne is moving at $V_{OMC} = 101$ km s^{-1} with $\theta = 18°$.

It is likely that the feature sw1, which is seen only in [N II], is unrelated to the shocks driven by d109.4-326.7's jet. This is because the feature does not fall along the west jet's axis, it is clearly low ionization (whereas the other features are high ionization), and the tangential velocity is much lower than the other HH 510 features.

5.1.3. The 3D Location of HH 510

The visibility of HH 510 is made difficult because of the presence of other structures. However, we can use them to determine their relative positions along a line of sight into this part of the Huygens Region. There is no indication of interaction of the east-jet and the associated shocks with HH 625. HH 510 must lie in the foreground relative to that object.

About 3″ west of d109.4-326.7 the jet crosses a long feature shown in each of the panels of Figure 33 and most visible in the F502N panel (upper) of Figure 32, which shows its motion. The ratio images show that the long feature is an ionization boundary, with the ionization preceding from [O III] to [N II] to [S II] going from east to west.

This boundary is the northwest portion of a large area of high ionization northwest of the Trapezium grouping of massive young stars. It resembles several large parabolas pointing northwest with centers displaced about 30″ and extending back to the Orion-S region. The largest and easternmost parabola points toward the HH 202 shock complex, and the shortest and westernmost is about the same orientation as HH 625. They both are moving to the northwest (O'Dell & Henney 2008), and

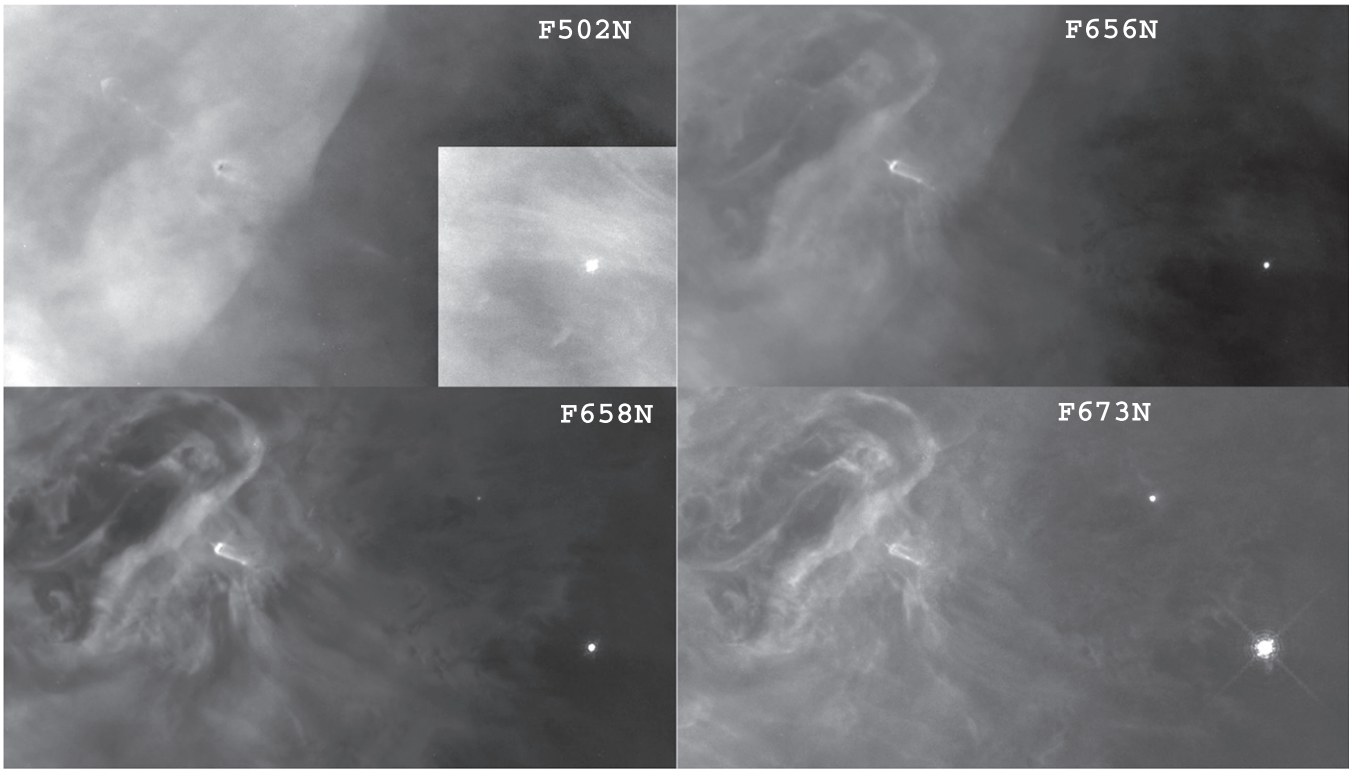

Figure 31. Four $31\farcs1 \times 17\farcs6$ monochromatic emission-line images of the vicinity of proplyd d109.4-326.7. The proplyd is at the left center in each, and the large feature to the left in each is the optical feature HH 625 discussed in Section 4.6. The vertical axis is pointed toward position angle 14°. The $11\farcs0$ square inset in the lower right of the F502N image is simply a rescaling of the display range in this area. It is contiguous with the remainder of that image.

their axes are separated by about 30″. These large structures were discussed in a study of the 3D structure of the inner Orion Nebula by O'Dell et al. (2009). It is likely that the easternmost parabola is associated with the HH 202 shocks and the westernmost parabola is associated with HH 625.

The west-jet from d109.4-326.7 passes through a break in this ionization front. This argues that the break is caused by the jet and that d109.4-326.7 lies within the high-ionization central cavity of the nebula. A caveat to drawing that conclusion is that we see a half shock in all the emission-line filters. When the image of this half shock is flipped on itself, the axis of this large shock is the same as the d109.4-326.7 jet and shocks. The mirror image of the half shock indicates that the full width of the parabola is about the same size as the gap in the ionization boundary feature, suggesting that this large shock is the cause of the interruption, rather than the west-jet. Of course, there may be a physical relation between the west-jet and this half-shock feature.

It is of interest that near the star 102.7-316.4 there is an incomplete circle of high ionization and immediately outside that circle there are multiple irregular features seen in [N II] and [S II]. Certainly this low-mass and low-temperature star is not the source of ionization that produces the [O III] emission. However, its large-angle stellar wind could have excavated a local region that has allowed photoionizing radiation to enter.

The high ionization seen in both the east and west outflows from d109.4-326.7 may be due to collisional effects, rather than photoionization. The new shock is moving at about 100 km s^{-1}, which corresponds to 52 eV of energy, plenty to doubly ionize oxygen (removing the second electron takes 35.1 eV photons.

5.2. HH 518

Various features have been assigned to HH 518 since its first designation in Bally et al. (2000), where it had only one feature, a single shock at 162-342. O'Dell & Henney (2008) argued that it was composed of the shocks 163-342, 165-334, 172-327, and 177-322. Our superior determination of the motions (seen only in F502N) shows that there are actually two separable flows. We have designated them as HH 518a (162-342, 165-335, 164-333, and 165-333) and HH 518b (164-343 and 167-337), as shown in Figure 19.

Farther west along a slightly CW curving of the axes of HH 518a and HH 518b we see additional large moving shocks that are probably part of these flows. In Figure 22 we see shocks A (170-325) and B (172-327) WSW of θ^1 Ori C and shocks C (177-320), D (178-318), E (178-321), and F (180-325) WSW of θ^1 Ori D. Inclusion of these shocks makes the HH 518 flows among the largest in the Huygens Region.

The average axis of these two flows passes through the bright variable V2279 Ori, which is probably the source of the optically invisible jet driving both HH 518a and HH 518b. There are no shocks identifiable with material streaming in the opposite direction from V2279 Ori.

Doi et al.'s (2004) velocity mapping showed that the shocks identified with HH 518 are redshifted. This is confirmed in our analysis. These flows are among the few in the Huygens Region that show positive values of V_r, indicating motion toward the OMC. For shock 164-343 $V_r = +95$ km s^{-1} and $V_T = 13$ km s^{-1}. These yield $V_{OMC} = 70$ km s^{-1} and $\theta = -79°$. There are two high positive velocity shocks (+102 km s^{-1} and +122 km s^{-1}) to the EWE from 164-343 that are probably associated with the material driving HH 518a and HH 518b.

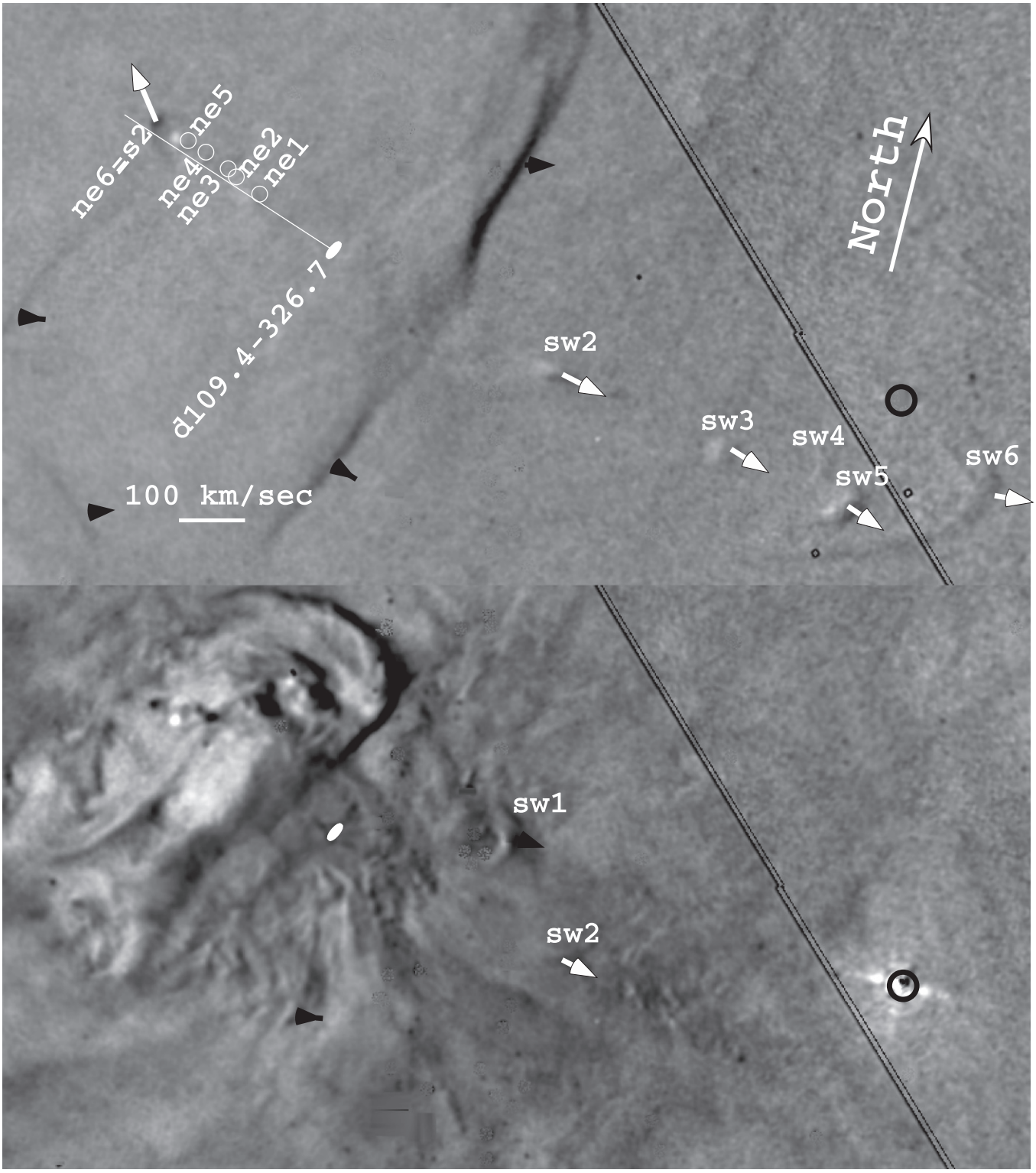

Figure 32. The same field of view as in Figure 31 is shown as the ratio of first-epoch (GO 5469) over second-epoch (GO 12543) images in the two filters capturing the high-ionization ([O III] with F502N) and low-ionization ([N II] with F658N) emission from the nebula. The added details are explained in Section 5.1.2. The thin white line indicates the direction (71°) of the microjet extending east from d109.4-326.7. The star 102.7-316.4 has been indicated by a thick white circle in the lower right.

5.3. HH 530 Redefined

The object HH 530 has been mentioned in multiple studies since its discovery by Bally et al. (2000). As shown in Figure 34, the region is complex, and in fact it must be a composite of unrelated features, as first suggested by O'Dell & Doi (2003a). The dominant feature is a large, low ionization bow shock facing west with numerous nearby small moving features. We designate the large low-ionization shock as the Large Shock in Figure 34, and its axis of symmetry is about 281°. The conditions in this region are illuminated and somewhat confounded by recent CO studies with ALMA (Bally et al. 2015).

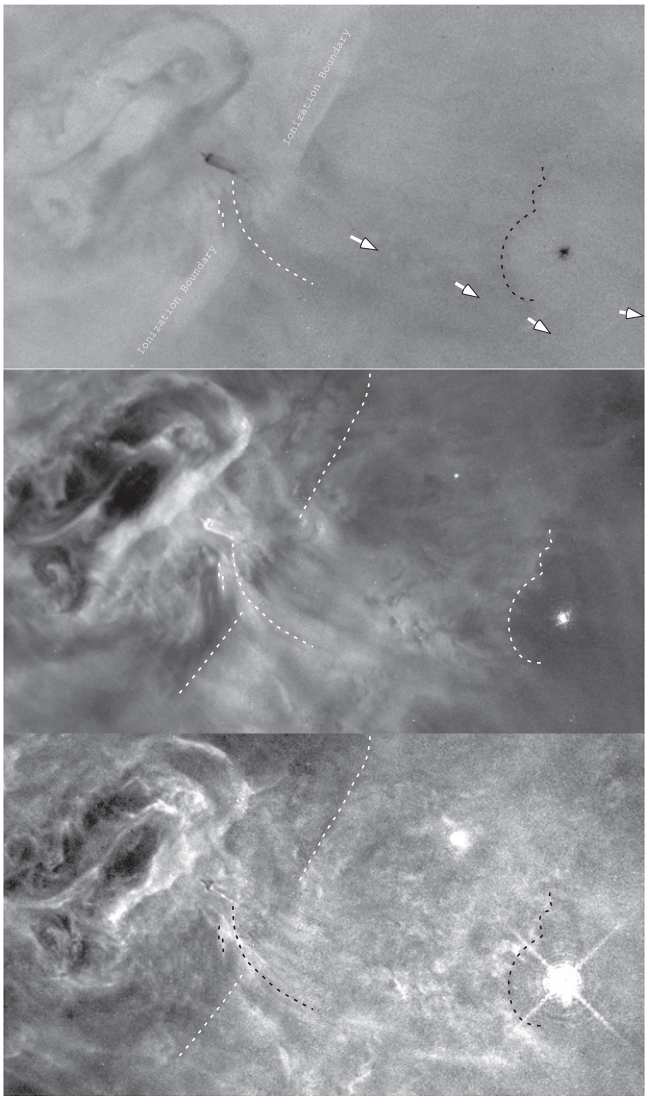

Figure 33. The same field of view as in Figure 31 is shown as the ratio of the extinction-insensitive ratios of F502N/F487N (upper), F658N/F656N (middle), and F673N/F656N (lower). The rapidly moving [O III] features sw2, sw3, sw4, and sw5 are shown as arrows. The features marked "Ionization Boundary" in the upper panel are shown as a dashed white line in the lower two panels. An apparent ionization boundary east of star 102.7-316.4 is outlined as a dashed white line in the upper two panels and a dashed black line in the lowest panel. An open partial shock lying to the west of the proplyd d109.4-326.7 is shown as dashed lines (white in the upper two panels, black in the lowest panel).

Table 4
Tangential Motions of Objects near HH 510

Object Name	μ (″/yr)	Tangential Velocity (km s^{-1})	θ (″)	Age (yr)
ne2	0.047	97	6.56	140
sw1[a]	0.013	26	5.54	440
sw2	0.032	67	7.87	250
sw3	0.033	68	13.44	410
sw5	0.031	65	17.38	560
sw6	0.029	59	21.2	750

Note.
[a] Object sw1 is unlikely to be associated with HH 510 in spite of its proximity to proplyd 109.8-325.3.

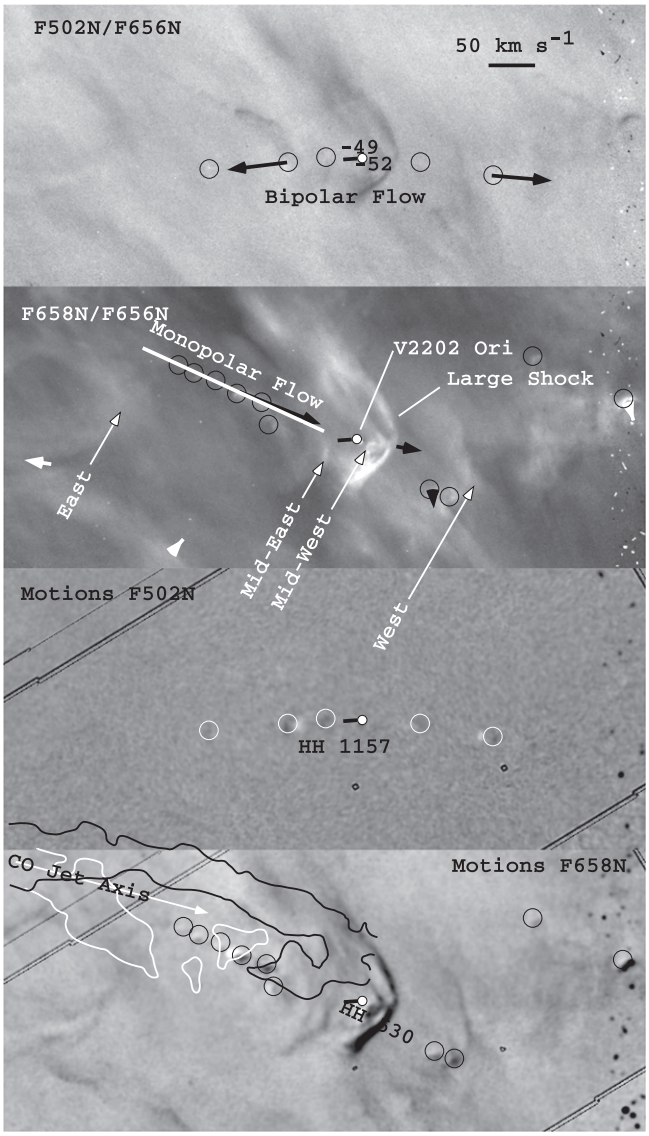

Figure 34. These four identical FOV 27.″5 × 12.″1 images centered on HH 530 show both ratio images (upper two panels) and motions (lowest two panels). The FOV is shown in Figure 2. The open circles indicate the position of components of the two flow systems (HH 530 and HH 1157), some of which could not be measured quantitatively. The only star in this FOV is V2202 Ori, the apparent source of the HH 1157 bipolar flow. The numbers indicate the [O III] V_r values. These lie at the extreme west boundary of the spectral Atlas. The irregular lines in the lowest panel represent the outer contours of blueshifted (white, 20.1–24.0 km s^{-1}) and redshifted (black, 28.6–32.4 km s^{-1}) CO emission reported by Bally et al. (2014). The white arrow designates the direction (PA = 269°) of the highest-intensity portions of this molecular jet.

5.3.1. HH 1157

In the F502N ratio and motion images (Figure 34) we see that there are a series of high-ionization shocks extending from both sides of V2202 Ori. We designate these as the bipolar flow feature. This flow is slightly curved and points toward 108° to the east and 276° to the west. A close examination of our images of V2202 Ori in the F502N and F656N filters reveals an unresolved width microjet about 0.″2 long pointed to about 108° (with an uncertainty of about ±10°). Within the uncertainty of this angle, it must be the driving source for the

east-moving series of shocks. We must be seeing shocks formed by an episodic bipolar flow that is curved owing to the southward-moving ambient high-ionization gas. This bipolar flow is designated as HH 1157. The spectral Atlas coverage ends a few arcseconds west of V2202 Ori, but it does show high radial velocities (−49 and −52 km s^{-1}) in [O III] coincident with that star, and they probably arise from its microjet.

The similarity of the Large Shock's orientation of about 281° and the direction of the western HH 1157 flow (276°) is likely to be coincidental. There is a gap in the well-defined Large Shock where the west-moving high-ionization flow from V2202 crosses it in the plane of the sky. This argues that this aligned high-ionization HH 1157 flow is penetrating and disrupting the large low-ionization Large Shock. They are probably unrelated, and the Large Shock is driven by another collimated outflow.

5.3.2. HH 530

In the F658N ratio and motion images we see a series of low-ionization shocks moving toward 259°. We designate these as the Monopolar Flow feature. Although it nearly aligns with V2202 Ori, it is moving toward that star. These westward-moving shocks and V2202 must be unrelated, and the origin of the Monopolar Flow feature must lie to the east. If one includes the two low-ionization shocks to the west of the Large Shock as part of the Monopolar Flow, it is seen that clearly the flow passes south of V2202.

Within the arc of the Large Shock is a low-ionization-moving feature designated as Mid-west. This feature is near where one sees similar features in HH 269-west and HH 625, but not quite at the same position as this shock lies below the symmetry axis of the Large Shock. It is close to the axis of the Monopolar Flow, but slightly below. The small low-ionization-moving knot designated as Mid-east falls below the projection of the Monopolar Flow but otherwise has the same characteristics of the Monopolar Flow. There are two low-ionization knots lying just below a projection of the Monopolar Flow, and they lie immediately to the east of the larger west shock. It appears that the Monopolar Flow curves slightly south and may produce the larger, low-ionization west shock.

With the identification of the bipolar flow from V2202 as HH 1157, HH 530 can be said to now be composed of the Monopolar Flow, the Large Shock, the shock we label as west, and two small shocks (Mid-east and Mid-west). However, this grouping into one flow (HH 530) is probably too simplistic.

5.3.2.1. HH 530 Is Complex

In a recent study of the nearby silhouette proplyd 114-426, Bally et al. (2015) discovered CO emission velocity shifted with respect to the OMC. The west end of these features is shown in Figure 34 and the east in Figure 42. The linear blueshifted CO axis is oriented PA = 269°, with a spur on the east end (Section 5.13) and another pointing SE on the west end. The blueshifted axis orientation is 10° larger than the Monopolar Flow axis, but they may be linked if the CO molecular flow is redirected in the plane of the sky as it passes through the MIF.

Because of their proximity, it is tempting to associate the redshifted and blueshifted CO flows. However, a link is difficult to understand unless a bipolar stellar outflow has suddenly reversed direction or the elongated redshifted component is only a portion of an expanding envelope surrounding the blueshifted linear flow, which seems unlikely.

The redshifted flow has the fish-hook feature of an incomplete bow shock, with its apex within the optical Large Shock feature. However, the apex of the CO feature lies NE of the apex of the Large Shock. The average of its flow is 272°, different from the 281° symmetry axis of the Large Shock. A link of the Large Shock to either the redshifted or blueshifted components could be established by determination of the Large Shock's radial velocity. Unfortunately, the database of velocities that we used ends just east of the Large Shock.

5.3.2.2. The Origin of the HH 530 Complex

The reciprocal of the several directions associated with the HH 530 features all point in the direction of a concentration of imbedded young stars and known molecular outflows called the Ori-S6 region, whose most prominent source is EC 14 (Schmid-Burgk et al. 1990; Zapata et al. 2013). EC 14 lies 49″ at 82° from the apex of the Large Shock. 82° is similar to the reciprocal of the HH 530 features (Large Shock symmetry axis, 101°; Monopolar Flow, 79°; CO blueshifted jet, 89°). If one begins the search for a source or sources at the east end of the CO jet, there are no candidate stars until reaching the region of Ori-S6, and then there are many (including COUP 496, 132-413, EC 12, H20097, EC 113, EC 14, COUP 582, COUP 615). EC 14 is highly unlikely to be the source because it begins its outflow at 225° before being deflected toward 209°.

5.4. HH 626

The central star of this outflow is V1328 Ori (142.8-424.6). It was first detected outside the optical region in the radio study of Felli et al. (1993) and has now been observed through the infrared and into X-ray wavelengths. O'Dell & Wong (1996) noted it as a round proplyd with a tail, reporting that its size was 0.″6 × 0.″73. Examination of our new images shows that the star is embedded in a concentrated core of emission and that after deconvolution is 2.8 ± 0.3 WFC3 pixels, or 0.″1 ± 0.″01 FWHM. There is a low-ionization microjet traceable to 0.″88 from the star in the direction 224°. This is probably what led O'Dell & Wong (1996) to conclude that the proplyd was elongated. There is a much fainter linear feature at 214° that extends to 3.″0 from the star and is labeled the extended jet. V1328 Ori lies at 208° with respect to θ^1 Ori C. This means that the microjet and the linear feature are not inline or in the direction expected for the tail of a proplyd and the features are part of a collimated outflow and not simply the tail formed by gas being accelerated away from V1328.

HH 626 was initially reported by O'Dell & Doi (2003a) as an incomplete double ellipse of high ionization, being visible only in F502N and F656N images. Along a line with 149° there are two shocks (as shown in Figure 35. The southeast component is 5.″0 from the central star, and a blunter shock is in the northwest direction at 4.″8. F658N emission is seen clearly only in the northwest blunt shock. None of these features align with the microjet and its possible extension.

There are a number of additional shocks probably belonging to HH 626. At 354° and 6.″0 there is a bright high-ionization shock and there are several fainter shocks to the west through

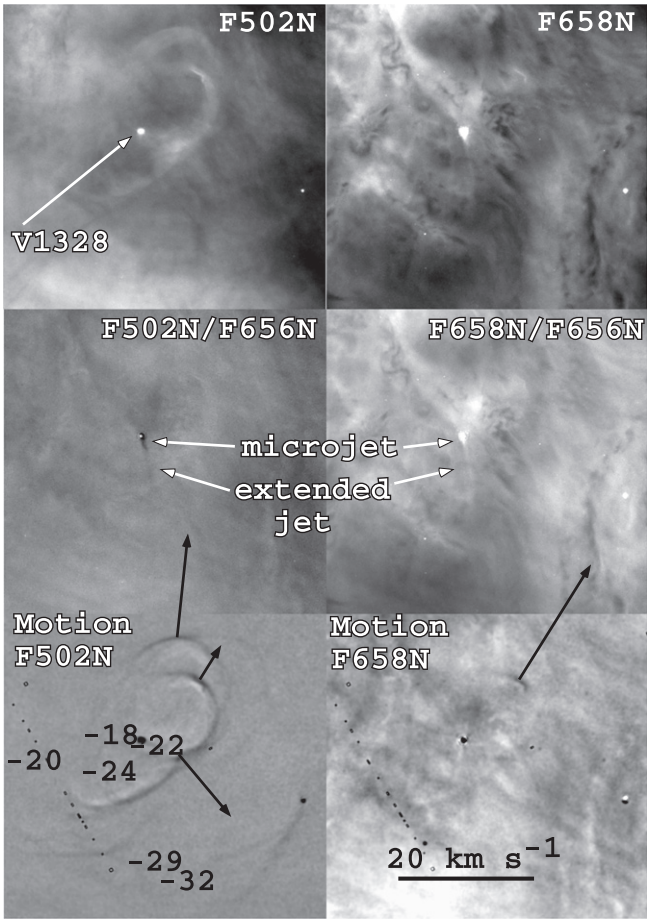

Figure 35. This mosaic is composed of $18\farcs9 \times 17\farcs9$ images of the components of HH 626. This FOV is labeled HH 626 in Figure 2. The central star is V1328. The microjet, the extended jet, and the measured velocity vectors are shown. V_r values in [O III] are inserted.

southeast. The dynamical age of the three measured components (from nearest to farthest) is 350, 800, and 1700 yr.

As noted by O'Dell & Doi (2003a), HH 626 appears to be shocks associated with either a large-angle wind from the proplyd or photoevaporative flow from a disk of gas and dust close to the central star and unresolved in our images. The multiplicity of the shocks indicates that they might be formed by different flows in nearly orthogonal directions. The star is probably located within the high-ionization, low-density gas that exists between the MIF and the foreground Veil. The lower brightness of the features in the northeast probably indicates that the slow wind from the star is moving into lower-density ambient gas in that direction.

Only in the case of the feature 2″ west of V1328 Ori are there both radial and tangential velocities. Using $V_T = 12\,km\,s^{-1}$ and $V_r = -22\,km\,s^{-1}$ gives $V_{OMC} = 49\,km\,s^{-1}$ and $\theta = 66°$.

5.5. HH 998

O'Dell & Henney (2008) designated the shock 158-355 as HH 998. This well-defined shock is more visible in F502N but is clear in both the F502N and F658N motion images (Figures 19 and 20). Its symmetry axis is toward 244° and moves along that axis. There is a fainter shock of the same form and direction of motion about 0.″6 outside of it. Much farther out (8.″0) there is the large and less well defined shock (153-359) that aligns suggestively near the axis of the HH 998 shock and may be the result of an earlier outflow from a common source.

O'Dell & Henney (2008) discovered a microjet extending 0.″4 from AC Ori at 47° and could see no shocks identifiable with it in that direction. The microjet is shown as a short dark line in Figures 19 and 20.

HH 998 lies at 4.″1 at 230° from AC Ori, and O'Dell & Henney (2008) argued that it was produced by a counterjet (227°) from that star. However, those directions do not agree with the symmetry axis of HH 998 (244°). This calls into question the conclusion that AC Ori is the source of HH 998. There are two other possible sources, COUP 769 and a currently undetected source (Blank-east).

The highly obscured star COUP 769 is the first alternative source. The HH 998 shock lies 3.″9 at 254° from it. This means that neither AC Ori nor COUP 769 lies exactly along the symmetry line of the HH 998 shock, with the difference being +14° for AC Ori and −10° for COUP 769. No clear association is possible, with the known microjet in AC Ori favoring that star while the closer PA alignment favors COUP 769.

If the driving source of the HH 998 shock is AC Ori, then the shock arose 330 yr ago. If the driving source is COUP 769, then the shock arose 355 yr ago. However, it is most likely that the source lies in the Blank-east region. In this case the age of the HH 998 shock would be even shorter.

We have both radial and tangential velocities for only one of these features. The derived 3D motion for 155-354 ($V_r = -53\,km\,s^{-1}$, $V_T = 4.6\,km\,s^{-1}$) is $V_{OMC} = 79\,km\,s^{-1}$, $\theta = 87°$.

5.6. HH 1127

The isolated flows near the Dark Arc first seen by O'Dell & Doi (2003a) are now shown clearly in our motion images and designated as HH 1127. The motion and emission-line images of this object are shown in Figures 36 and 37.

The HH 1127 system is defined by two parabolic shocks of increasing size aligned and moving toward 255° and three small shocks at 252°. As indicated previously (O'Dell & Doi 2003a), they head away from star MAX 46, which is seen only in infrared wavelengths. However, their alignment is equally good with the more distant star COUP 602, which is seen in X-rays, optical, and the infrared. We can rule out an association with the nearest star (V1398) because the velocity vectors and the alignments pass south of that star. There are no nearby candidate stars beyond COUP 602. The closer shock has a kinematic age of 400 yr and the farther shock 700 yr if the source is MAX 46, and 540 and 640 yr, respectively, if the source is actually COUP 602.

Only the westernmost shock of HH 1127 may have an associated radial velocity (the [O III] $V_r = -36\,km\,s^{-1}$, [O III] $V_T = 38\,km\,s^{-1}$). The derived spatial motion is $V_{OMC} = 73\,km\,s^{-1}$ and $\theta = 58°$. We note that there are similar unrelated [O III] radial velocity features of about the same value in the vicinity of the HH 1127 shock. It may be that we cannot actually derive a V_{OMC} for HH 1127.

There are no shocks that clearly lie westward along the axis of the HH 1127 flow. It is not clear whether the high-ionization knot (126-346) shown at the bottom right of the F502N panel (upper) of Figure 36 is part of the HH 1127 system. Its V_T ($39\,km\,s^{-1}$) is comparable to that of the two parabolic

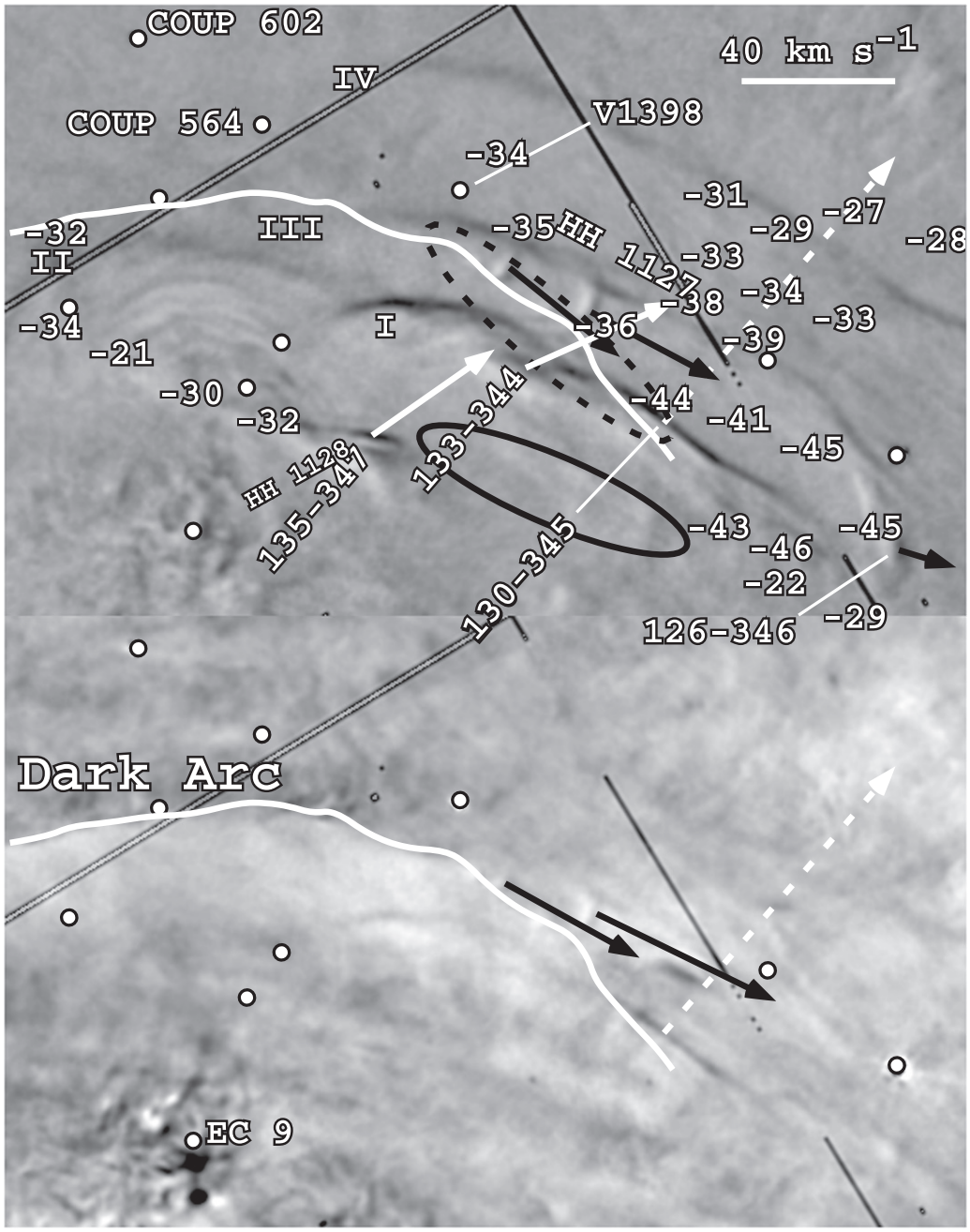

Figure 36. This pair of $25\farcs0 \times 15\farcs9$ motion images centered on the northwest corner of Figure 10 shows the tangential velocities measured in this study for the parabolic arcs and the knot within HH 1127 (black arrows), the average (as a dashed white line) of the motions in Hα and [N II] measured by O'Dell & Doi (2003a) for the feature they call 130-345, and the newly measured motions for features 133-344 and 135-347, which are not part of HH 1127. The velocity vector for 126-346 in the F502N (upper) panel is at 40% the scale of the other vectors. The irregular curved white line delineates the sharp north boundary of the Dark Arc feature. The ellipses and Roman numerals designate objects discussed in Sections 5.6 and 5.7. The negative numbers indicate the high-velocity [O III] features. The white lines without arrowheads indicate the names of features in crowded fields.

shocks (average 37 km s^{-1}). Its direction of motion (267°) is slightly CCW from the direction of motion of the HH 1127 shocks (255°), and its position direction is slightly CW (249°) with respect to the HH 1127 shocks. It may be part of the HH 1127 system, but this is unlikely.

There is a narrow, strong, irregular, nearly linear [O III] feature within the dashed ellipse in the upper right panel of Figure 37. The orientation is toward 240°, and it extends for $7\farcs7$. The position and orientation indicate that it is not a jet associated with the HH 1127 flow. Its NE end is coincident with a linear F658N feature, and no F658N feature is seen on the SW end. In F502N it lies along the edge of the Dark Arc feature. If it is an edge-on ionization front, it is one of the most narrow that has been found.

The many [O III] radial velocity features in the west side of Figure 37 show no obvious correlation with features seen in the motion images (Figure 36), with the exception of one feature possibly associated with the westernmost HH 1127 shock. One group with an average of $V_r = -33 \pm 4$ km s^{-1} lies in the NNW area, another five features with an average of $V_r = -44 \pm 2$ km s^{-1} lie in the region between HH 1127 and shock 126-346, and two other velocity features (average $V_r = 26$ km s^{-1})

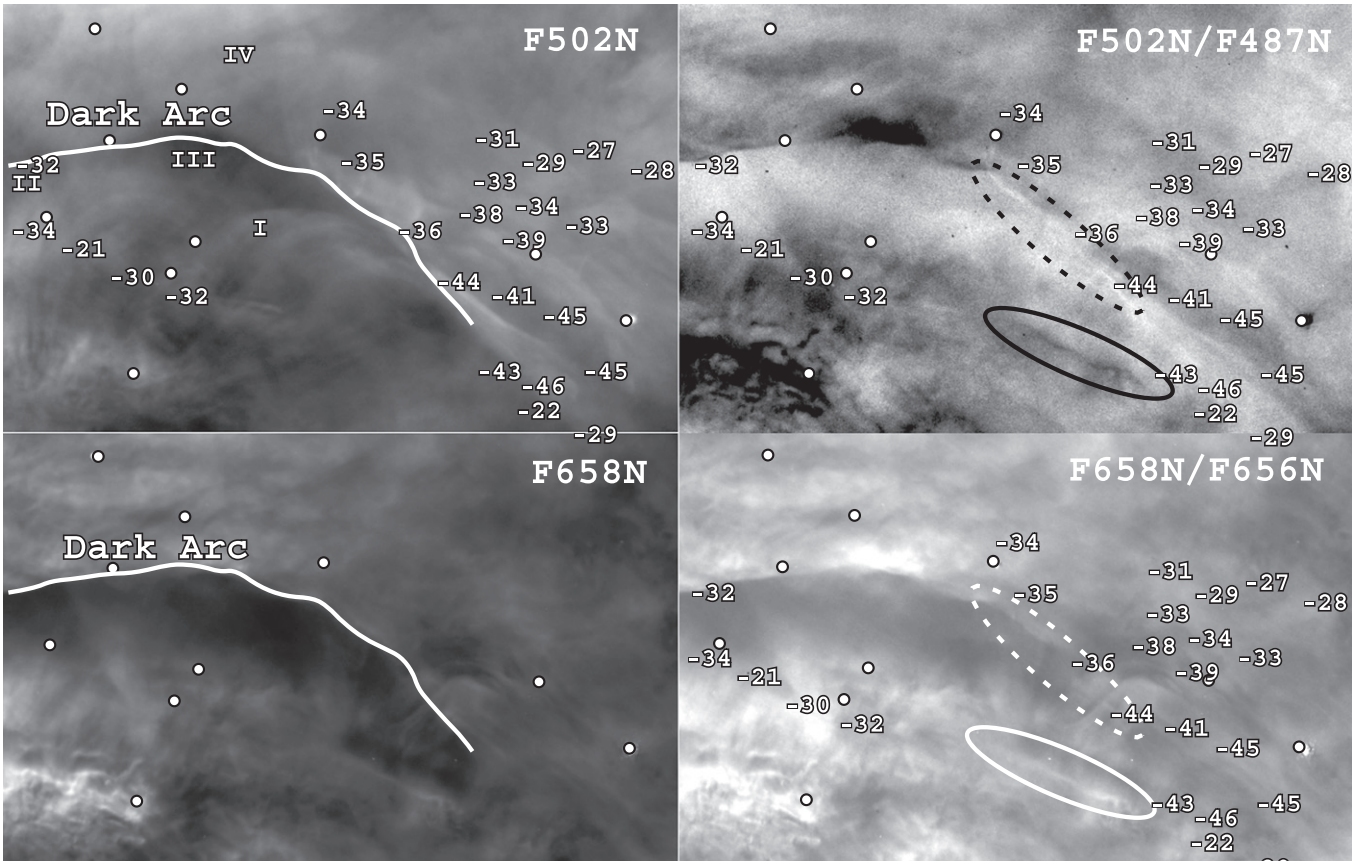

Figure 37. The same FOV as Figure 36 is shown in single-filter and ratio images. The boundary of the Dark Arc is highlighted by a wavy line. The numbers in the panels indicate high-velocity [O III] features.

are found south of shock 126-346. Obviously, some types of medium-scale outflows are occurring in this area, but it is not clear what they are.

5.7. Motions within and near the Dark Arc

There are important structures within and near the Dark Arc. One series of shocks has been reported before, and the remainder were discovered in our new images.

We see in the F502N motion image (Figure 36, upper panel) and the F502N image (Figure 37, upper left panel) that there is a series of three large high-ionization incomplete parabolic shocks directed approximately toward 68°. The westernmost shock is the most visible of the three in Figure 36 and is labeled I. The NW boundary of the westernmost shock is about parallel to the HH 1127 flow (there is probably no association) and about 1.″6 south. These shocks were initially reported by O'Dell & Doi (2003a) on the images then available, where they reported the orientation as 85° and they measured one boundary, calling it 130-345.

We also see in the F502N motion image (Figure 36, upper panel) and the F502N image (Figure 37, upper left panel) three other even larger high-ionization shock features, labeled in Figure 36 as II, III, and IV. The NW boundary of III passes almost parallel to and about 0.″8 north of HH 1127. These objects appear as northern portions of very large incomplete parabolic shocks that are moving toward about the same direction of I (68°). There is evidence in both [O III] and [N II] for an even fainter large partial shock with an apex about 3″ west of feature IV. There is a linear sequence including velocities of −32, −30, −21, −34,and −32 km s^{-1}, as shown in the figures. Another feature at −31 km s^{-1} lies on an extension of this series. Their PA is about 74°, close to the approximate 68° of the large partial shocks. Although there may be a relation of this sequence to the large shocks, their positions are too far east to be the source of even the easternmost shock II. There are no candidate stellar sources for this series of high radial velocity features. The size and incompleteness of shocks I through IV render it imprudent to comment on their sources, but these must lie at a considerable distance to the WSW. Shock II can also be designated as 141-345 and is discussed further in Section 5.13. There is a strong resemblance to the wide shocks lying along the axis of the HH 202 flow (Sections 4.2 and 5.1.3).

There is a narrow [N II] strong linear feature within the ellipse in the lower right panel of Figure 37 that resembles a jet. This feature is undetectable in [O III] and appears dark in an F502N/F487N image. This indicates that it is either a low-ionization jet or a local ionization front seen almost edge-on. If it is a jet, the orientation of 81° is 13° less than the orientation of shock II, which is the best candidate for an association with a visible shock. We note that this linear feature points close to the series of high V_r [O III] features discussed in the preceding paragraph. The difference in PA of the linear feature (81°) and the series of [O III] high-velocity features (74°) argues against an association. The linear feature is probably an edge-on ionization front.

There are two features moving along the same direction lying to the NW (312°) from star EC 9 (137.2-350.6). Shock 135-347 lies at 5.″2 from the star and shock 133-344 at 9.″5. The orientation, motion, and proximity argue that these are shocks driven by an optically invisible jet arising from star EC 9. This object is only seen at millimeter wavelengths and is object 24 in the catalog of Eisner & Carpenter (2006). This source and pair of shocks is designated as HH 2034AA.

Along the same line passing through shocks 133-344, 135-347, and star EC 9 is a series of shocks to the south near the star COUP 607, as seen in Figure 19. The motions of these shocks indicate that there is no association with the EC 9 driven shocks. The former are discussed in Section 5.8.

5.8. Complex Shocks Forming HH 1153

There are a group of high-ionization shocks near the star COUP 607. On a motion image such as Figure 19 the movement appears to be to the south. However, this is a result of the complexity of the field, which has both bright and dark features. When the individual features are measured, a movement toward 19° is apparent, a conclusion supported by the symmetry axes of the shocks. We designate this group of shocks as HH 1153.

There are no nearby stars toward the reciprocal heading, and the Ori-S6 region (Schmid-Burgk et al. 1990; Zapata et al. 2013) is the first group of sources encountered. The source EC 14 that is identified by Zapata et al. (2013) as the source of a deflected SO outflow lies at 196° with a distance of 12.″9. The direction of EC 14 is close to the reciprocal of the motions of the COUP 607 shocks, but it is impossible to link the shocks to the molecular outflows since the initial flow is toward 245° and after deflection it is 238°.

5.9. HH 1154

O'Dell & Henney (2008) noted an unusual feature, best seen in F658N, and designated it as 137-317. They interpreted it as a bright object moving at 155 km s^{-1} toward 113°. This may not be the case if the apparent motion was caused by the changing structure of the feature. The object is very low contrast with the background, even in its stronger F658N line. It appears as a crescent, oriented to the NE, and is absent in F502N. The earlier epoch images of this region (GO 5469 and GO10921) are of course lower resolution than the GO 12543 images, but the change of appearance is much more than can be attributed to improved resolution. If the bright feature in the lowest panel is interpreted as a change of position, the motion would be 146 km s^{-1} toward 120°, similar to the results of O'Dell & Henney (2008). The tip can be designated as 136.5-317.5. The presence of an isolated high radial velocity feature in [N II] at −110 km s^{-1} argues that the correct interpretation is that it is a moving feature (the −110 km s^{-1} feature is only 0.0028 the strength of the emission from the MIF, but it is well resolved). We designate the apparent high-velocity shock as HH 1154.

There is a single nearby star. The proplyd 139.2-320.3 (COUP 593) was discovered by O'Dell & Wen (1994) and was designated there as 139-320. The proplyd has been detected in X-rays, in optical wavelengths, and in infrared wavelengths. In our images we see an unresolved dark disk in F502N that is surrounded by a ring of [O III] emission that is 0.″3 in diameter.

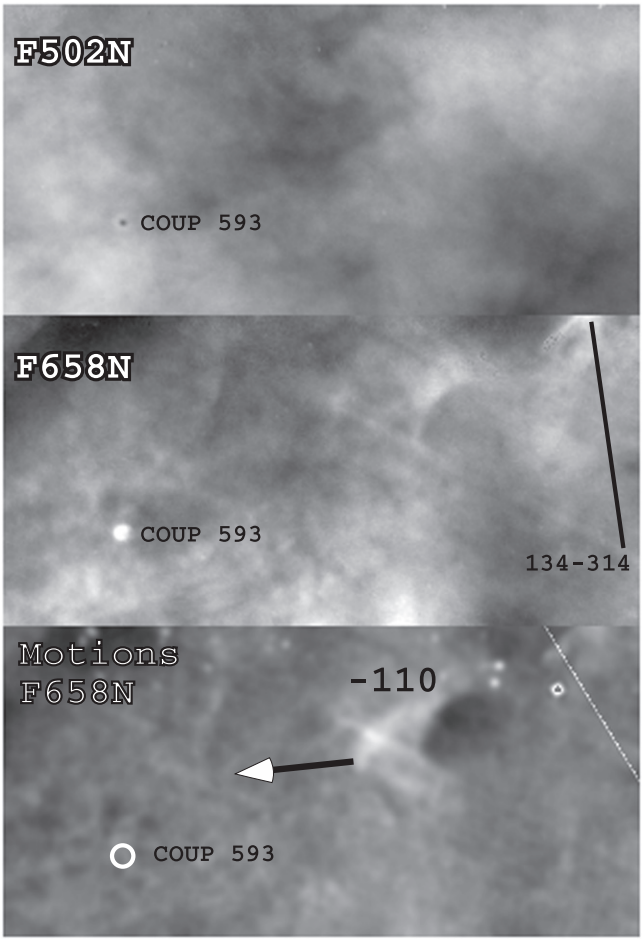

Figure 38. This set of 12.″0 × 5.″8 FOV images shows the region around HH 1154. The upper panel shows the GO 12543 F502N images and the middle panel the GO 12543 F658N images. The lowest panel shows the motion image displayed so that the positions of objects on the second-epoch images are brighter. The FOV is designated as HH 1154 in Figure 2. The only star in this region is shown. The stationary shock feature (134-314) is pointed out in the middle panel with a black line. In the motion image the only high radial velocity feature ([N II]) in this region is shown. The cluster of star-like features in the upper right of the lower panel are from cosmic-ray events not edited out of the second-epoch F658N images.

In F658N it is a partially resolved star-like source of FWHM = 0.″2.

If the derived V_T (146 km s^{-1}) and V_r (−110 km s^{-1}) arise from the same feature, then V_{OMC} = 200 km s^{-1} and θ = 43°. HH 1154 is left here as a curiosity, one that begs for resolution of its motions through additional radial velocity spectra and WFC3 images in F658N.

We see a curious linear feature that tangentially grazes the low dark feature (seen best in Figure 38, lower panel). The PA is 257°, and it starts before the dark feature and extends after it. This eliminates it as an ionization shadow cast by HH 1154. A projection toward 77° points toward θ^1 Ori B, which is much cooler and much lower in LyC luminosity than θ^1 Ori C.

5.10. Outflows in the Region Immediately SW of the Trapezium

The region immediately SW of the Trapezium contains several previously unrecognized high-velocity flows. We characterize four and when possible identify the best candidates for their sources.

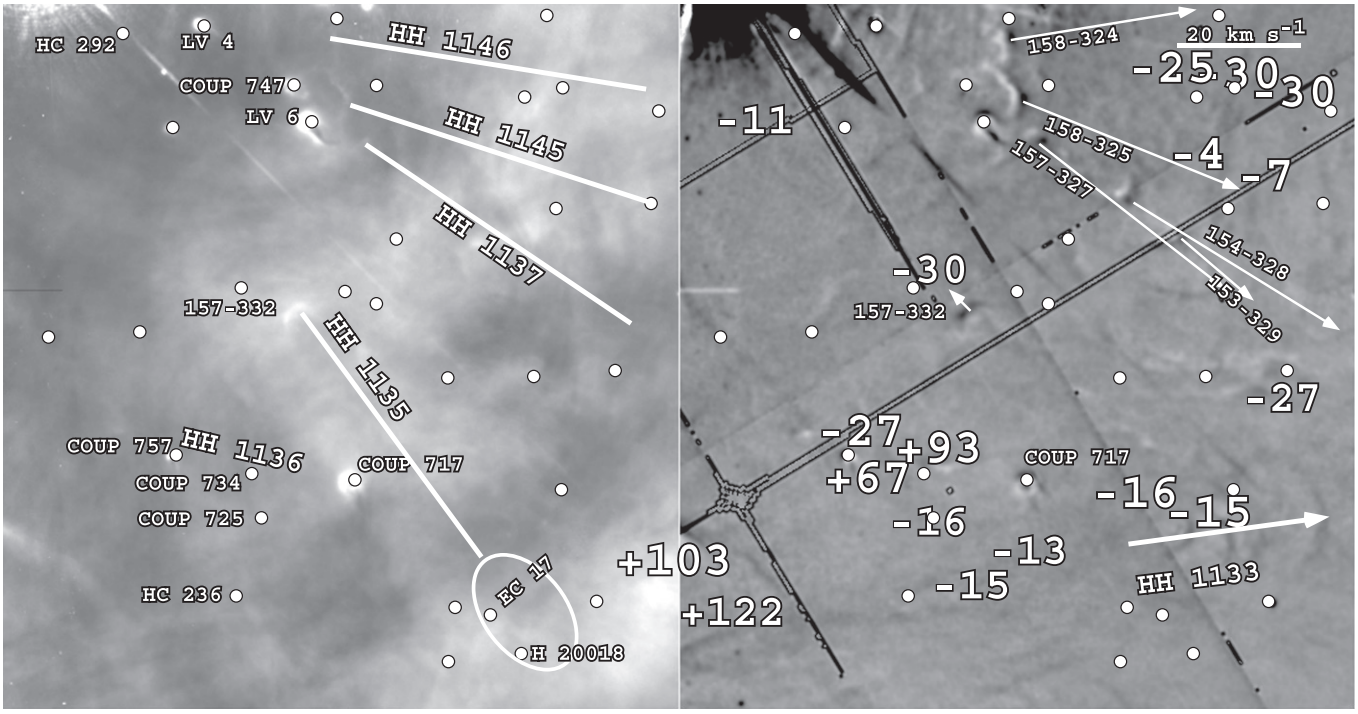

Figure 39. This pair of 21.″8 × 22.″7 images presents the F502N image (left panel) and motions (right panel) of an FOV designated as southwest in Figure 2. The velocity vector for shock 158-324 is shown at one-half the scale of the others. The filled circles represent SIMBAD sources in this region. The inserted numbers are values of the [O III] V_r. The other features are discussed in the text.

There are two well-defined large shocks (158-324 and 158-325) lying about 9″ west of θ^1 Ori C. Their motions are shown in the right panel of Figure 39. There is no obvious low-mass star that can be associated with them, and they are discussed in Section 5.11. There are three high-velocity [O III] features (−25, −30, and −30 km s^{-1}) in the upper right-hand of the right panel of Figure 39 that appear to be unrelated to any of the flows discussed here. They are also discussed in Section 5.11.

5.10.1. HH 1137

Three aligned shocks have been discovered in our new F502N images (Figure 39) that we designate as HH 1137. In addition to 157-327, 154-328, and 153-329, there is an additional, barely detectable, larger shock to the SW, along the same axis (250°) as the others. A backward projection of their axis passes through the proplyd COUP 747 and at a greater distance proplyd LV 4. It is impossible to judge definitively between the two as the source of HH 1137 as neither shows a jet on our images. The axis of HH 1137 passes about 0.″5 north of θ^1 Ori C (Section 5.11), well within the uncertainty of the projection of its axis.

There are no radial velocity features that would help in determining their 3D motion. Their axis also passes close to θ^1 Ori C (Section 5.11).

5.10.2. HH 1145

The partial bow shock labeled 158-325 is moving toward about 262°, which is compatible with its symmetry axis. Farther out in this direction are two [O III] radial velocity features of −4 and −7 km s^{-1}. Within the assumption that these are part of the same flow that produces the shock, the axis is 276°, and this points exactly at the nearby proplyd COUP 747 and at a much greater distance HC 292.

5.10.3. HH 1146

The moving knot at 158-324 would not ordinarily be assigned to a designated flow. However, there are a series of high-velocity [O III] features (−25, −30 km s^{-1}, and −30 km s^{-1}) lying beyond it. If these are associated with knot 158-324, then this forms HH 1146. The flow is then at 275°. The axis points back to LV 4 and the more distant proplyd HC 292.

5.10.3.1. Summary of Preceding Three Sections

In the previous three sections we identified three flows that all arise from a small region to the west of θ^1 Ori C. There are four candidate proplyd sources there (COUP 747, LV 4, LV 6, HC 292). Of these, only LV 6 fails to align with any of the flows. However, each of the flows aligns with two possible sources. The well-defined flow, HH 1137, aligns with the nearby COUP 747 and the more distant LV 4. The less well defined flow, HH 1145, aligns with the nearby COUP 747 and the more distant HC 292. The other less well defined flow, HH 1146, aligns with the similarly distant LV 4 and HC 292. It is possible that two of the stars produce Multi-Direction flows. However, if all the sources produce monopolar flows, then the most likely pairings are HH 1137 with LV 4, HH 1145 with COUP 747, and HH 1146 with HC 292.

5.10.4. HH 1133

The series of shocks labeled as HH 1133 (centered at 5:35:15.1, −5:23:37) align along a vector that passes between the two candidate stars HC 236 and COUP 725 (156.8-339.0). The latter star is listed in SIMBAD as COUP 725 (5:35:15.68, −5:23:39.0) and Lada et al. (2000) 49 (5:35:15.69, −5:23:39.5), which are probably the same source,

with the COUP position being used here. The alignment of the HH 1133 shock's symmetry favors HC 236. The V_T velocity vector shown in Figure 39 is the average result from the group of shocks. The [O III] V_r values (-16 and $-15\,\mathrm{km\,s^{-1}}$) are almost certainly associated with HH 1133, yielding $V_{OMC} = 53\,\mathrm{km\,s^{-1}}$ and $\theta = 52°$. The similarity of magnitude of the [O III] V_T values to those lying to the east (-16, -15,and $-13\,\mathrm{km\,s^{-1}}$) and their alignment along the symmetry axis of HH 1133 argue that these five radial velocity features are all part of the HH 1133 system. This means that its source lies in the direction of star HC 236, which is seen in optical through radio wavelengths.

5.10.5. HH 1136

The very high and positive [O III] V_T ($+103$ and $+122\,\mathrm{km\,s^{-1}}$) features in the lower left of the right panel of Figure 39 are part of the flow producing HH 518a and HH 518b, as discussed in Section 5.2, while the two other high-velocity features ($+67\,\mathrm{km\,s^{-1}}$/ and $+93\,\mathrm{km\,s^{-1}}$) are out of the line of progression of the two HH 518 flows and are probably not part of them.

This region also contains the proplyd COUP 717 (d155-338 [Bally et al. 2000], more accurately d155.1-337.2). This object is seen from X-rays through the radio continuum. It has the peculiar feature of a series of equally spaced bright rings of emission in F502N, extending out to 4.″2 toward 38°. Unlike the concentric rings in the Dark Arc (Sections 3.2.1 and 7.7.1), these have no detectable tangential motion.

There are two knots of high tangential velocity lying at 91° from COUP 717, the closer at 3.″3 and the farther at 7.″6. The high [O III] radial velocity features -27, $+67$,and $+93\,\mathrm{km\,s^{-1}}$ lie between these moving objects. The moving knots and the $+67$ and $+93\,\mathrm{km\,s^{-1}}$ are likely to be an outflow from COUP 717, which we designate as HH 1136.

The nearby $-27\,\mathrm{km\,s^{-1}}$ feature is probably associated with the all-wavelengths source COUP 734 (proplyd 157.3-337.9).

5.10.6. HH 1135

There is a conspicuous shock seen in F502N in Figure 39 whose motion is shown in the motions (right) panel and labeled 157-332. The symmetry axis of the shock is toward 50° and is shown as a line in the left panel of Figure 39, whereas the less accurately determined vector of the motion is 59°. Both the symmetry axis and the vector direction argue against an association with the nearby COUP 717. There are two stars that fall within the range of uncertainty of the symmetry axis; these are 151.6-340.6 at 226° and H 20018 at 227°. They are enclosed within an open ellipse in the lower left panel of Figure 39. The closer object (EC 17) has only been seen as a millimeter thermal object (Eisner & Carpenter 2006), and the farther object H 20018 has only been seen in the near-infrared (NIR; Hillenbrand 1997); therefore, neither are a promising source. The shock 157-332 and the possible sources are designated as HH 1135 in Figure 39.

5.11. Shocks near the Trapezium Stars

The Trapezium is at the core of the optical components of the ONC. On the average, the low-mass stars forming near this line of sight will be subject to a more intense ionizing radiation flux from θ^1 Ori C than stars farther away in the plane of the sky. This made it particularly worthwhile to study the flows in this region.

5.11.0.1. Shocks to the West of θ^1 Ori C

To the west of θ^1 Ori C we see (Figure 40) a series of nearly N-S shocks (about 10.″5 and 259°) that we call the Western Shocks. The individual components of this series are oriented toward θ^1 Ori C or slightly south of it, with the exception of the 157-327, 158-324, and 158-325 features that have been assigned to specific HH flows (Section 5.10).

5.11.0.2. Shocks to the East of θ^1 Ori C

Similar to the situation to the west of θ^1 Ori C, there is an extended series of shocks to the east that we call the eastern shocks. Most of these were identified in Bally et al. (2000) and assigned to HH 523. However, we are now able to assign them to the redshifted lobe of the bipolar flow that originates in the well-studied proplyd LV 2. The brightest proplyd is LV 2 (θ^1 Ori G, COUP 826). Its position is under the $-98\,\mathrm{km\,s^{-1}}$ entry in Figure 40. Among the many studies of this bright proplyd, Henney et al. (2002) established that it has a jet extending 2″ toward 120° and a fainter counterjet extending 2.″5 toward 300°. They found that the SE jet has a velocity of $+126\,\mathrm{km\,s^{-1}}$, in agreement with our value of $+123\,\mathrm{km\,s^{-1}}$. The counterjet probably accounts for the coincident $-98\,\mathrm{km\,s^{-1}}$ feature. Doi et al. (2004) created a detailed radial velocity map in [O III] of this region and showed that the redshifted flow could be traced to the east boundary of the Trapezium and the blueshifted flow extends to the west boundary. These flows follow the 120° and 300° orientation of the jet and counterjet of LV 2. They were given the designation HH 726.

Bally et al. (2000) defined HH 523 as shocks at 184-330, 183-327, and 179-326. We more accurately define these individual features as 184-329, 182.7-327.3, and 178.7-326.4. They lie at 120°, 117°, and 122° from LV 2 and almost certainly belong to HH 726. Were it not for the known flow from LV 2, one might assign as their source COUP 900, but the fit with HH 726 is excellent. Moreover, there is a high-velocity ($V_T = 160\,\mathrm{km\,s^{-1}}$) shock moving away from COUP 900, and we define that flow as HH 1143. We have found that COUP 900 (175.7-324.7) lies indistinguishably close to the proplyd 175.3-324.7 (176-325 in Henney & Arthur 1998). This proplyd has a cusp in F502N and a 0.″8 long tail pointed about 102°. θ^1 Ori C̃lies at 106°, and this tail is probably determined by the ablation of material by θ^1 Ori C.

The large shock at 182-336 is symmetric along a line to the star HC 271, and the measured motion shares this direction. We define this newly discovered flow as HH 1144. In summary, we can say that all of the eastern shocks can be assigned to known or new HH objects and HH 523 should now be considered nonexisting.

Most of the multiple high-velocity features about 10″ east of θ^1 Ori C are probably associated with the extended sequence of shocks assigned to the two branches of HH 518. Those may restrict identification of radial velocity features.

5.11.0.3. Shocks to the North of θ^1 Ori C

North of θ^1 Ori C at 7″ are a large number of outward-moving shocks lying nearly along an E–W line over a spread of PA values of 67°. They are less well defined than those in the

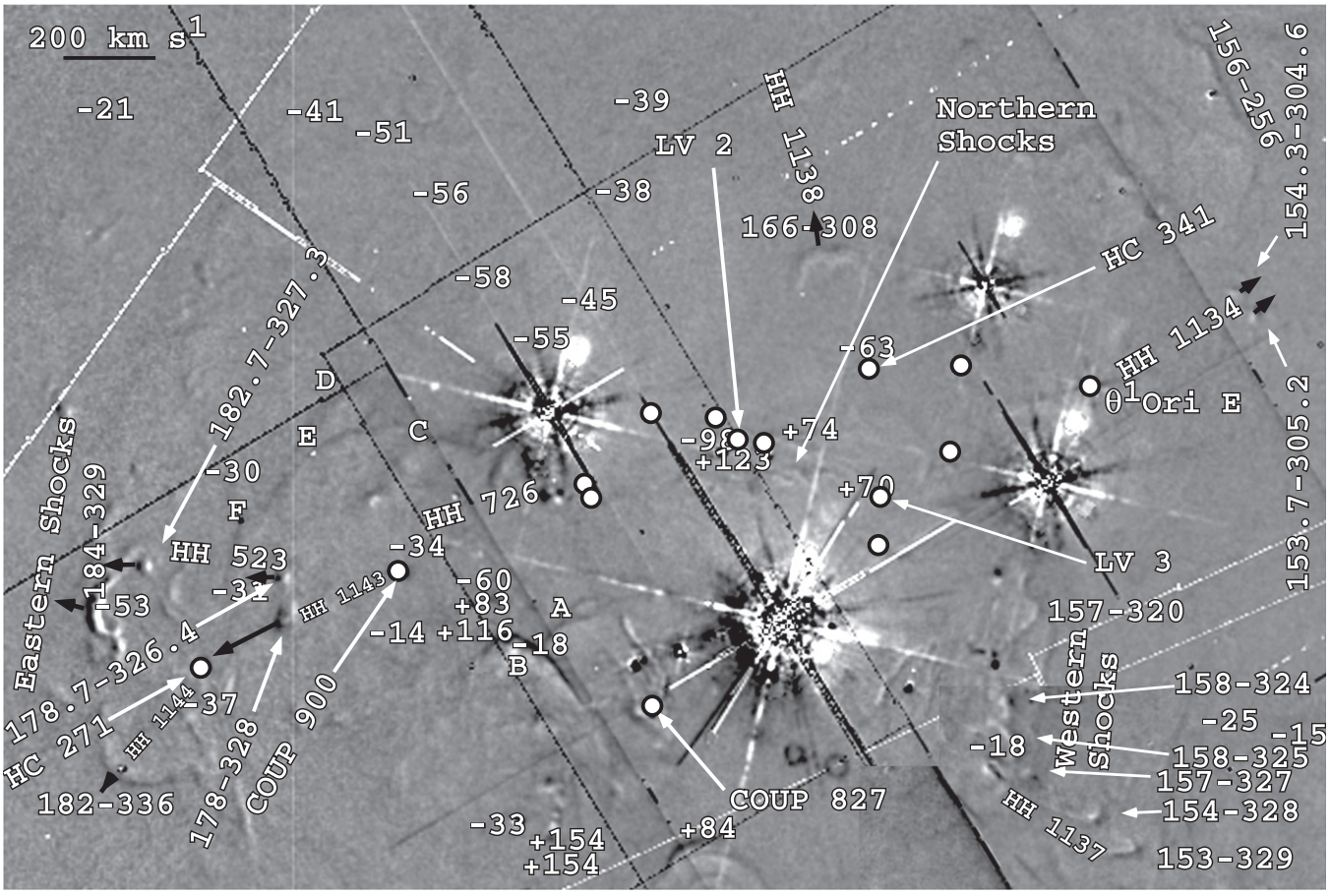

Figure 40. This 56.″8 × 38.″0 image presents the F502N motion image derived from non-WFC3 observations. The letters A–F designate features in the northern portions of HH 518a and HH 518b (Section 5.2). Radial velocities in [O III] are from Doi et al. (2004). Features discussed in Section 5.11 are labeled. Not all stars in this FOV are shown, but all sources in SIMBAD that fall within the four Trapezium stars are. Features with measured tangential velocities are shown with black arrows.

Western Shocks series, but again they are oriented away from θ^1 Ori C. We call these the Northern Shocks. There are multiple proplyds and several measured high radial velocity features in the vicinity of the Northern Shocks. However, the stars and the high-velocity features lie farther from θ^1 Ori C than the Northern Shocks.

Farther north of the Trapezium, at 15.″9 and 8° from θ^1 Ori C, lies the double shock 166-308, the west component of which approximately aligns with θ^1 Ori C (there are no intervening candidate sources) and the other toward the proplyd 164-316 (HC 341, which lies near the −63 radial velocity number). The tangential velocity vector indicates motion of the shock 166-308 away from HC 341. We designate proplyd HC 341 and 166-308-east as HH 1138.

There is a similar double-shock form at 156-256 symmetrically oriented toward θ^1 Ori D. It lies at 309° and 34.″5 from θ^1 Ori D. There is a more symmetric shock with the same orientation 3″ beyond it. However, an association of these shocks with θ^1 Ori D is uncertain because there are numerous intervening other candidates.

Near the right-hand edge of Figure 40 we see a pair of NW-moving knots (154.3-304.6 and 153.7-305.2). Their positions straddle the projection (±1°) of the HH 726 axis. However, their motions indicate that they arise from the nearby binary star θ^1 Ori E, and we designate this flow as HH 1134. θ^1 Ori E is a remarkable star as it is a spectroscopic binary, both components of which are mid-G giants (Herbig & Griffen 2006; Costero et al. 2008). Most unusual is that its systemic radial velocity is 8.3 km s^{-1} greater than the ONC. This means that the star is not dynamically part of the Trapezium. The orientation of HH 1134 is 309°. It is interesting that a line projected back 7.″7 from θ^1 Ori E passes through a small bow shock of the same orientation. Unfortunately, the proper-motion study of Olivares et al. (2013) does not give a useful result for the tangential motion of θ^1 Ori E with respect to the Trapezium stars considered as a group.

The broader context of the θ^1 Ori C features is discussed in Section 7.9.

5.12. Outflows near the HH 269 Axis

In our examination of the westward flows that constitute HH 269 we saw that there were numerous shocks that moved at similar PA values and had locations near the HH 269 axis. The optically dominant feature is the group of shocks lying to the east of the HH 269-east feature. A careful examination of these objects indicates that almost none can be identified with the HH 269 flow.

5.12.1. HH 507

This object is part of a complex system of overlapping shocks. This accounts for the assignment of membership and

the accompanying features in the literature changing with time. Our new images have allowed a more accurate identification of the flows involved.

HH 507 was first designated in Bally et al. (2000). They identified the shock 109-347 (designated here as 109.1-346.6) as being of a different orientation (315°) than the other shocks on which it is superimposed and different from the HH 269 axis (which we establish in this paper as 275°–276°). They reported a 10″ linear feature nearly along the symmetry axis of the shock and noted that this pointed south of the nearby proplyd d117-352 (117.0-351.3) and toward the complex of molecular outflows to the east. O'Dell & Doi (2003a) assigned the adjacent shocks at 111-352 (designated as 110.3-351.6 in this paper) and 113-345 to HH 507 and cast doubt on the association of HH 507 with the molecular outflows. Improved values of positions, designations, and angles are given below.

We note that on our F658N image the proplyd d117.0-351.3 (COUP 443) has a previously unreported microjet extending to 1.″9 from the central star at 56°. There is a low-ionization moving shock about 0.″3 from the star that is probably driven by this microjet.

There are multiple unassociated small shocks lying within the HH 507 bow shock. Their motions are usually along or near the HH 269 axis and several are probably part of that system of flows.

Figure 41 shows that the form and measured motions present a more complex picture than previously realized and that there are at least two overlapping flows. The axis of symmetry of the 109.1-346.6 shock that defines HH 507 (300°) lies along its tangential motion. The putative 10″ linear feature in the Bally et al. (2000) study lies along this symmetry axis. It is a low-ionization feature extending east only 8.″3 (this feature is shown as a black dashed line in the middle panel of Figure 41). We will call this the western HH 507 jet. The shock 112-349 lies along and is symmetric with this linear feature and is probably part of the HH 507 flow. Immediately beyond the east extension of the western HH 507 jet is the shock 115-352. It has a small shock 1.″0 west that is certainly part of western HH 507. The position of this shock is less than 1″ from the star COUP 423, but since the shock lies 0.″3 north of the star and is moving to the NW, COUP 423 cannot be the source of HH 507.

The more pronounced 115-352 shock is the westernmost feature of a series of shocks (8.″7 length and 291°) shown as white dashed lines in the middle panel of Figure 41 and which we call here the eastern HH 507 jet. The axis of the eastern HH 507 jet curves more rapidly at the small shock 121-355, remaining populated by small shocks and extending to 129-354 with a final orientation of 261°.

The combined western HH 507 jet and the eastern HH 507 jet are marked by a continuous nonmonotonic change in direction. This combined jet extends over 31″. There is no obvious source, but there are many candidate stars starting at about 5″.

5.12.2. Shocks near but Probably Unrelated to HH 507

Unlike the other shocks in the HH 507 region, 118.0-345.4 and the shocks to the west of it (117-345, 116-345, and 116-346) appear in both F502N and F658N. Their motion and symmetry indicate an axis of 284°, in agreement with the orientation of the small arc that constitutes 118.0-345.5. This orientation is close to the angle of the blueshifted SiO from COUP 554 but is displaced 2″ from that star. A link to the SiO flow would require a rotation by a few degrees CW beyond the region traced by the SiO emission. The PA of this grouping is sufficiently uncertain that it is impossible to establish a link to the SiO outflow. However, their motion is very nearly parallel to the HH 269 axis, arguing for an association with HH 269 in spite of the displacement.

Features closer to the bow shock of HH 507 are probably also associated with HH 269. Shocks 109.7-346.8 (which falls 0.″7 east of the large bow shock 109.1-346.6), 110.3-351.6, and 112.3-346.2 are not symmetric about the symmetry axis of 109-347; rather, their symmetry and motion are at about 284°. This is closer to the HH 269 axis (275°) than to the HH 507 axis (300°), arguing that these are associated with the HH 269 flow. Although their average [N II] V_T is large (32 km s^{-1}), there are no detected radial velocities for them. This indicates motion almost in the plane of the sky.

The moving knots a few arcseconds east of 112-352 appear to be independent of either HH 269 or HH 507.

5.12.3. A New Outflow Source South of HH 507

There is a faint large bow shock seen in the F658N motion image oriented toward the west, and its apex is at 107-357. There is a diffuse moving shock within the arc of the bow shock about 3″ from the peak. There are no other obviously related features, although the axis of symmetry passes close to the shock 121-353, whose motion is toward 107-357. The separation of these features is 21″. The axis of these features passes through the star COUP 478, which is their likely source. This star is seen in X-rays, our F547M image, and the infrared. We designate this flow as HH 1140.

5.12.4. A Possible Link of Large Shocks by Radial Velocity Data to the EC 13 Outflow Complex

There are a series of large shocks and high-velocity features that may be related to a compact region of multiple outflows. In the F502N motions panel of Figure 41 we see that the measured shock at 107-342 shares a similar orientation (304°) and tangential motion to the large shock containing 116-356. Shock 107-342 is seen best in F502N and is not the same as the shock at 109.1-346.6 that is the leading bow shock of HH 507.

Possible additional evidence lies in the [O III] radial velocities shown in Figures 3 and 41. All have velocities of about −40 km s^{-1} and an axis of about PA = 295°, about the same as the axis of 107-342 and 116-356 shocks (304°). Although parallel to the position of the west HH 507 shocks, they are displaced to the north by well more than the uncertainty of position of the radial velocities. The easternmost of this set lies on the large shock containing 116-356, and the westernmost is 107-342. It appears that these large shocks (116-356 and 107-342) are driven by a source at PA = 124°. This direction passes close to the source 137-408 (Zapata et al. 2006), which lies within a complex group of sources (Zapata et al. 2013) and has a bipolar SiO outflow (Zapata et al. 2006). In its discovery paper (Zapata et al. 2006) it was designated as 137-408, but later studies (Nutter & Ward-Thompson 2006) show that it should be called EC 13. The blueshifted flow (the reciprocal of the better-defined redshifted flow) has PA = 129° as shown in Figure 41. This suggests a causal relation.

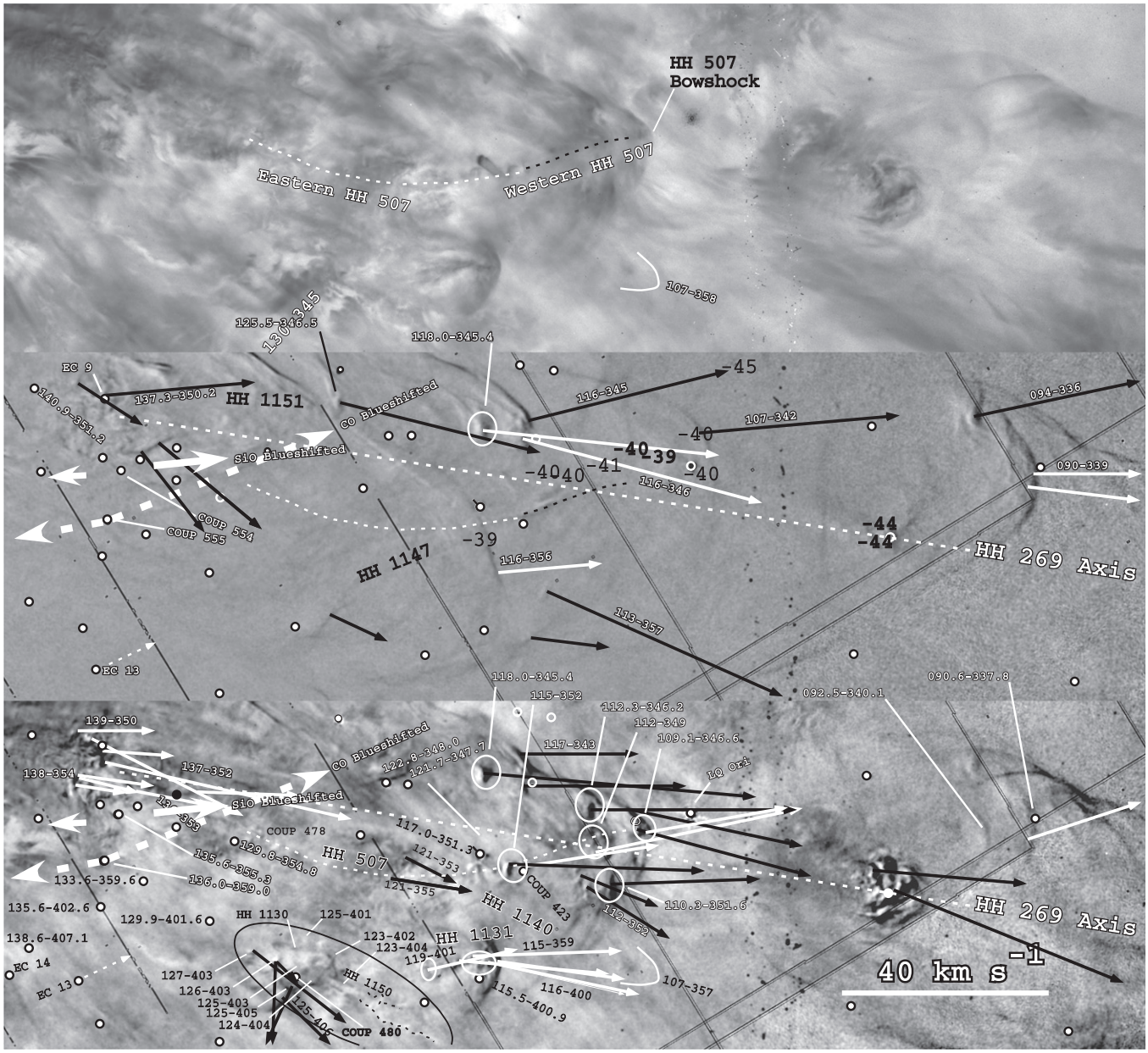

Figure 41. The FOV is designated as Large-West in Figure 2 is shown in this set of 89.″1 × 26.″9 images. The top panel is the F502N ratio image, with the motion images in the middle and lower panels. The velocity scale shown applies for all velocity vectors except those labeled 094-336 and 124-404, where the lines are at one-half the scale of the others. The curved lines shown crossing near star COUP 423 are faint patterns in the ratio and motion images. White and black vectors are used to distinguish different flow patterns, although the same color is used for different groups when it is clear that one is referring to different flows. The dashed line emanating from EC 13 indicates the direction of the blueshifted SiO outflow (Zapata et al. 2006). The thick black letters in the middle panel indicate [O III] radial velocities taken from Figure 3. The truncated black ellipse indicates the complex of objects called 126-406 in Sections 5.12.5 and 5.13. The open circle on the ellipse designating 109.1-346.6 marks the positions of the shock 109.7-346.8 discussed in Section 5.12.6.

A caveat upon using the [O III] radial velocities for identification of a flow is in the two nearby features with $-44\,\mathrm{km\,s^{-1}}$ lying exactly on the HH 269 axis. Although their position is exactly on HH 269-east, their velocities are very different from HH 269-east, as noted in Section 3.1. Clearly, these features are not part of HH 269, but if they are part of the two [O III] high radial velocity features to their west that are of about the same value, then the argument for linking those features to the large-scale shocks is destroyed. However, the latter association is unlikely, and we designate the EC 13, 116-356, and 107-342 sequence as HH 1147.

5.12.5. Motions near 126-406

The region enclosed in a truncated ellipse in Figure 41 contains evidence of several different flows and is designated here and in Section 5.13 as 126-406. In this section we consider only some of the features. The others are probably part of the HH 1148 system and are discussed in Section 5.13.

There are a series of barely resolved moving knots closed by an expanding boundary that we designate as 123-404. The boundaries slowly widen, being 0.″6 wide at their east end. The boundaries are clearly defined for 2.″6 and then become irregular, as shown by the dashed line extensions in Figure 41. The orientation of the linear boundary region is 258°. This

points at 129.9-401.6. We designate this flow as HH 1150. The probable source (129.9-401.6) has only been detected in the Two Micron All Sky Survey (2MASS).

There is another series of shocks near the top of the truncated ellipse that we designate as 125-401. Their orientation is 266°, which again points close to 129.9-401.6. Since it shares a common source with HH 1150, we include it within HH 1150.

There is a 1.″0 wide bow shock (123-402) pointed toward 283°. Its orientation and position indicate that 129.9-402.6 is not its source. The closest other candidate sources are COUP 582 at 23.″3 and reciprocal 283°, EC 14 at 24.″8 and reciprocal 287°, and EC 13 at 19.″5 and reciprocal 289°. In terms of the alignment, the best possible source is COUP 582, which has only been seen as an X-ray source (COUP 582). We designate this source and shock combination as HH 1130.

The moving knot 126-403 ($V_T = 37\,km\,s^{-1}$, 192°) and the moving shock 125-405 ($V_T = 17\,km\,s^{-1}$, 169°) do not have identified sources and must be unrelated to either HH 1150 or HH 1130. They are probably unrelated to the HH 1148 flow, although the other features are probably part of HH 1148 and are discussed in Section 5.13.

5.12.6. Shocks near but Probably Unrelated to Either HH 269 or HH 507

A different constellation of shocks are those at 137.3-350.2, 125.5-346.5, and 094-336 seen in the F502N motion image. In this case all of the shocks are of similar form, none appear as bow shocks, and the orientation is 283°. The easternmost shock (137.3-350.2) is close to the millimeter source EC 9, but a projection of this axis passes only 0.″4 south of the 6 cm radio source 140.9-351.2 (Felli et al. 1993), and that is the most likely source. There is no obvious alignment with the stars in the vicinity of the OOS region. We designate this system as HH 1151.

The symmetry and motion of the shocks at 090.6-337.8 and 092.5-340.1 indicate that they have a symmetry axis of about 308°, making them unlikely to be related to the shocks covered in the above paragraphs. This axis passes 1.″6 north of the star 096.5-346.7, which is superimposed on the HH 269-east complex of shocks, and this cannot be their source. Otherwise, there are no nearby stars along the axis of these two shocks.

5.12.7. HH 1131

HH 1131 is newly discovered in this study. As shown in Figure 41, it is composed of a well-defined large shock (115-359) symmetrically oriented along the path of a series of moving knots (grouped in the figures as 119-401 and 116-400). The symmetry of the shock and the alignment plus motion of the knots define an axis at 288°.

Projected backward, the axis of HH 1131 leads to the star COUP 480. That object is an unresolved point source in X-rays (Getman et al. 2005) and infrared observations (Hillenbrand & Carpenter 2000; Muench et al. 2002; Lada et al. 2004). There is no known optical counterpart, even on the GO 12543 F547M images.

5.13. HH 1148

The nearly edge-on silhouette proplyd 114-426 and its surroundings have been a subject of interest since first announced (O'Dell & Wong 1996) and studied in detail (McCaughrean & O'Dell 1996; Throop et al. 2001; Bally et al. 2015). As illustrated in Figure 42, there are a host of nearby shocks running from ENE to the SW, with the clearest component of the 108-430 grouping having been measured multiple times (Bally et al. 2000; O'Dell & Doi 2003a; Henney et al. 2007). At first this series of shocks appear to be like HH 626, which would indicate that they too represent the interaction of a large-scale outflow with the ambient low-ionization gas. However, this is not likely to be correct. Our new images have allowed determination of motions of multiple low-ionization features (some well-defined shocks, some linear, and some simply knots). We see in Figure 42 that these features move along a common axis of about 229° and are probably related to one another, but not to the proplyd 114-426. The linear blueshifted CO flow found by Bally et al. (2015) has a spur oriented like HH 1148 that must be associated with the 120-414 shocks. The peak intensity of this spur lies immediately to the NE of the [N II] shocks in 120-414. This argues for an association of the optical objects and a molecular flow. A counterargument to this is the optical features "upstream" discussed in the next paragraph. However, it could be that the molecular flows just graze the MIF.

The neighboring group of shocks that we collectively refer to as 126-406 and that are within the truncated ellipse in Figure 41 have at least four overlapping flows (Figure 41). There is a knot at 126-403 moving at $37\,km\,s^{-1}$ toward 192° and a bow shock at 125-405 moving at $17\,km\,s^{-1}$ toward 169°. These cannot be related to the HH 1148 flow. In addition, there is the HH 1130 flow probably coming from COUP 582 and the two branches of the HH 1150 flow coming from 129.9-401.6.

However, 127-403 ($23\,km\,s^{-1}$, 246°), 126-403 ($6\,km\,s^{-1}$, 239°), and the bow shock 125-406 ($19\,km\,s^{-1}$, 235°) may be associated with HH 1148. Their average motion is toward 240°. Projections of the velocity vectors of 125-406 and 127-403 are shown as white arrows at the top of Figure 42. The northern well-defined component of HH 1148 (120-414) lies at 227° from 126-406.

These three shocks within 126-406 align (227°) almost exactly with the common axis of HH 1148 (229°), and their tangential velocities (240°) are directed almost toward the northern components of HH 1148 (120-414). The major components of HH 1148, including the 126-406 group, are shown as open circles in Figure 2. Their velocity vectors are shown in the upper left of the F658N motion image in Figure 42. It is almost certain that the three shocks of 126-406 are members of the HH 1148 flow.

We have also looked for other members of this flow and for candidate sources. A projection crosses the putative source for HH 1150 (129.9-401.6) and, within the uncertainty of the flow direction, numerous candidate source stars beyond that. There are multiple molecular outflows along the projection, but none of them align with HH 1148. The projection passes through the middle of the Figure 11 FOV, where the number of candidate stars is a maximum. This line passes within one arcsecond east of the center of the concentric arcs at 137.6-348.8 discussed in Sections 3.2.1 and 7.7.2. It also aligns with the symmetry axis (57°) of the large WNW-pointing bow shock 141-345 (feature II in Figure 22). That bow shock has a series of otherwise invisible high negative velocity [O III] features leading to it at 74°. If the high-ionization shock 141-345 is part of the low-ionization HH 1148 flow, this means that the source lies between the last [O III] radial velocity feature at 5:35:13.6, −5:23:47 and the 126-406 features. Given

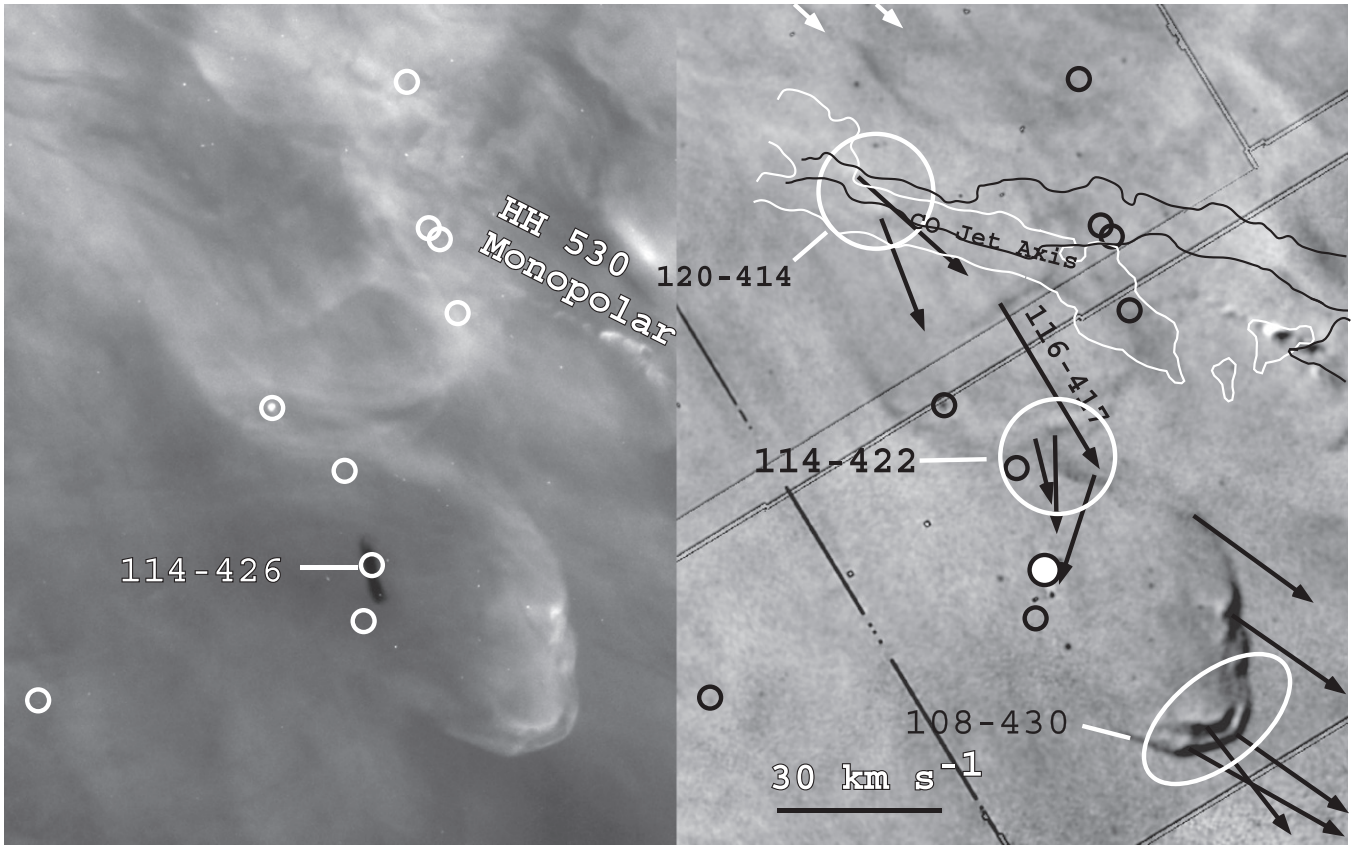

Figure 42. This 24.″4 × 30.″6 FOV is designated as HH 1148 in Figure 2. It shows the F658N image on the left and the F658N motion image on the right. The large silhouette proplyd 114-426 is shown and labeled, with only the positions of other SIMBAD sources depicted. Only two individual velocity vectors are labeled in addition to two groupings of velocity vectors. The velocity vectors extending to the image boundary have been truncated. The velocity vectors of the components of the HH 530 monopolar jet have not been shown. The uppermost white vectors are discussed in the text. The outer contours of the CO flows (blueshifted—white; redshifted—black) recently discovered by Bally et al. (2015) and discussed in Section 5.3 are shown in the right panel.

the large number of stellar sources along this line, we cannot make a convincing identification of the HH 1148 flow.

5.14. Possible Outflow from DR 1186

In their study at 1.3 cm wavelength, Zapata et al. (2004b) detected a microjet (about 0.″5) extending toward 324° ± 4°. The compact source, which is also seen at 3.6 cm (Zapata et al. 2004a), lies nearly along the middle of an irregular low-ionization linear feature of about 4″ full length oriented about 331°. Zapata et al. (2004b) argued that DR 1186 could be the source of both HH 202 and HH 528. Although we do not detect a tangential velocity along the optical filament, there is a nearby feature seen to move in the F658N motion image (Figure 20), but the direction of the motion indicates that it is probably part of the HH 269 flow. In our spectra we see a faint Hα component at $V_r = -50\,\mathrm{km\,s^{-1}}$ and another in [N II] at $V_r = -53\,\mathrm{km\,s^{-1}}$, which may be an indication of an outflow from DR 1186.

6. IONIZATION SHADOWS

In an earlier *HST* study, O'Dell (2000) studied linear features oriented toward the dominant ionization star in both the Orion Nebula and the Helix Nebula. It was established that these features are ionization shadows cast by small objects (proplyds in the case of the Orion Nebula and knots in the case of the Helix Nebula). LyC radiation stops at the ionization front of the obscuring object, leaving a shadowed zone outside of it. In the case of the Orion Nebula, the shadowed region is no more than moderate ionization and [O III] is the primary way of detecting the gas. In the shadowed region [O III] is not found as that tapered column is subjected only to ionization by LyC photons coming from recombining ionized hydrogen. The shadowed region is only evident when there is ionized gas present, a feature used by O'Dell et al. (2009) to determine the distribution of gas in the inner parts of the Orion Nebula.

6.1. A Rapidly Rotating Ionization Shadow

One of the radial shadows studied by O'Dell (2000) is double in our F502N motion images. It is labeled as "Ionization Shadow" in Figure 22. This is a low-ionization ([O III] weak–[N II] strong) feature extending from 58″ to 128″ from the dominant ionizing star (θ^1 Ori C), and its middle lies along 256.°1. Its width at 66.″4 from θ^1 Ori C is about 0.″87. It has been displaced by 0.°44 CW between the first-epoch (GO 5469) and second-epoch (GO 12543) observations. The other shadows studied by O'Dell (2000) that fall within the GO 12543 FOV do not show this magnitude of rotation. There are three candidate sources for the obscuring object. They are the only objects within ±7° of the PA of the low-ionization shadow.

The first candidate is the proplyd 158.0-326.7 (LV 6). The true nature of this object was revealed in one of the first images made after the initial servicing mission of the *HST*, when

O'Dell & Wen (1994) recognized it as a proplyd. In a subsequent study Bally et al. (2000) described it as a dark-disk object with an optically visible central star and an ionized crescent facing θ^1 Ori C (incorrectly calling it d158-326). The chord perpendicular to a radial line toward θ^1 Ori C is seen on the GO 12543 images to be 0.″31. Using the SIMBAD position for θ^1 Ori C (5:35:16.46, −5:23:22.9) locates the proplyd at 10.″7 distance at 249° from θ^1 Ori C (GO 5469 images give 10.″7 at 250°). The second candidate is COUP 747, a much fainter proplyd with an ionized crescent facing θ^1 Ori C. The chord of the crescent is 0.″29. It is 9.″5 from θ^1 Ori C at 254° (GO 5469 images give 9.″6 at 255°). The third candidate source of the ionization shadow is the proplyd 161-324 (LV 4). It has much higher surface brightness in F656N than LV 6 and is only marginally resolved, with a diameter of $\leqslant$0.″2. It has a narrow low-ionization tail of about 2.″9 in the θ^1 Ori C anti-direction. It is 6.″3 from θ^1 Ori C at 256° (GO 5469 images give 6.″1 at 256°).

The width of the ionization shadow should scale linearly with increasing distance from the obscuring source. This means that the 0.″87 width of the shadow (at 66.″4 from θ^1 Ori C) should project to a size of 0.″14 at LV 6, 0.13 at 158.5-325.5, and 0.″08 at the distance of LV 4.

The better agreement of the inferred size of the obscuring source and the agreement of the PA of the low-ionization shadow and the orientation of the object with respect to θ^1 Ori C indicate that the proplyd LV 4 is the object producing the shadow.

The rotation of the ionization shadow must be due to the change of orientation of the obscuring source with respect to θ^1 Ori C. As noted above, this was about 0.°44 CW over the 16.8 yr period between the first- and second-epoch images. If the source is LV 4, this corresponds to a relative tangential motion of 1.2 pixels perpendicular to 256°, corresponding to a velocity of 7 km s^{-1}. This is a problem.

Van Altena et al. (1988) included θ^1 Ori C in their determination of proper motions of cluster members and found that it was moving about 2.3 mas yr^{-1} toward the SE, corresponding to 1.0 pixel motion in our study. If the van Altena et al. (1988) motion is correct and the proplyd is stationary, then the shadow would have moved 0.°4 CCW. This is of similar magnitude but in the opposite direction of the observed rotation. Photographic determination of the motion of bright stars with respect to faint stars, as was done by van Altena et al., is notoriously difficult, and a recent, more definitive study by Olivares et al. (2013), using *HST* images, indicates that the relative motion within the Trapezium cluster stars is only a few kilometers per second, comparable to the velocity dispersion of the low-mass members (Jones & Walker 1988). It is best to leave this discussion at this point with the conclusion that the rotation of the low-ionization shadow indicates that θ^1 Ori C and LV 4 are rotating with respect to one another at a rate of 0.°026 per year (a period of 14,000 yr), which corresponds to a relative tangential velocity of 7 km s^{-1}. The radial velocity study of Tobin et al. (2009) indicates a wide dispersion of velocities of stars in the declination range of the Trapezium, and a deviation of 7 km s^{-1} is possible. If the high proper motion of θ^1 Ori C posited by Tan (2004) is correct, we would see a pattern of motions of the radiation shadows, which we do not.

6.2. Additional Ionization Shadows

A well-defined nonmoving ionization shadow is at 225°. At 58.″8 from θ^1 Ori C it is 0.″8 wide. The PA value aligns with the well-defined proplyd COUP 717. Using the SIMBAD position of 5:35:15.509, −5:23:37.18, the calculated PA is 224.°9, and its measured chord is 0.″36. This chord size projected to 58.″8 is 1.″05, so there is adequate agreement between the observed and predicted shadow size if this proplyd is causing the ionization shadow. The rotational motion of the ionization shadow is less than 0.5 pixels (0.″04), corresponding to an amount of PA change of $\leqslant$0.°019. This corresponds to a maximum relative velocity perpendicular to the line connecting θ^1 Ori C and COUP 717 of $\leqslant$2.5 km s^{-1}, a number compatible with the known velocity dispersion of the lower-mass members of the ONC.

There is a sharp ionization shadow whose northern boundary is at 255.°4 from θ^1 Ori C. This angle passes through the northern side of the ionization boundary of proplyd 158.5-325.5. At position 5:35:11.85, −5:23:41.0 this northern boundary is 72.″1 from θ^1 Ori C and the projection of the ionized chord (0.″29) of 158.5-325.5 would be 2.″2. The area immediately south of this point is complex, and the south boundary is not visible. Even in the simpler region at 5:35:10.75, −5:23:46.1 (at 89.″7 from θ^1 Ori C), where the predicted south boundary of the projection would occur (predicted 2.″7), there is no clear evidence of a boundary. At the well-defined northern boundary there is no indication of rotation of the ionization shadow.

There are a series of unresolved linear features grouped over about 1.″0 and extending from 5:35:13.4, −5:23:42.2 to 5:35:11.1, −5:23:56.7 with 244°. These show up best in Figure 22. The NE end passes less than an arcsecond south of the shocks composing HH 1127, but these are clearly unrelated. The projection back to θ^1 Ori C passes 0.″6 south of the center of LV 6 and well outside of the ionization shadow of the proplyd. The other proplyds in the area are even farther from the projected line to θ^1 Ori C. The complex structure makes it impossible to tell whether this is the case of an obscuring proplyd rotating rapidly around θ^1 Ori C.

7. DISCUSSION

In Section 3 through Section 6 we have presented the results on a plethora of objects within the Huygens Region. These objects have been as small as the microjets of less than 1″ to shocks at up to 1000″ from their sources. Summarizing this wealth of information is inevitably flawed, but we have ordered this section into subjects that are arguably separate from one another, usually proceeding from large scale to small scale, with an integrating summary at the end.

7.1. Nature and Origin of the Major Northwest and Southeast Flows

The correct identification of sources of flows depends on many factors. A tangential velocity vector indicates an origin along the reverse direction from the moving feature. Where possible, a high-velocity jet produces another line useful for determining where orientation angles cross. The smaller the distance to the intersection, the more accurately that intersection is determined and the more lines of motion available, leading to a more accurate location of the source. In a system like the Major Northwest (dominated by HH 202) to Southeast

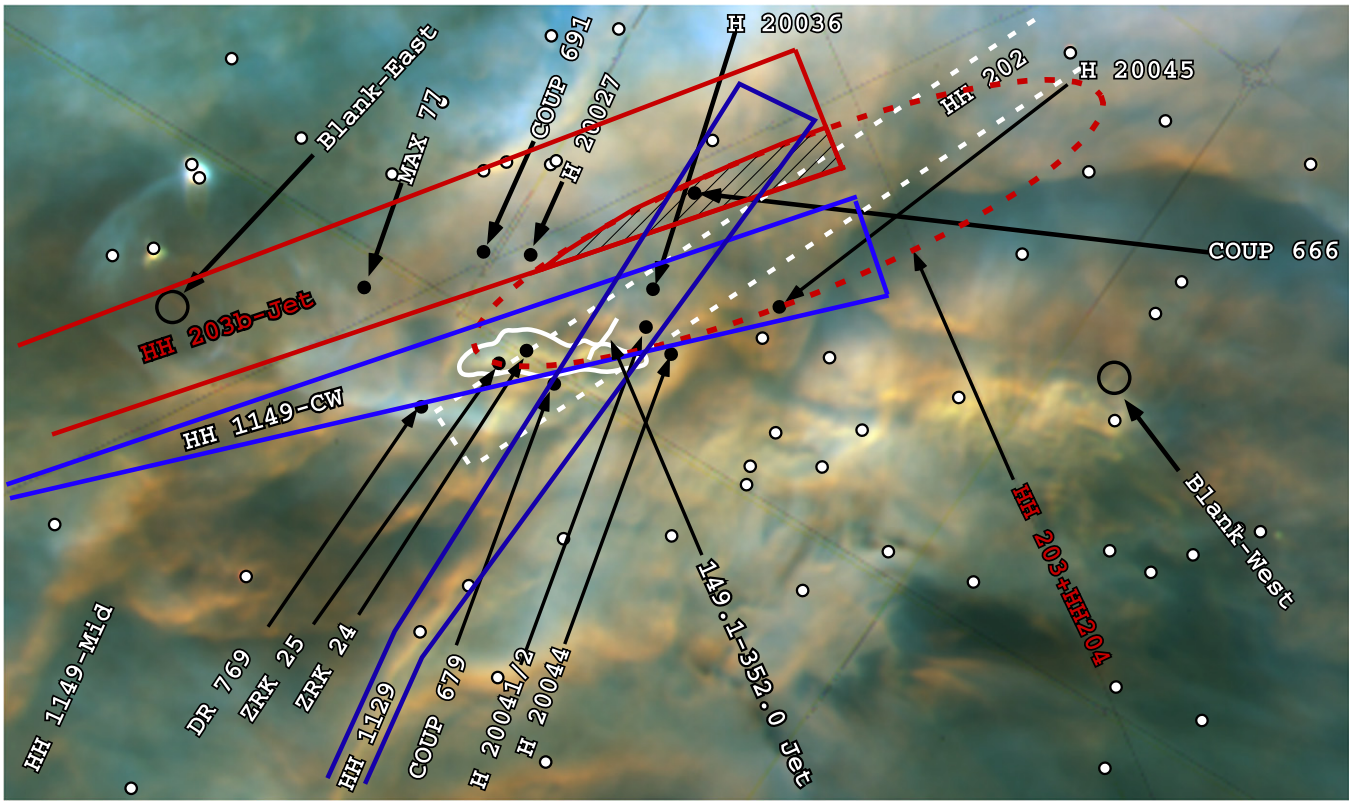

Figure 43. This $47\farcs1 \times 27\farcs8$ *HST* image shows a field of view near the center of Figure 5. The color coding is blue for F502N, green for F656N, and red for F658N. Stars relevant to the discussion of sources are shown as filled circles, those in black being the most relevant here. The large black open circles show the positions of inferred positions (see Section 7.7) without SIMBAD sources. The colored lines are explained in the text.

Flows (dominated by HH 203 and HH 204), we have the advantage of vectors over a wide range of PA and a subsequently accurate determination of the source. In the case of the major east–west flows (various features of HH 529 moving east and the HH 269 features moving west), it is more difficult. Earlier work that combined the data from these nearly orthogonal flows led to the identification of the OOS, under the assumption of a common origin. In this paper we have shown that the two systems may be independent, yet their sources can be determined, both lying slightly outside the OOS.

Henney et al. (2007) discussed these shocks in their earlier study. That study had to rely on less accurate motions and was done before HH 1149 was recognized. They could only argue that there was a source near the OOS.

Appreciation of what is happening demands understanding the inner features that we have been discussing thus far and the outer features beyond them. All are discussed in the following six sections. We will see that a coherent picture develops.

7.1.1. HH 202

In Figure 43 the dashed white band labeled HH 202 is a 2″ band centered on the jet leading to HH 202-S. The source is most likely to lie within this band near the region of highest stellar column density. Examination of the other shocks associated with HH 202 (at greater and smaller PA values) indicates a source in this area, but the angles are too imprecisely determined to narrow down the source precisely. Stars H 20036, H 20041/2, and COUP 679 fall within this large area.

7.1.2. HH 203 and HH 204

The large red oval marked HH 203 + HH 204 is the region where the lines of symmetry of these bow shocks converge. Since the range of angles is small, this area is large. Stars COUP 666, H 20036, H 20045, H 20041/2, ZRK 24, and ZRK 25 fall within this large area. A red trapezoid with sides divergent by $\pm 1°$ indicates the axis of the HH 203b jet. Among the many stars in this large area, stars COUP 666, H 20037, and COUP 691 are closest to the area of convergence of the HH 203 and HH 204 symmetry axes. Under the assumption that HH 203, HH 204, and the HH 203b jet share a common origin (the cross-hatched region in Figure 43), the best candidate source is COUP 666. It is visible in X-rays (Schulz et al. 2001; Getman et al. 2005), optical (Da Rio et al. 2009), NIR (Jones & Walker 1988; Herbst et al. 2002; Hillenbrand 1997; Hillenbrand & Carpenter 2000), and the longer-wavelength infrared (Lada et al. 2004). The spectral type has been reported as K6–M4 (Hillenbrand et al. 2013).

7.1.3. HH 1149

The other dominant SE flow is HH 1149. Although neither boundary of its fan of linear features and bow shocks can be determined accurately, there is a well-defined jet that probably forms that CCW boundary and allows identification of the source.

The shock used to define the CW boundary has a symmetry axis of 120°. The corresponding blue trapezoidal source box (blue lines in Figure 43) contains the stars H 20045, H 20036, H 20041/2, ZRK 24, and ZRK 25. Close examination shows that this shock is complex and therefore its symmetry axis is

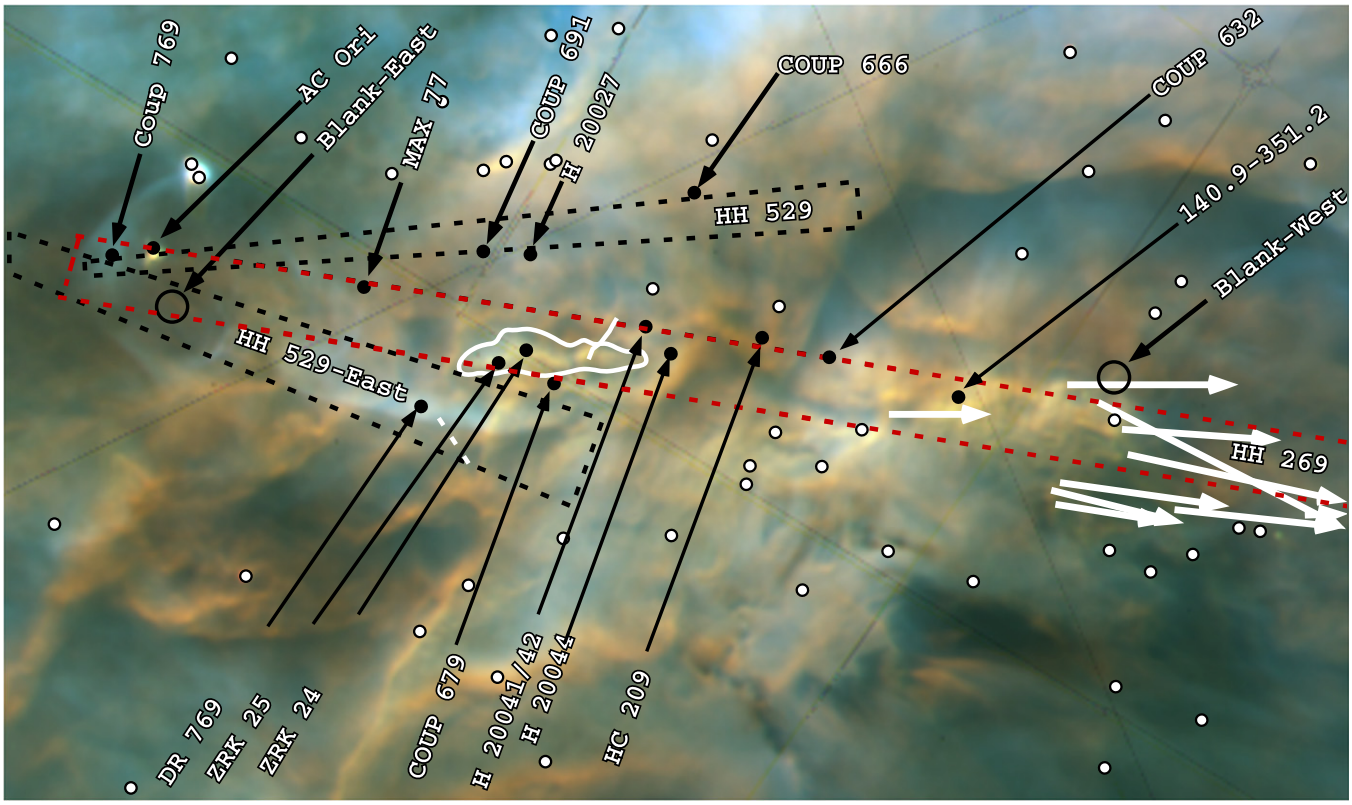

Figure 44. Like Figure 43, except now the colored lines discussed in the text are those relevant to understanding the east–west flows.

not well defined. This means that the source box is probably much larger than drawn and is of limited aid in identifying a source in this crowded field.

The CCW boundary of HH 1149 varies from 168° in the south and then changes to 160°, again being depicted with blue lines in Figure 43. It is notable that the center of this box passes very close to the linear jet, which points toward COUP 666. The jet's center is at 5:35:14.91, −5:23:52.0 (hence a designation as the 149.1-352.0 jet) and crosses the east-jet with no obvious interaction. The jet clearly misses (Figure 12) star H 20036. This means that the CCW boundary of HH 1149 is caused by the sequence of objects COUP 666, the 149.1-352.0 jet, the 160° linear feature, and the 168° linear feature.

The most CW shock assigned to HH 1149 has a smaller symmetry axis PA than those to the CCW direction from it. This progression of PA values is what defines the group as a common flow. However, the PAs of the interior shocks' symmetry axes are generally difficult to determine. The bow shock 158-405 is oriented toward 144°, while the linear feature 154-401 is moving toward 150°. Both of these directions are similar to their PA value (141° and 148°, respectively) from COUP 666. This argues that both these interior shocks originate from that star.

This leaves the most CW shock of HH 1149 in limbo, as it shares the form and low ionization of the other HH 1149 bow shocks, but its formal symmetry axis PA is too small to fit into HH 1149. Close examination shows that this shock is complex, and therefore its symmetry axis may not be well defined.

The feature HH 1149-Mid in the lower left of Figure 43 resembles the CCW boundary of HH 1149 (designated as HH 1129). As noted before (Section 4.4), this feature projects to the HH 528 Base feature and it may be the source of the HH 528-west flow. Its origin is uncertain, although its north portion is at 166° and a projection passes very close to the Blank-east region.

7.1.4. Features near the Bright Bar

In Section 4.5 we saw that there are numerous features along the Bright Bar that are oriented toward the OOS region. These include a large low-ionization pair of bow shocks inside the Bright Bar aligned with HH 203 and HH 204 (Section 4.5.3) and a large number of bow-shock-like features that we designate as crenellations (Section 4.5.2) that are found both inside and beyond the Bright Bar from the direction of HH 203 CCW to beyond the HH 528-Cap. Whether or not these are formed in the tilted surface of the Bright Bar or in the foreground Veil is unknown; however, they are likely to be associated with outflows from the OOS region. If from a single source, this would demand collimated flows in multiple directions over a confined range of PAs; if from single stars, this would demand collimated flows in similar directions from at least 12 different stars.

7.1.5. Outer Features

Henney et al. (2007) argued that the distant (633″ from Orion-S, 146° from the OOS) low-ionization shock HH 400 (Bally et al. 2001) lies on an extension of HH 203+HH 204 +HH 528 and that they could be related. Henney et al. (2007) found a larger shock they called HH 400-S farther out (789″ at 148°), as well as a third feature composed of multiple smaller shocks designated as HH 400-SS (970″ at 162°). With our new division of HH 528 into two parts and a more careful examination, we believe that these conclusions must be revised.

The orientation of HH 203 is 123°, and that of HH 204 is 127°. Although curves in flows can occur (Bally et al. 2006b), this is quite different from HH 400's PA (146°). It is most likely that HH 400 and HH 400-S are associated with the HH 528-east flow at 142°, which probably originates in COUP 632. HH 400-SS is probably associated with the flow from HH 528-west (163°), which is fed by HH 1149-Mid (162°). The latter series of features is designated as HH 1142.

Henney et al. (2007) pointed out a series of shocks on *HST* images that we determine to be at 590″ and 321° from the OOS. They concluded that these were associated with either what was producing HH 202 or the fingers of outflow from the BN–KL region. Their forms indicate an origin in the direction of the OOS. Their PA (321°) is larger than that of the most CCW HH 202-N shock (327°) but is close to the alignment of HH 202-S (323°). Figure 23 shows that there are numerous shocks extending beyond the bright HH 202 shocks (Section 4.2), and it seems safe to conclude that the NW shocks are part of the HH 202 shocks. Their distance (590″) is only somewhat smaller than HH 400 (633″), but, unlike HH 400, there are shocks seen farther out. This is consistent with the model of the EON (O'Dell & Harris 2010), where its ionization boundary is farther to the SE than it is to the NW.

7.1.6. NW and SE Flow Summary

HH 202 is a multiple-member set of bow shocks with a high-ionization jet, with bow shocks outside of the HH 202 features and distant shocks (NW shocks) even farther out. An origin has not been established because the jet does not continue into the OOS region and the varied PA bow shocks are not well enough defined to allow backward triangulation within the band of possible sources of the jet. The star COUP 666 lies slightly outside the path of the HH 202 jet, although it should be noted that in Figure 23 the jet curves toward this star.

HH 203 and HH 204 are more complex than previously appreciated. HH 203 is actually two superimposed bow shocks, components HH 203a and HH 203b. The latter is aligned with a high-ionization jet. HH 204a is a well-defined bow shock with a faint irregular shock farther out designated as HH 204b (at a slightly larger PA). The region of convergence of the symmetry axes of HH 203a and HH 204a overlaps with the extension of the jet pointing toward COUP 666.

HH 1149 is a series of partial and complete bow shocks. The CCW boundary is ill defined but probably is due to the outflow 149.1-352.0 jet that originates in COUP 666. Although the well-defined interior bow shocks also seem to arise from COUP 666, the most CW boundary complex bow shock is oriented at too small a PA. The HH 1149-Mid linear feature aligns with the HH 528 Base feature and may give rise to the HH 528-west flow. Its origin may be in the Blank-east region.

The above information means that COUP 666 appears to have SE outflows toward HH 203b (123°), HH 203a (124°), HH 204a (127°), the linear jet at 160°, the CCW boundary of HH 1149, and crenellation features at 127°–135° and 140°–160°. In addition, COUP 666 is likely to be producing the multiple bow shocks within HH 1149. This means that COUP 666 has multiple outflows over 123°–160° and, if the SW-Group of features are included, to 184°. This means that COUP 666 has produced a lobe of collimated outflows to the SE. If COUP 666 is also the source of the HH 202 shocks, then this means that it is producing shocks to the NW at 296°–327°. If the SW-Group of features is not included with the COUP 666 features, the range of angles of the NW flow (296°–327°) is very similar to the SE flow (123°–160°), with the center of the ranges in nearly reciprocal directions (142° and 312°).

COUP 632 is producing the outflow HH 528-east (142°), which eventually connects with HH 400 (147°) and HH 400-S (148°).

These considerations lead us to the important conclusion that COUP 666 is producing multi-fingered lobes of bipolar flow, with the lobes pointed NW and SE.

All of the measured components of the two sides of the bipolar flow are blueshifted. This is probably because the outflows are bipolar over a wide range of directions in space, although concentrated to the NW and SE. We see this motion in the plane of the sky as a pair of fans of shocks over multiple directions. The redshifted components of the outflow will be directed to behind the MIF, and because of the jump in extinction that is expected upon passing through the PDR, the blueshifted components are not seen optically.

We see a similar pattern in the Allen–Burton fingers arising from the BN–KL explosive event. There is a rich literature of studies of the Allen–Burton fingers and the BN–KL source (Hu 1996; Schultz et al. 1999; Kaify et al. 2000; Lee & Burton 2000; Vannier et al. 2001; Gustafsson et al. 2003; Kristensen et al. 2003; O'Dell & Doi 2003a; Doi et al. 2004; Colgan et al. 2007; O'Dell & Henney 2008; Fukue et al. 2009; Furuya & Shinnaga 2009; Plambeck et al. 2009; Zapata et al. 2009, 2011, 2012; Bally et al. 2011). The Allen–Burton fingers are simply the NW portion of a multi-element bipolar flow, with a less well characterized optically invisible similar flow (McCaughrean & Mac Low 1997) to the SE. These fingers are the result of a single event estimated to have occurred 500 yr ago (by the tangential motions of the radio sources involved; Rodríguez et al. 2005) or no more than 1000 yr ago (by the tangential velocities of the optical shocks; Doi et al. 2002).

Unlike the Allen–Burton fingers, it is not likely that the NW and SE features discussed here arose at the same time and from a single event. We see only one driving jet for each of the two best-defined shock systems (HH 202 and HH 203). It appears more likely that we are seeing the result of collimated bipolar flows occurring at different times and directions.

7.2. Nature and Origin of the HH 269 and the HH 529 East–West Shocks

7.2.1. HH 269

The westward-moving HH 269 feature has been shown in this paper (Section 3.1) to begin with the feature HH 269-east and to extend beyond the new HH 269-westmost features to join with H_2 knots even farther west. These features are of low ionization, although [O III] is sometimes seen, and a series of small shocks to the east of HH 269-east are likely to be caused by the same invisible flow at 276° (Section 3.1). Their motion is shown by the white arrows in Figure 44. The westernmost velocity vector is important since it indicates that the source lies to the east of 140.9-351.2. When radial velocities are available, they are all blueshifted. In Figure 44 we show a band ±1″ from the path of the well-defined HH 269 axis as parallel dashed red lines. The source of this flow is most likely to occur within the central region, which contains stars H 20044, HC 209, ZRK 24, ZRK 25, MAX 77, AC Ori, and COUP 769. Detection in multiple wavelength ranges is a good indication of a very young star. As shown in Table 1, only two are seen

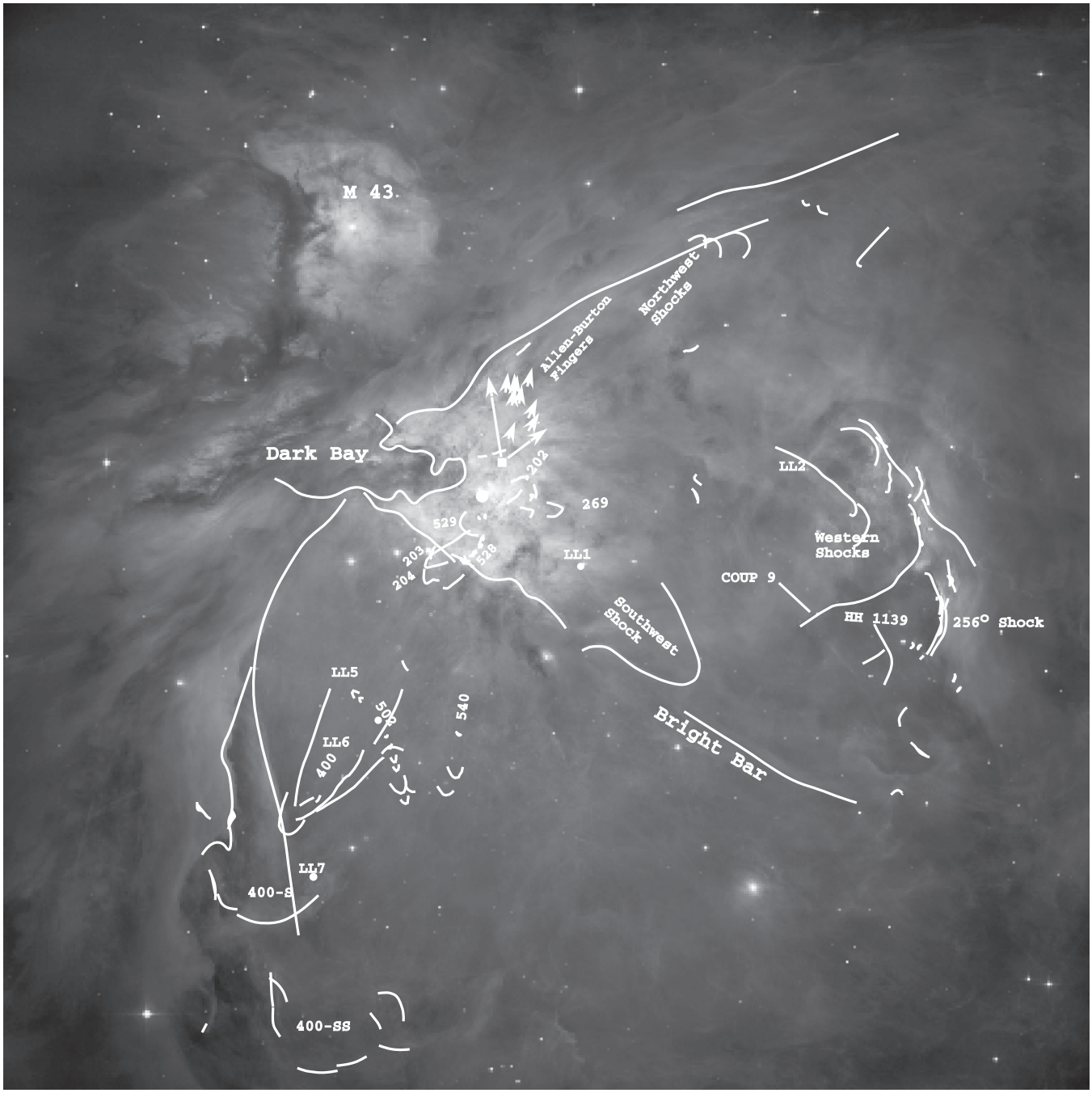

Figure 45. This 30′ × 30′ *HST* image of the Huygens Region, M43, and most of the EON (Henney et al. 2007) has been annotated with white lines highlighting features outside of the Huygens Region found by Bally & Reipurth (2001) and Henney et al. (2007). The relation of the inner and outer features is discussed in Section 7.6, with the exception of the Allen–Burton fingers originating from the BN–KL region, which have been adequately discussed in Section 7.1.

outside of a single wavelength range. AC Ori is seen in all wavelength bands, and COUP 769 is seen in the X-ray (Getman et al. 2005) and infrared (Lada et al. 2004); these are the best candidate sources.

7.2.2. Outer Shocks Possibly Associated with HH 269

Henney et al. (2007) have shown that there are a large number of shocks near the edge of the optical EON that lie west of HH 269. They indicate that an association with HH 269 is unlikely unless a strong change of PA occurs. The shocks are found from about 256° to 283° from the OOS. This includes the PA of 276° for HH 269, but there are no outer shocks at that angle.

7.2.3. Origin of the HH 529 Shocks

In this study we have shown that in addition to the HH 529-I, HH 529-II, and HH 529-III high-ionization shocks (axis 109°) there is an apparently independent shock we have designated as HH 529-east (axis 84°). In Figure 44 we show trapezoidal boxes that begin with the center of the defining shock and diverge by ±1°. These are not extended beyond the concentration of known stars.

The box for HH 529 (white dashed lines) contains no stars, although stars COUP 666, H 20027, COUP 691, AC Ori, and COUP 769 fall on the edge of the box. COUP 666 and AC Ori are seen at all wavelengths, H 20027 and COUP 691 only in the infrared, and COUP 769 in X-rays and the infrared. The star COUP 632 identified earlier by Rivilla et al. (2013) on the basis of extrapolations from a large distance falls well outside the box for candidate stars.

The three stars seen in more than one wavelength window are the best prospects for the source. COUP 666 has already been invoked as the most likely source of the large-scale SE flows. If this is the source of the HH 529 shocks, then this would be simply an extension of the PA range of its outflow. AC Ori has a jet with orientation 47° (O'Dell & Henney 2008), which does not align with HH 529-east's symmetry axis of 109°, making it a less likely source. COUP 769 is well located within the source, but the nearby series of moving knots headed at 82° argues against an association.

These considerations leave COUP 666 and AC Ori as the prime candidates. The HH 529-I shock is fully developed, and AC Ori is centrally located within the shock and slightly offset. These considerations, in addition to the nonalignment with the known AC Ori jet, mean that COUP 666 is the most likely source. This star is not deeply imbedded (we see it as an optical star), and that is attractive because the HH 529 shocks are high ionization and are formed within the [O III] region of the nebula (Blagrave et al. 2006). Placing the source (COUP 666) in front of the MIF explains the bow shock's ionization.

7.2.4. Origin of the HH 529-east Shock

The HH 529-east high-ionization shock's potential source box (again with ±1° divergence and as black dashed lines) contains only the inferred source Blank-east (159-355) that has no known SIMBAD stars and the millimeter source (Da Rio et al. 2009) DR 769. The star COUP 769 falls on the edge of the box, and as noted previously, a line of 82° from the center of the defining bow shock through several west-moving intervening high-ionization knots passes indistinguishably close to COUP 769 (seen in X-rays and the infrared) and the Blank-east center.

This means that HH 529-east can be explained by collimated flows from either COUP 769 or a hidden source in Blank-east. Since no source is seen in Blank-east, any source there must be highly embedded, and it would be difficult to explain the high ionization of HH 529-east. This leaves COUP 769 as the most likely source for HH 529-east.

7.2.5. Summary of the Likely Sources of the East–West Systems

HH 269 has as its best candidate sources AC Ori and COUP 769. The lack of alignment of the reciprocal of the AC Ori jet (227°) and the HH 259 axis (276°) means that by default COUP 769 is the more likely source.

HH 529 is most likely driven by a collimated outflow from COUP 666. This would extend the PA range of SE shocks driven by this star. The different nature of these shocks (high ionization) indicates that this region of the outflow quickly moves into gas ionized by θ^1 Ori C.

HH 529-east is most likely driven by COUP 769. The knots seen nearby at 82° and the HH 529-east shock (84°) are the strongest arguments.

The above conclusion means that HH 529 is simply one more flow from COUP 666, whereas COUP 769 is now revealed as the most likely source of HH 269 (276°, reciprocal 96°) and a counterflow (HH 529-east, 84°). If both of these flows originate from the same source as a nearly bipolar flow, it must mean that the opposite flows are not exactly aligned. The alternative is that even for COUP 769 we are seeing a multi-branched outflow. Unfortunately, there are no radial velocities for HH 529-east. If it is blueshifted, like the HH 269 features, then this strengthens the argument for a multi-flow coming from COUP 769.

7.3. Nature and Origin of HH 1132 and HH 1141

In Figure 46 we see both the east-jet and the axis of the east-second-jet (Section 3.2.2) as extracted from Figure 14. The axis (107°–108°) of the east-moving east-jet projects into the white trapezoidal box with ±2° divergence. The east-second-jet (axis 87°) is less well defined by radial velocities, so we have projected its trapezoids (divergence ±3°) in both directions.

7.3.1. The East-jet (HH 1132)

The alignment of the east-jet argues that the source of this jet is either HC 209, H 20044, or the more distant COUP 632. There are no other nearby compact sources lying within the small uncertainty of the angle of the jet. H 20044 lies at the end of the east-jet form and its radial velocity features, while objects HC 209 and COUP 632 become candidates as one moves farther to the west. HC 209 and H 20044 are relatively faint and seen only in near-IR surveys (Rodríguez-Ledesma et al. 2009). Although H 20044 is listed in the early X-ray catalog of Orion sources (Feigelson et al. 2002), it does not appear in the later COUP (Getman et al. 2005) catalog.

In contrast with the other candidate stars, COUP 632 is a luminous source seen in the full energy range of surveys (Lada et al. 2000, 2004; Muench et al. 2002; Smith et al. 2004; Getman et al. 2005; Robberto et al. 2005). COUP 632's characteristics have been summarized well in Appendix A9 of Rivilla et al. (2013). Rivilla et al. (2013) establish that it suffers high extinction in the infrared, even more in the X-ray, and represents emission from a star of 0.5–1.5 $M_\odot$, most likely being near the larger value. These characteristics make it the most attractive candidate source for the east-jet.

7.3.2. Features Related to the East-jet

As seen in Figure 46, there is a high-ionization partial bow shock whose apex lies 5.″8 along an extension of the east-jet axis. This is labeled east-shock in Figure 14. Its tangential motion is difficult to determine, but one sees in Figure 14 that it lies along the projection of the east-jet. It has numerous high-velocity [O III] features that have about the same velocity as the east-jet. The high ionization is consistent with the transition of ionization as the driving jet emerges. There are no obvious related features farther along the line of projection.

Therefore, we have a sequence of features arising from COUP 632. As the collimated flow breaks through an ionization front (either the MIF or the ionization front of the Orion-S cloud, as discussed in Section 3.2.2), it forms the high tangential and radial velocity features and finally produces the east shock. This sequence can be designated as HH 1132.

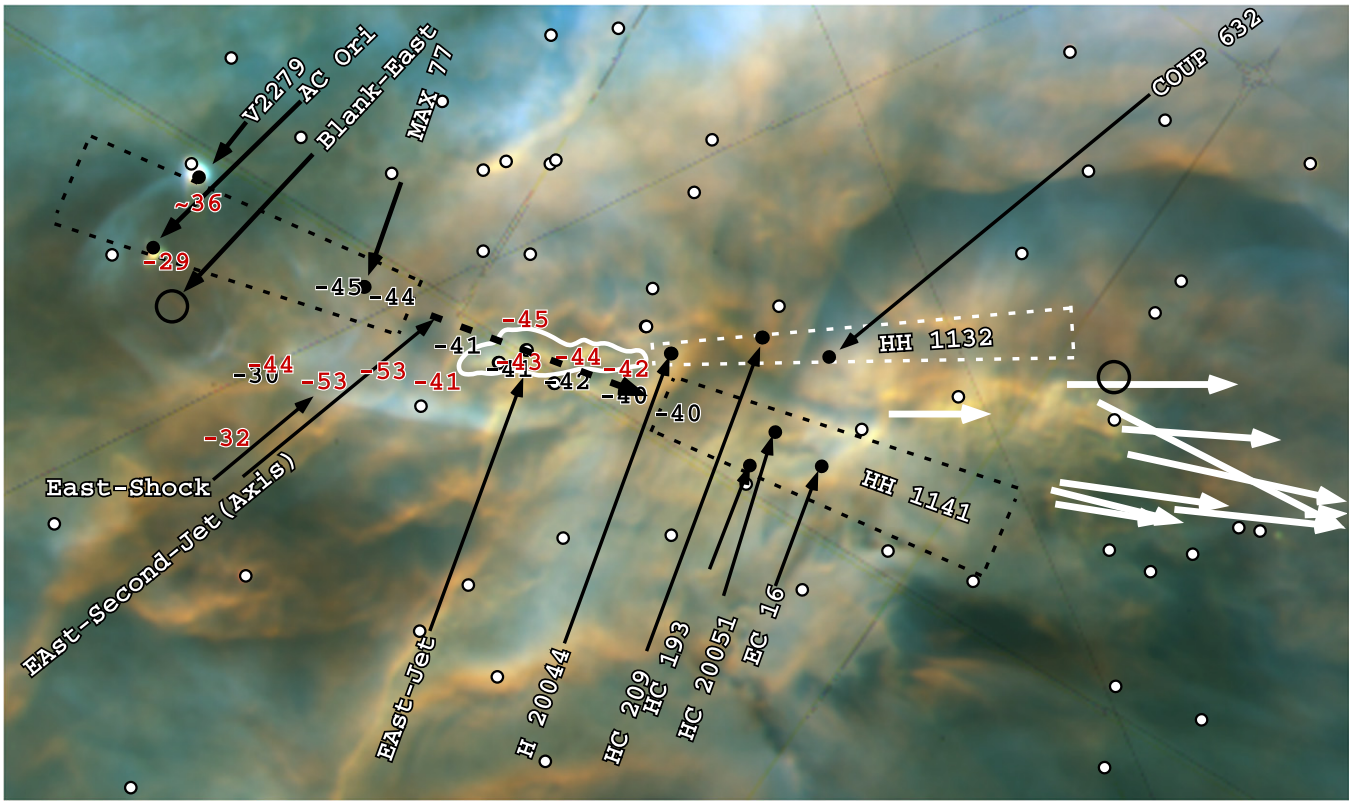

Figure 46. Like Figure 43, except now the black and white features discussed in the text are those relevant to understanding the east-jet and east-second-jet flows. The black numbers indicate radial velocities in [N II], and the red numbers indicate radial velocities in [O III].

7.3.3. The East-second-jet (*HH 1141*)

HH 1141 is defined only by [N II] radial velocities. Since there are no associated tangential velocities, we do not know whether it is moving east or west, and the trapezoids probably containing its source star are shown projected in both directions from the feature.

If it is moving west, there are three candidate sources MAX 77 (infrared only), AC Ori (X-rays, visual, infrared, radio continuum), and V2279 (X-rays, visual, infrared). It does not align with the microjet (47°) from AC Ori, and V2279 actually falls slightly outside the possible source trapezoid. MAX 77 is the only good candidate, especially as the [N II] high-velocity features begin at that point.

If it is moving east, there are again three candidate sources HC 193 (infrared), HC 20051 (infrared), and EC 16 (infrared). All are relatively weak sources seen only in the infrared, with HC 20051 and EC 16 being more favorably located.

This means that the only good candidate source is MAX 77, and the east-second-jet features are expected to be moving to the west. We can define the new HH object HH 2014ESJ as the source, MAX 77, and the seven [N II] radial velocity samples to its west. The axis of this flow is drawn as a thick black vector in Figure 46.

7.4. An Outer Flow (*HH 1139*)

In Figure 45 we show most of the boundary of the EON. One of the best-defined shocks is labeled as "256° Shock" in this figure. It aligns well with the bright ($V = 12.57$) star COUP 9. The spectral type of COUP 9 has been reported as spectral type K1, K0IV, K3III-IVe, and K1 (Hillenbrand et al. 2013). It is seen in X-rays, optical, and near-IR wavelengths. If this is the source producing the 256° shock, we designate the COUP 9 + 256° shock as HH 1139.

7.5. Relation of Huygens Region Outflows to 21 cm Absorption in the Veil

In a recent study of high-velocity H I absorption lines in the Veil (angular resolution about 6″), van der Werf et al. (2013) detected several regions of blueshifted material that are probably related to the large-scale outflows detected at the boundaries of the Huygens Region.

Their broad (about 60°) velocity system L is centered on the HH 203 and HH 204 shocks and extends SW to the end of the HH 528 shocks. The fan of shocks identified as part of HH 1149 overlaps in PA with feature L, but HH 1149's most CW PA coincides with HH 203's jet, and its CCW PA limit goes beyond feature L. The radial velocity of the L feature is 15 km s^{-1}, quite different from that of HH 203 (-46 ± 15 km s^{-1}; Doi et al. 2004) and HH 204 (-18 ± 18 km s^{-1}; Doi et al. 2004). These shocks are probably interacting with the foreground Veil, but the neutral material is in a mass-loaded region ahead of the shocks.

Their system F was found around the NW boundary of the series of shocks that include HH 202, and the width of the feature coincides with the NW flows identified in Section 4.2 and Figure 23. System F has the partial shell structure expected from a series of shocks striking and accelerating the foreground Veil. Feature F's H I absorption radial velocity (about $V_r = -1$ km s^{-1}) contrasts with the optical shock feature velocity of -39 ± 2 km s^{-1} (Doi et al. 2004), again indicating

that the H I absorption comes from a decelerated region ahead of the shock.

Samples taken on van der Werf's features C (lying to the SW within the Huygens Region), D, and G show no optical features in [N II] or [O III] that resemble the H I absorption features. This indicates that these H I features are not related to the optical features we see nearby.

7.6. Relation of the Southwest Shock to the Orion-S Region

In Figure 45 we see that the "southwest shock" is at 246° from the molecular outflow from EC 14. This direction is only slightly less than the direction of the outflow, which begins with 245° and changes to 238° after deflection. Perhaps the deflection began later than the jet driving the "southwest shock." If this is the case, then it is noteworthy that the well-defined shock 108-430 (see Figure 23) lies at 247° from EC 14, and this shock may be a result of the same outflow as the "southwest shock." Bally et al. (2000) assigned this shock to the group called HH 530 close to the silhouette proplyd 114-426 but concluded that it was likely to be driven by a source in Orion-S. We are able to reach the same decision, but with more accuracy as the outflow from EC 14 has been only recently been defined in detail (Zapata et al. 2013).

7.7. Flows without Candidate Sources

There are three cases in which there seem to be flows without an apparent source. In the first two the angle on the sky back to the sources is small. In the third a point of origin is not obvious. The first is in the west region and appears in Figures 11 and 19; the second is near AC Ori (Figure 19). It is remarkable that the features are most visible in [O III], which must lie farther from the MIF than the [N II] layer, making it harder to conceal the source. The third feature is HH 1154 (Figure 38), which is quite different from the first two.

7.7.1. Flows Originating within the Dark Arc

We note that in the west F502N motion image (Figure 11) there are three groups of nearly circular moving arcs, the first lying NNE of compact source EC 9, the second lying ENE of that same object, and the third to the NNW. Their directions of motions are shown by the thin dashed white arrows in Figure 11. Their point of intersection (5:35:13.76, −5:23:48.8, with an uncertainty of about 1″) clearly lies north of source West-A, and there is no candidate for a common source. We will call this position Blank-west. Although there are large arcs in WFPC2 and WFC3 images owing to fringing in the filter-detector combination, these occur at a much larger scale and cannot produce the small-scale fringes that we see. The better-defined north series is moving about 16 mas yr^{-1}, corresponding to 34 km s^{-1}. If they arise from a source near the intersection, this time was about 300 yr ago. This structure is unique. It is unlikely to be a light echo from a long-period star because it shows up only in the [O III] emission. It may be that it is the result of varying-intensity large-scale prestellar wind from an object whose obscuring disk is aligned with the direction to the observer.

7.7.2. Flows Originating from near AC Ori

In Section 5.5 we presented the arguments that the earlier conclusion of O'Dell & Henney (2008) linking the HH 998 shock feature to a putative counterjet from AC Ori was possibly incorrect and that COUP 769 had to be considered as a candidate source. Neither one is a good explanation, and we discuss here other features that share a common origin with the HH 998 shocks.

There is another well-defined shock in the vicinity that is identified as 156-352 in Figure 19. Lines drawn perpendicular to the motion of the 156-352 shock and along the symmetry axis of the HH 998 shock intersect at 5:35:15.91, −5:23:54.5 with an uncertainty of less than 1″. We will designate this as Blank-east. There are no sources in the SIMBAD catalog at this position.

Other, more distant shocks may also originate from this source-free area. The well-defined shocks at 155-354 lie at 5.″9 along 277°, 148-346 14.″9 at 265°, and 153-359 9.″4 at 24.2° (essentially on an extension of HH 998). All of these show symmetry and motions along a line originating in the source-free area. Their radial velocities are uncertain since they lie along an extension of the east-jet and the local numbers near 155-354 are similar in value to those in the east-jet.

In Section 5.5 we discussed the fact that there are a series of faint moving knots 8.″3 east of the obscured star COUP 769, shown as a dashed vector in Figure 19. Although their axis passes close to COUP 769, it also passes into the empty source region identified above and may also arise from there. We call these HH 1152.

In addition to the above multi-angle flows, we have shown in Section 7.1.3 that the linear features HH 1149-Mid and HH 528-west may also arise from Blank-east. If so, it is one of the most elaborate regions of outflow in the Huygens Region.

If the HH 998 shock arises from the undetected source, it is about 145 yr old, and if the 156-352 shock arises from the same region, it is about 450 yr old. The other shocks would be much older (155-354, 2700 yr; 148-346, 4600 yr; 153-359, 2200 yr). These numbers indicate that collimated outflows in different westerly directions are occurring essentially at the present and began at least about 4600 yr ago. The source or sources have undergone collimated ejections in two quite different directions about 300 yr apart. These properties are not unlike other sources found in the Huygens Region, but the big difference is that the source or sources have not been detected in any studies.

7.7.3. HH 1154

The curious object HH 1154 has the highest V_{OMC} (200 km s^{-1}) of all the Huygens Region objects. It is only 5.″2 from the proplyd 139.2-320.3 (COUP 593), which has been detected in X-rays through infrared radiation. But the most straightforward explanation of the change of shape and position of HH 1154 indicates that it is moving exactly toward the proplyd. There are no candidate sources along the axis of motion. If we have interpreted the two-epoch images correctly, the source of HH 1154 has not been detected.

7.8. Types of Flows

Even though this study has analyzed in detail only a fraction of the Huygens Region, it does include most of the core of the ONC. This makes it possible to consider this a representative sample of outflows from young stars in a rich cluster. The results can be generalized to similar clusters, commonly

Table 5
Summary of Data on Flows

Designation in Text	Section	Figure	Source
	Monopolar Flows		
HH 507	5.12.1	41	Unknown, many candidates
HH 512	Bally et al. (2000), O'Dell & Henney (2008)	O'Dell & Henney (2008), Figure 14	COUP 728
HH 528-east	4.4, 7.1.3, 7.1.5	23	COUP 632?
HH 528-west	4.4, 7.1.3, 7.1.5	23	Blank-east?
HH 529	3.3.1, 7.10, 7.2.3	16, 17, 19, 45	Probably COUP 666
HH 530	5.3	34	EC 14
HH 625	4.6,4.6.1	25, 26	COUP 555
HH 1127	5.6	36, 37	MAX 46 or the more distant COUP 602
HH 1128	5.7	36	EC 9
HH 1129	4.1, 7.1.3, 7.1.6	19, 20, 43	COUP 666
HH 1130	5.12.5	41	COUP 582
HH 1131	5.12.7	41	COUP 480
HH 1132	3.2.2,7.3.1	12, 13, 14, 15, 16, 46	COUP 632
HH 1133	5.10.4	39	HC 236
HH 1134	5.11	40	θ^1 Ori E
HH 1135	5.10.6	39	EC 17 or H 20018
HH 1136	5.10.5	39	COUP 717
HH 1137	5.10.1 and 5.10.3	39	LV 4
HH 1138	5.11	40	HC 341
HH 1139	??	44	COUP 9
HH 1140	5.12.3	41	COUP 478
HH 1141	3.2.2, 7.3.3	14, 46	MAX 77
HH 1142	5.5, 7.7.2, 4.1, 7.1.3, 4.4, 7.1.5	19, 20, 23, 44	Blank-east
HH 1143	5.11	40	COUP 900
HH 1144	5.11	40	HC 271
HH 1145	5.10.2 and 5.10.3	39	COUP 747
HH 1146	?? and 5.10.3	39	HC 292
	Bipolar Flows		
HH 269 + HH 529-east	3.1, 2.4, ??, 3.3.1, 7.2.3, 7.2	5, 6, 7, 16, 17, 18, 19, 20, 45	Most likely source, COUP 769
HH 540	4.5.4	24	Most likely source Beehive Proplyd 181-826
HH 510	5.1	29, 30, 31, 32, 33	Edge-on dark proplyd 109.4-326.7
HH 1157	5.3.1	34	V2202
HH 726	5.11	40	LV 2
HH 888, LL1	7.8	44	LL Ori–COUP 245
HH 1147	5.12.4	41	Likely source EC 13
HH 1148	??	2, 42	Undefined, too many candidate sources
	Multi-direction Flows		
HH 202 + HH 203 and HH 204	4.2, 4.3, 4.5, 4.5.2, 7.6	22, 23, 24, 43, 44	Most likely source COUP 666
HH 518a & HH 518b	5.2	22, 39, 40	V2279
HH 626	5.4	35	V1328
HH 998	5.5, 7.7.2	14, 19	Probably Blank-east
HH 1149	4.1, 7.1.3	20, 43	Unidentified
HH 1150	5.12.5	41	Probably 129.9-401.6
HH 1151	5.12.6	41	140.9-351.2
HH 1152	5.5, 7.7.2	19, 46	Unknown
	Unassigned Flows		
HH 1153	5.8	11, 19	Unknown
Near Dark Arc	5.7	36, 37	Unknown
HH 1154	5.9,	23, 38	Unknown[a]

Note.
[a] Source is COUP 593 if the shock is moving westward.

thought to be the primary source of field stars. In this section we categorize the outflows of different types and where possible identify their sources. In Table 5 we have divided them into five categories: monopolar, bipolar, multi-direction, unassigned, and hot star. In each case we give the section(s) where the flow is discussed, the figure(s) where it is presented, and the candidate source. In some cases a flow appears in more than one category. Two previously known flows (HH 512 and HH 888) that have been studied in detail elsewhere are included in Table 5 for completeness.

There are 27 monopolar flows; 21 have been discovered in this study, and two of the previously known flows are reassignments of portions of previously known flows. There are nine bipolar flows; one is a combination of a well-known flow plus a new feature, two are newly recognized portions of a known flow, and three are newly discovered flows. There are nine multidirection flows; four of them are newly discovered, and the others are known flows or reclassified known flows. Three flows are unassigned, one of which was known before.

A monopolar flow may have an aligned counterpart that is aimed in a direction where there is insufficient material to produce an optically visible shock. Where we have good radial velocities for a monopolar feature, with the exception of HH 518, they are blueshifted. This argues that the redshifted flow penetrates behind the obscuring PDR of the MIF, or that the flows are moving into the dense material of the foreground Veil, with the redshifted flow passing into the lower-density regions within the cavity lying between the Veil and the MIF. All theories of star formation call for a polar ejection in opposite directions, so the monopolar flows are probably the result of these selection effects.

Some of the monopolar and bipolar flows may actually be parts of multi-direction flows. Those objects listed in that category in Table 5 have identifiable flows in more than one nearby direction in the plane of the sky, and where there are radial velocities, they are both blueshifted. The detection of paired blueshifted or redshifted flows in opposite components of the bipolar flows would move them into the multi-direction category. It is worth noting that the SE redshifted component of the HH 726 flow from LV 2 shows a range of angles of its outer shocks from 117° to 122° even though the flow is very linear at 120° in its inner region.

In summary, we can say that observational selection effects may account for the monopolar objects not having the bipolar features expected theoretically. Adding these two categories (monopolar and bipolar) yields 32 systems of flows, where there are nine multi-direction flows. More complete data may move some of the former flows into the latter.

This gives the surprising result that multi-direction flows represent a significant portion (about one-fifth) of all known flow systems in this study, and correction for the observational selection effects can only increase this fraction. This means that in addition to the well-known intermittency of collimated outflows, either there must be multiple unresolved stars forming with different orientations in space, but at essentially the same time, or effects are present that cause the collimated jets to have rapidly varying directions. In private correspondence John Bally points out that some of these multi-shock features could be due to wide-angle outflows (like in HH 626) undergoing instabilities or having had to punch through obstructing media.

7.9. The Shocks near the Trapezium in Context

In Section 5.11 we saw that there are multiple shocks to the east, west, and north of the Trapezium. Most of these can be assigned to designated HH flows, although the sources are sometimes ambiguous. However, there are two sets of multiple shocks lying almost parallel to one another, the Northern Shocks and the Western Shocks. The individual shocks in both sets are oriented away from θ^1 Ori C. Either θ^1 Ori C has had multiple collimated outflows at various PA values but all at about the same time, or (the more likely explanation) these shocks are at instabilities in zones of interaction of a large-scale wind from θ^1 Ori C with the ambient nebula gas.

θ^1 Ori C is known to be a triple system with component masses of 36, 8, and 1 $M_\odot$ (Vitrichenko 2002; Kraus et al. 2009; Lehman et al. 2010) and the strong stellar characterstics of very hot stars (Howarth & Prinja 1989). This means that there is ample opportunity for instability-produced phenomena in several directions.

These two sets of shocks are very different from structures seen farther away from θ^1 Ori C that arise from the large-angle stellar wind from that star. They are much closer than the "[O III] Shell" discussed in O'Dell et al. (2009), where it is argued that this marks a boundary of material shocked by the high-speed stellar wind from θ^1 Ori C. This is in agreement with arguments presented in Massey & Meaburn (1995). None of these shock structures coincide with the larger but inner-nebula C-shaped high-ionization zone identified by O'Dell et al. (2009). This C-shaped feature is open in the direction (SW) of the Orion-S cloud and has an irregular radius of about 34″, and it was designated there as the [O III] Shell (O'Dell et al. 2009). It may be that this feature is actually circular as projected on the plane of the sky, rather than open, because Orion-S obscures it in the SW. It is clearly an ionization phenomenon since where [O III] is strong, [N II] is weak, but it is not an ionization boundary because there is no enhancement of [N II] on the outside. O'Dell et al. (2009) argue that inside the [O III] Shell is a region of lower gas density that results from the high-speed stellar wind from θ^1 Ori C. Sample B (Section 4.1) is our only spectroscopic sample of high S/N for the [O III] Shell. Its V_r([O III]) = 18.6 km s^{-1}, while our other samples average to 15.5 ± 2.6 km s^{-1} and García-Díaz et al. (2008) found a Huygens Region average of 16.3 ± 2.8 km s^{-1}. Our Sample B gave V_r([N II]) = 22.5, while our other samples average to 20.0 ± 1.9 km s^{-1} and García-Díaz et al. (2008) found a Huygens Region average of 20.5 ± 2.9 km s^{-1}. The small differences of velocity (one sigma high in both [O III] and [N II]) of the [O III] shell relative to the ambient gas agree with the models presented in O'Dell et al. (2009). The θ^1 Ori C collimated outflow shocks are generated within this inner zone of high ionization. They are much more visible in [O III], but some do have [N II] present on the concave side of the shocks.

Even farther there is a high-ionization feature similar to the [O III] shell in terms of its ionization properties. O'Dell et al. (2009) divide it into two portions: a curving bright [O III] feature that they call the Big Arc East (to the SE from θ^1 Ori C), and another longer and linear feature (the Big Arc South) beginning at the CW end of the Big Arc East and running nearly east–west. The portion of the latter directly south of θ^1 Ori C is at 69″ from θ^1 Ori C. Unlike the [O III] Shell, there is a region of [N II] enhanced emission associated with both the Big Arc and Big Arc East features, and the [N II]emission peaks farther from θ^1 Ori C, which is consistent with the expectations of photoionization.

In summary, we can say that while the inner systems of shocks must be related to a recent period of high-velocity wind from θ^1 Ori C, the much larger [O III] Shell was formed by an earlier period of a similar wind. θ^1 Ori C is well known to have strong variations in its spectrum and derived radial velocities. This makes it more plausible to interpret these two features as caused by two different periods of intense wind. The Big Arc

South and Big Arc East features are likely to be caused by an even earlier period of strong stellar winds from θ^1 Ori C.

As noted in Section 5.11, there are also shock features aligned with θ^1 Ori D. 156-256 at 34.″5 and 309° (plus a more symmetric shock 3″ outside it). θ^1 Ori D is quite different from θ^1 Ori C in that at spectral type O9.5V it is much cooler and the star lies close to the MIF. It is close to the Nye-Allen infrared source and shows unusually strong He I 388.9 nm absorption (O'Dell et al. 1993). θ^1 Ori C is a much hotter spectral type O6V star and lies about one-fourth of a parsec in front of the MIF. θ^1 Ori D is known to be a binary (Grellmann et al. 2013). If a collimated flow from θ^1 Ori D is real, it is the first known from a star in this temperature range.

7.10. Sources of the Outflows

A major goal of this program was to determine patterns in the outflows from young stars in the central part of the ONC. The intent of this was to see whether one can narrow down the properties of the stars with outflows in order to inform the process by which stars and protoplanetary disks are formed.

7.10.1. Sources of Outflows in This Study

It is worth examining the properties of the sources of the HH flows in order to establish patterns. Of the 31 flows where we have made an identification, there were 2 that had an ambiguity of the source and 1 (HH 626) that was not a source of collimated outflows, leaving 28 with single candidate sources. Of these, 11 were stars visible in the optical and 18 were COUP sources. This means that about one-third of the sources were not subject to heavy foreground extinction and two-thirds were young enough to be X-ray sources. Nine of the 10 visible sources were also COUP sources.

We would expect to find molecular outflows where there is high extinction; otherwise, the molecules would be photodissociated into atomic flows. If one sees an optical HH object arising from a molecular outflow, one may see features where the outflow passes through an ionization front. There are three known optical HH objects with molecular outflows driving them (EC 14 with the southwest shock, EC 13 [137-408] with HH 1147, COUP 555 with HH 625). HH 625 clearly appears to be passing through an ionization front. The HH 1132 outflow arising from COUP 632 also has the characteristics of collimated outflow passing through an ionization front, but there is no known associated molecular outflow.

In our study we identify COUP 666 with the large bipolar flow HH 202, HH 203 and HH 204, the multiple high-ionization shocks composing HH 529, and the linear feature HH 1129. The star is bright optically and is seen in X-rays and the infrared. None of the associated outflows show breakthrough features associated with passing through an ionization front, which indicates that their source is not imbedded. It is very important to study the optical spectrum of this star as it is the optically brightest candidate for the source of outflows.

7.10.2. Comparison of These Results with Those in an Earlier Study

Rivilla et al. (2013) recently reported a study intended to compare outflows in the Orion-S region with X-ray stars in the COUP list (Getman et al. 2005). Their sample came from within the north FOV area of our GO 12543 FOV, which means that we have high-quality optical data of the area they investigated. Their major emphasis was to establish whether the sources of molecular outflows determined from radio observations were also high-extinction COUP stars. They established that six of the seven sources were COUP stars, the only exception being EC 13 (135.7-408.2), which is seen only as a millimeter source. This establishes that COUP stars with high extinction can produce molecular outflows.

They then looked at whether the sources of optical HH objects were also COUP sources. For this purpose they used the positions of HH objects from a ground-based Fabry–Perot image published by Smith et al. (2004). That study identified only HH 202, HH 203, HH 204, HH 269, HH 528, HH 529, HH 530, and HH 625. As we have shown in this study, these HH objects are much more complex than indicated in the ground-based image they used, and the best available spatial resolution and derivation of motions are necessary to get accurate results. They concluded that HH 529 was driven by COUP 632 and argued more generally that the other outflows were driven by nonspecified high-extinction sources in Orion-S. As we have determined in the present study, the three previously known bow shocks in HH 529 are probably driven by COUP 666 rather than COUP 632. The sources we posit for the other HH objects they consider do lie within the Orion-S region, but the devil is in the details.

In their appendices they give an in-depth discussion of three well-studied and luminous sources in the Orion-S region (COUP 554, COUP 555, and COUP 632), all of which are sources of molecular outflows. In this study we identify COUP 555 as the probable source for HH 625. We identify COUP 632 as the source for HH 1142. We find no optical HH objects with COUP 554 as a source.

According to Rivilla et al. (2013), "Although some of the HH objects might be produced by stars of the ionized nebula ONC seen at optical wavelengths, it is expected that most of them are powered by stars still embedded in the dense molecular core in ONC1-S." This statement merits examination in the light of our new results. If this were rigorously true, one would not expect to detect sources of outflows in the visual, but in the preceding section we see that one-third of the identified sources were detected there.

Evidently the process of collimated stellar outflow can occur both in a high-extinction region like Orion-S and also in a region of low-density ionized gas. The presence of X-ray emission also occurs in optically visible stars, and this cannot be used as proof that the Orion-S sources are younger.

7.11. Summary of the Conclusions

We have found that our new data have allowed identification of the source of most of the optical outflows. In the case of the seven molecular outflows, three of these can be related to optical outflows, one of which (HH 625) clearly has the characteristics of breaking through an ionization front. We have also found that a significant fraction of the outflows not related to molecular outflows have optically visible sources. This argues that the period of collimated outflows survives even though the star lies in an ionized region. There are two regions from which outflows seem to originate that do not have a candidate source that is currently identified. Multiple shocks diverging from a single source are not uncommon, indicating that some stars have outflows directed in many directions, at different but similar times. This explains why many apparently aligned outflows are always blueshifted.

Table 6
Tangential Velocities[a]

Position Designation	PA(°) [O III] …	V_T [O III][a] …	PA (°) [N II] …	V_T[N II][a] …
053-509	317	98	…	…
053-509	318	115	…	…
053-510	341	83	…	…
057-516	319	50	…	…
065-343	…	…	284	27
076-343	…	…	265	93
077-342	296	67	…	…
077-343	…	…	284	64
077-343	…	…	284	69
077-344	…	…	266	88
077-348	284	59	…	…
077-348	…	…	256	51
078-345	…	…	266	75
079-343	284	30	…	…
085-531	…	…	320	25
090-339	284	21	…	…
090-340	274	52	302	39
094-336	296	61	…	…
096-329	274	59	…	…
097-345	…	…	279	32
096-346	…	…	270	48
096-347	…	…	254	47
098-330	250	65	…	…
098-412	…	…	212	15
101-329	252	68	…	…
102-330	…	…	233	15
102-416	279	69	…	…
103-313	279	67	…	…
103-418	…	…	198	18
104-417	…	…	274	28
105-325	257	24	…	…
106-322	284	47	…	…
106-325	…	…	265	26
107-314	276	38	…	…
107-322	309	28	…	…
107-342	272	49	…	…
107-430	…	…	232	25
108-307	278	96	…	…
108-418	111	65	…	…
108-430	…	…	246	34
108-430	…	…	246	34
109-313	…	…	296	28
109-321	…	…	299	40
109-323	302	31	…	…
109-426	…	…	259	30
109-430	…	…	232	25
109-430	…	…	232	25
109-431	…	…	255	50
110-321	…	…	298	26
110-345	…	…	264	26
110-346	…	…	270	42
110-347	…	…	242	37
110-347	…	…	270	33
110-351	…	…	286	29
110-416	…	…	262	95
110-423	…	…	248	27
110-423	…	…	333	15
110-423	…	…	248	27
112-320	…	…	333	24
112-324	…	…	284	32
112-349	…	…	298	41
111-323	…	…	302	40
111-347	250	43	…	…

Table 6
(Continued)

Position Designation	PA(°) [O III] …	V_T [O III][a] …	PA (°) [N II] …	V_T[N II][a] …
112-351	…	…	262	16
112-352	…	…	252	19
112-423	…	…	237	27
113-324	…	…	69	50
113-324	…	…	282	50
113-324	37	97	…	…
113-346	…	…	284	40
113-400	277	15	…	…
113-422	…	…	176	21
113-357	260	50	…	…
113-422	…	…	176	21
114-421	…	…	195	18
114-421	…	…	208	12
114-422	…	…	208	12
115-352	…	…	293	26
115-359	…	…	276	29
116-327	…	…	242	17
116-332	279	30	…	…
116-344	298	40	…	…
116-346	269	48	…	…
116-348	279	54	…	…
116-352	…	…	282	38
116-356	289	20	…	…
116-359	277	29	269	28
116-359	272	30	272	30
116-417	…	…	225	35
117-342	…	…	284	23
117-400	…	…	279	29
117-401	…	…	297	18
118-320	288	27	…	…
118-346	278	46	279	53
118-348	261	81	…	…
119-400	297	18	…	…
119-415	…	…	215	22
120-414	…	…	242	27
121-325	…	…	275	16
121-353	…	…	257	11
121-408	211	14	…	…
122-319	338	21	…	…
123-402	259	12	…	…
123-408	208	19	…	…
123-552	…	…	240	15
124-405	…	…	201	17
125-316	318	22	…	…
125-405	…	…	169	17
125-406	230	18	239	19
125-548	…	…	238	14
126-346	…	…	270	40
126-403	…	…	192	37
126-403	…	…	239	6
127-403	…	…	246	23
130-433	232	15	…	…
130-544	…	…	290	11
132-342	256	38	258	26
133-342	245	70	255	40
133-344	308	43	…	…
133-352	…	…	282	20
134-353	244	26	…	…
135-332	…	…	265	21
135-347	319	39	…	…
135-352	…	—75	15	
136-317	…	…	296	159
136-428	213	14	…	…

Table 6
(Continued)

Position Designation	PA(°) [O III] …	V_T [O III][a] …	PA (°) [N II] …	V_T[N II][a] …
136-508	…	…	6	13
136-353	…	…	278	15
137-351	…	…	280	14
137-352	…	…	271	49
137-408	…	…	155	25
137-514	…	…	150	37
138-254	…	…	275	10
138-350	…	…	257	33
138-519	…	…	191	41
139-350	251	15	273	15
139-353	…	…	276	15
139-516	…	…	190	30
141-421	342	18	342	20
141-425	234	30	…	…
142-356	349	9	…	…
142-357	24	6	…	…
142-358	21	8	…	…
143-325	275	24	…	–
143-351	…	…	284	8
143-357	43	12	…	…
143-418	9	19	…	…
143-428	197	36	227	18
148-354	…	…	239	15
149-352	…	…	104	101
149-354	…	…	129	95
149-356	241	38	…	…
151-351	17	34	…	…
LV 151-353	…	107	85	
151-356	…	…	187	9
151-359	…	…	244	19
152-353	89	87	…	…
152-354	…	…	106	96
152-358	…	…	201	20
153-359	255	44	…	…
154-305	320	58	…	…
154-305	325	62	…	…
154-328	…	…	246	16
154-344	…	…	225	10
154-401	…	160	25	
155-327	254	39	305	13
157-327	246	38	…	…
155-354	257	13	…	…
158-324	290	38	…	…
158-326	276	38	…	…
158-333	39	5	…	…
166-308	23	78	…	…
178-328	132	161	…	…
179-326	106	64	…	…
182-336	159	37	…	…
183-327	106	74	…	…
184-329	90	68	…	…

Note.
[a] Velocities are in km s^{-1}.

The late Robert H. Rubin, our colleague of many years, was the original Principal Investigator of *HST* program GO 12543, which produced the primary images used in this study. He was a career-long student of the Orion Nebula and the physical processes occurring in ionized nebulae. He made many contributions in his numerous research papers, and his presence at professional meetings was always a source of pleasure and stimulation.

In this study we have made extensive use of the SIMBAD database, operated at CDS, Strasbourg, France, and its mirror site at Harvard University.

We are grateful to the referee, Professor John Bally, for his helpful comments on this paper. G.J.F. acknowledges support by NSF (0908877; 1108928; and 1109061), NASA (10-ATP10-0053, 10-ADAP10-0073, and NNX12AH73G), JPL (RSA No 1430426), and STScI (*HST*-AR-12125.01, GO-12560, and *HST*-GO-12309). M.P. received partial support from CONACyT grant 129553. W.J.H. acknowledges financial support from DGAPA–UNAM through project PAPIIT IN102012. C.R.O.'s participation was supported in part by *HST* program GO 12543.

Facilities: HST (WFC3).

APPENDIX A
ERRORS IN POSITION COMPILATIONS

During the examination of the stars within Figure 39, it was noted that a star at 5:35:15.76, −5:23:38.4 is not listed in any of the sources summarized in SIMBAD. The closest star is COUP 734 (5:35:15:73, −5:23:37.9), which is 0.″67 to the NW. Our new star (257.6–338.4) is present on both the first- and second-epoch images within 0.″04, and the discrepancy cannot be explained as its being of high tangential velocity.

The source DR 1186 was reported as seen in ground-based images by Da Rio et al. (2009). It was not detected in previous visual images and does not appear in GO 12543 F547M images. Similarly, it does not appear in the *HST* Legacy Program catalog of visual and NIR images compiled by Robberto et al. (2013). It should be noted that in their image of the inner Orion Nebula (Figure 11 of Robberto et al. 2013) the stars and the nebula are in registration, but the coordinate scales shown are in error.

In the examination of our new images we noted two stars in the Da Rio et al. (2009) list that are probably mistaken positions for nearby stars. Their star 305 (5:35:10.71, −5:23:46.1) is probably Hillenbrand & Carpenter (2000) 224 (5:35:10.73, −5:23:44.6). Their star 1814 (5:35:11.77, −5:23:53.4) is probably the star designated in Hillenbrand & Carpenter (2000) as 205 (5:35:11.70, −5:23:51.3) and in Robberto et al. (2013) as 3405 (5:35:11.73, −5:23:51.7).

APPENDIX B
NEW TANGENTIAL VELOCITIES IN THE HUYGENS REGION

The tangential velocities determined from *HST* images are presented in Table 6.

APPENDIX C
RADIAL VELOCITIES OUTSIDE THOSE OF THE MIF

The radial velocities of features not directly associated with the MIF are presented in Table 7, using data from the spectroscopic Atlas.

APPENDIX D
USING THE STRENGTH OF LINES TO ANALYZE HH 1149

It is in the ratio of signals of different emission-line components of the high-resolution spectra that the greatest deviations occur. Therefore, we derived the ratio of different

Table 7
Radial Velocities outside Those of the MIF

Position Designation	V_r ([O III])[a] …	V_r ([N II])[a] …
106-310	−24	…
106-337	−45	…
106-416	−52	…
108-315	−18	…
108-343	−40	…
108-351	+2	…
108-413	−49	…
109-314	−20	…
109-323	…	−4
109-345	−39	…
109-351	…	+2
110-322	…	−5
110-345	−40	…
112-323	…	−4
112-346	−41	…
113-324	…	−12
113-348	−40	…
114-348	−40	…
114-426	+5	…
115-323	−32	…
117-309	−20	…
117-319	−31	…
117-354	−39	…
118-345	…	0
119-309	−54	…
121-310	−55	…
121-327	−25	…
121-334	−34	…
121-336	−23	…
122-314	−20	…
122-315	−58	…
122-437	…	+25
123-313	−21	…
123-315	−19	…
123-358	−58	…
123-323	−17	…
123-337	−30	…
123-428	−19	…
125-317	−56	…
125-319	−16	…
125-428	−17	…
126-319	−53	…
126-320	−13	…
126-338	−28	…
126-342	−30	…
126-346	−45	…
126-348	−29	…
126-419	−33	…
126-429	−19	…
127-318	−11	…
127-321	−46	…
127-338	−27	…
127-341	−33	…
127-342	−38	…
127-344	−45	…
127-347	−46	…
127-348	−22	…
129-320	−14	…
129-325	−43	…
129-339	−29	…
129-341	−34	…
129-342	−39	…
129-344	−41	…

Table 7
(Continued)

Position Designation	V_r ([O III])[a] …	V_r ([N II])[a] …
129-347	−43	…
130-327	−43	…
130-333	−37	…
130-339	−31	…
130-340	−33	…
130-341	−38	…
130-344	−44	…
131-329	−39	…
131-342	−36	…
133-330	−36	…
133-341	−35	…
134-232	−34	…
134-339	−34	…
134-429	−35	…
135-316	−41	…
135-333	−30	…
135-401	−47	…
135-432	…	−37
137-315	…	−100
137-330	−30	…
137-335	−20	…
137-337	−32	…
137-348	−32	…
138-317	−38	…
138-333	−30	…
138-340	−32	…
139-318	−37	…
139-321	−23	…
139-332	−25	…
139-336	−28	…
139-340	−31	…
139-346	−21	…
139-433	−32	…
141-318	−34	…
141-319	−45	…
141-324	−21	…
141-332	−22	…
141-336	−26	…
141-342	−32	…
141-347	−34	…
142-328	−37	…
142-329	−21	…
142-330	−23	…
142-427	−22	…
143-327	−35	…
143-339	−40	…
143-425	−18	…
143-427	−24	…
145-330	−44	…
145-338	−43	…
145-344	−31	…
146-331	−41	…
147-324	−8	…
147-333	−32	…
147-354	…	−42
147-428	−20	…
149-323	−19	…
149-324	−25	…
149-326	−42	…
149-353	…	−40
149-355	…	−42
150-324	−25	…
150-333	−27	…

Table 7
(Continued)

Position Designation	V_r ([O III])[a]	V_r ([N II])[a]
	...	...
150-352	−44	...
150-354	...	−42
151-323	−30	...
151-326	−7	...
151-336	−15	...
151-354	...	−41
151-352	−45	...
151-353	−48	...
153-323	−30	...
153-326	−4	...
153-336	−16	...
153-354	...	−42
153-355	−47	...
154-322	−25	...
154-339	−13	...
154-355	−53	−45
154-404	−8	...
155-323	−25	...
155-341	−15	...
155-355	−53	−45
155-426	−14	...
157-337	+93	...
157-339	−16	...
157-356	−44	−38
158-324	+82	...
158-332	−30	...
158-337	−27	...
158-339	+67	...
158-359	−32	...
159-351	−36	...
159-353	−29	−25
159-423	+24	...
161-343	+122	...
161-353	−33	...
161-354	−24	−27
162-328	−11	...
162-343	+103	...
162-352	−16	...
162-353	−39	...
163-326	−39	...
163-338	+70	...
163-343	+95	...
163-355	−8	...
163-359	−6	...
163-403	−4	...
163-455	−67	...
165-358	−22	...
165-405	−4	...
166-400	−28	...
166-358	...	−33
167-327	+25	...
167-358	...	−27
167-359	−30	...
169-339	−9	...
169-359	−29	−22
170-328	+115	...
170-330	+108	...
170-332	+110	...
170-337	+151	...
170-339	−4	...
170-3256	−18	...
170-357	−31	...
171-336	−37	...

Table 7
(Continued)

Position Designation	V_r ([O III])[a]	V_r ([N II])[a]
	...	...
171-339	−54	...
173-339	+52	...
173-339	−57	...
174-336	−40	...
174-345	−51	...
176-332	+5	...

Note.
[a] Velocities are in km s^{-1}, heliocentric. Subtract −18.1 km s^{-1} for LSR.

components for the various samples. The signal units (S) as we have measured them are in arbitrary units (numerous normalizations have been made since extracting the data from the Atlas). The results for this signal study are also shown in Table 3. Unfortunately, in the [O III] NEAR sample the association of the line components is unclear.

If the standard blister model applies, the ionization ratio of [O III] to [N II] is expected to decrease with the distance from θ^1 Ori C. The MIF signal ratio is S([O III])/S([N II]) = 0.29 for SHOCKS and 0.44 for NEAR if the 9.7 km s^{-1} and 20.9 km s^{-1} components are added together (if only the 20.9 km s^{-1} component is counted, the signal ratio is 0.08). These are the not the types of changes expected in moving outward from θ^1 Ori C, indicating that the two nearby samples are quite different regions. The average of five of the large samples (without C and D) is 0.60 ± 0.11, and the average of C and D is 0.06 ± 0.02. This indicates that the signals from C and D come from lower-ionization zones than the other large samples. This is consistent with their both being near where jets are producing shocks in the foreground Veil. The SHOCKS sample is significantly lower than the large samples, while the NEAR is closer to the SHOCKS sample than the Large Samples. The NEAR sample 20.9 km s^{-1} component ratio is much closer to the values of samples C and D, and the 9.7 km s^{-1} component is closer to the large samples without C and D.

For the HH 1149 samples the [N II] S(BLUE-[N II])/S(MIF-[N II]) ratios are similar for SHOCKS (0.02) and NEAR (0.06). This ratio is 0.07 ± 0.05 for the average of all the large samples, except for sample E, where the value is a deviant 0.15 (sample E falls on a foreground high-extinction feature, which may be the cause). We can conclude that the NEAR sample is coming from a region similar to the greater part of the Huygens Region and that the SHOCKS sample deviates in that the BLUE component is anomalously weak.

The differences are greater when examining the BLUE [O III] values using the S(BLUE-[O III])/S(MIF-[O III]) ratios. In the SHOCKS sample this ratio is 0.06. Only four of the large samples could be averaged, giving 0.17 ± 0.09. For the two large samples (A and G) lying on the Orion-S molecular cloud the ratio was 0.21 and 0.29. Sample-C's value was much greater than unity and probably indicates that the LOW component is actually the result of being on the edge of the HH 204 shock. Sample-D had no identifiable LOW [O III] component. Sample B, which lies in the high-ionization zone of O'Dell et al. (2009), had a value of only 0.02. The SHOCKS sample value of 0.06 is well less than the average of the four samples but much higher than in Sample B. These

numbers indicate that the [O III] BLUE component in the SHOCKS sample including HH 1149 is intermediate in value from most of the large samples and the high-ionization sample B.

As noted above, the NEAR [O III] line profile is divided into three components. The component at 9.7 km s^{-1} has a relative signal of 1.00, the 20.9 km s^{-1} is weaker at 0.09, and the backscattered 33.4 km s^{-1} has a signal ratio of 0.12. If the 9.7 km s^{-1} component is the blue component, then S(BLUE-[O III])/S(MIF-[O III]) is highly anomalous at 11.2. If the 9.7 km s^{-1} component is the MIF component, then the ratio is 0.0.

D.1 Testing the Methodology Using V_r

Several tests of the association of the SHOCKS and NEAR velocity components with similar components can be made. The first are the V_r values. The V_r values for the strong MIF emission in the individual large samples are probably accurate to better than 2 km s^{-1}. Variations between the samples can be larger than this because of local variations. Except when the BLUE component is strong compared with the MIF component, the V_r values of the weak individual BLUE components are probably accurate to about 4 km s^{-1}.

All of the V_r values for the MIF in SHOCKS and NEAR are similar to the averages of the large samples (Table 3), except for the NEAR [O III] sample. In the case of the weak SHOCKS-BLUE [N II] component, its value of −4.7 km s^{-1} is only slightly different from that for the large samples (1.3 ± 2.5 km s^{-1}). The NEAR-BLUE [N II] value 2.9 km s^{-1} is closer to that of the large samples. The SHOCKS-BLUE [O III] velocity of 1.1 lies within the scatter of the four large samples. At 9.7 km s^{-1} for the bluer NEAR [O III] component, this strongest feature is more positive than the other BLUE components (2.6 ± 2.2 km s^{-1}).

D.2 Testing the Methodology Using V_r Differences

Another test is the difference in velocity of the [O III] and the [N II] MIF components. This difference is due to material flowing through the PDR into the MIF and becoming more highly ionized on the θ^1 Ori C side of the PDR. The average V_r([O III])–V_r([N II]) for the seven large samples is −4.5 ± 1.6 km s^{-1}. This can be compared with −4.9 km s^{-1} and −10.3/−0.1 km s^{-1} in the SHOCKS and NEAR samples, respectively. The SHOCKS V_r difference is similar to the seven large samples, but the NEAR sample differs either high or low according to the assignment of its components, again pointing to a special nature of the nebula in this region.

D.3 Testing the Methodology Using Derived PDR V_r Values

A final test is that the average of the MIF and the Red scattered-light component should equal the velocity of the PDR (V_r(PDR)), within the approximation of fitting the Red component to a single Gaussian line. For our seven big samples V_r(PDR) was 27.2 ± 2.9 km s^{-1}, in good agreement with the OMC velocity (25.8 km s^{-1}). V_r(PDR) was 29.8 km s^{-1} and 28.0 km s^{-1} for SHOCKS in [N II] and [O III], respectively. V_r(PDR) was 29.1 km s^{-1} for NEAR in [N II], indicating that for the SHOCKS sample the MIF and RED components are correctly identified in [N II]. In the case of the NEAR [O III] sample the shorter (9.7 km s^{-1}) and longer (20.9 km s^{-1}) components give V_r(PDR) values of 21.6 km s^{-1} and 25.1 km s^{-1}, respectively, which argues that the longer and weaker component is due to the MIF. The signal ratio S(Red-[N II])/S(MIF-[N II]) is 0.06 and 0.07 for SHOCKS and NEAR, while it is 0.13 ± 0.04 for the average of the Big Samples, so that both regions have weaker [N II] Red components than the surrounding region. S(Red-[O III])/S(MIF-[O III]) is 0.10 and 0.12/1.38 for the SHOCKS and NEAR samples, respectively, whereas it is 0.10 ± 0.04 for the Big Samples. This means that the SHOCKS sample is indistinguishably the same as the Big Samples in both ions, and in the SHOCKS sample the agreement is only in [N II]. By the criterion of the Red-to-MIF flux ratio, the NEAR 9.7 km s^{-1} component is more likely the MIF feature, in contradiction with the V_r(PDR) results.

All the above indicates that we cannot clearly identify the sources of the two shorter velocity components of the NEAR [O III] features.

In a study now in progress we find multiple other regions with strong, even dominant, [O III] BLUE velocity components having velocities that associate them with the BLUE velocity components that are seen throughout the Huygens Region. These strong [O III] BLUE velocity areas must be samples of the material seen throughout the nebula but are under different conditions of illumination by θ^1 Ori C. They can also be the result of forward scattering from previously undetected material. The multiple shocks that constitute HH 1149 appear to be encroaching on one of these peculiar areas.

REFERENCES

Abel, N. P., Ferland, G. J., O'Dell, C. R., Shaw, G., & Troland, T. H. 2006, ApJ, 644, 344
Balick, B., Gammon, R. H., & Hjellming, R. M. 1974, PASP, 86, 616
Bally, J., Cunningham, N. J., Moeckel, N., et al. 2011, ApJ, 727, 113
Bally, J., Johnstone, D., Joncas, G., Reipurth, B., & Mallén-Ornelas, G. 2001, AJ, 122, 1508
Bally, J., Licht, D., Smith, N., & Walawender, J. 2005, AJ, 129, 355
Bally, J., Licht, D., Smith, N., & Walawender, J. 2006a, AJ, 129, 362
Bally, J., Licht, D., Smith, N., & Walawender, J. 2006b, AJ, 131, 473
Bally, J., Mann, R. K., Eisner, J., et al. 2015, APJ, 808, 69
Bally, J., O'Dell, C. R., & McCaughrean, M. J. 2000, AJ, 119, 2919
Bally, J., & Reipurth, B. 2001, ApJ, 546, 299
Blagrave, K. P. M., Martin, P. G., & Baldwin, J. A. 2006, ApJ, 644, 1006
Cantó, J., Goudis, C., Johnson, P. G., & Meaburn, J. 1980, A&A, 85, 128
Cantó, J., & Raga, A. C. 1996, MNRAS, 280, 559
Cantó, J., Raga, A., Steffen, W., & Shapiro, P. 1998, AJ, 502, 695
Colgan, S. W. J., Schultz, A. S. B., Kaufman, M. J., Erickson, E. F., & Hollenback, D. J. 2007, ApJ, 671, 536
Costero, R., Allen, C., Echevarría, J., et al. 2008, RMxAA (Serie de Conferencias), 34, 102
Currie, D. G., Dowling, D. M., Shaya, E. J., et al. 1996, AJ, 112, 1115
Cutri, R. M., Skrutskie, M. F., van Dyke, S., et al. 2003, yCat, 2246, 0
Da Rio, N., Robberto, M., Soderblom, D. R., et al. 2009, ApJS, 183, 261
Doi, T., O'Dell, C. R., & Hartigan, P. 2002, AJ, 124, 445
Doi, T., O'Dell, C. R., & Hartigan, P. 2004, AJ, 127, 3456
Eisner, J. A., & Carpenter, J. M. 2006, ApJ, 641, 1162
Feibelman, W. A. 1976, PASP, 88, 677
Feigelson, E. E., Broos, P., Gaffney, J. A., III, et al. 2002, ApJ, 574, 258
Felli, M., Taylor, G. B., Catarzi, M., Churchwell, E., & Kurtz, S. 1993, A&AS, 101, 127
Fukue, T., Tamura, M., Kandori, R., et al. 2009, ApJL, 692, L88
Furuya, R. S., & Shinnaga, H. 2009, ApJ, 703, 1198
García-Díaz, Ma.-T., & Henney, W. J. 2007, AJ, 133, 952
García-Díaz, Ma.-T., Henney, W. J., López, J. A., & Doi, T. 2008, RMxAA, 44, 181
Getman, K. V., Flaccomio, E., Broos, P. S., et al. 2005, ApJSS, 160, 319
Grellmann, R., Preibisch, T., Ratzka, T., et al. 2013, A&A, 550, A82
Güdel, M., Briggs, K. R., Montmerle, T., et al. 2008, Sci, 319, 309
Gustafsson, M., Kristensen, L. E., Clénet, Y., et al. 2003, A&A, 411, 437

Hartigan, P., Morse, J. A., Reipurth, B., Heathcote, S., & Bally, J. 2001, ApJL, 559, L157
Henney, W. J. 1994, ApJ, 429, 288
Henney, W. J., & Arthur, S. J. 1998, AJ, 116, 322
Henney, W. J., García-Díaz, Ma. T., O'Dell, C. R., & Rubin, R. H. 2013, MNRAS, 428, 691
Henney, W. J., O'Dell, C. R., Meaburn, J., Garrington, S. T., & Lopez, J. A. 2002, ApJ, 566, 315
Henney, W. J., O'Dell, C. R., Zapata, L. A., et al. 2007, AJ, 133, 2343
Herbig, G. H., & Griffen, R. F. 2006, AJ, 132, 1763
Herbst, W., Bailer-Jones, C. A. L., Mundt, R., Meisenheimer, K., & Wackermann, R. 2002, A&A, 396, 513
Hillenbrand, L. A. 1997, AJ, 113, 1733
Hillenbrand, L. A., & Carpenter, J. M. 2000, ApJ, 540, 236
Hillenbrand, L. A., Hoffer, A. S., & Herczeg, G. J. 2013, AJ, 146, 85
Howarth, I. D., & Prinja, R. K. 1989, ApJS, 69, 527
Hu, X. 1996, AJ, 112, 2712
Jones, B. F., & Walker, M. F. 1988, AJ, 95, 1755
Kaify, N., Usuda, T., Hayashi, S. S., et al. 2000, PASJ, 52, 1
Kraus, S., Weigelt, G., Balega, Y. Y., et al. 2009, A&A, 497, 195
Kristensen, L. E., et al. 2003, A&A, 412, 727
Lada, C. J., Muench, A. A., Haisch, K. E., Jr., et al. 2000, AJ, 120, 3162
Lada, C. J., Muench, A. A., Lada, E. A., & Alves, J. F. 2004, AJ, 128, 1254
Laques, P., & Vidal, J. L. 1979, A&A, 73, 97
Lee, J.-K., & Burton, M. G. 2000, MNRAS, 315, 11
Lehman, H., Vitrichenko, E., Bychko, V., Bychkova, L., & Klochkova, V. 2010, A&A, 514, A34
Luhman, K. L., Rieke, G. H., Young, E. T., et al. 2000, ApJ, 540, 1016
Massey, R. M., & Meaburn, J. 1995, MNRAS, 273, 615
McCaughrean, M. J., & Mac Low, M.-M. 1997, AJ, 113, 391
McCaughrean, M. J., & O'Dell, C. R. 1996, AJ, 111, 1977
McCaughrean, M. J., & Stauffer, J. R. 1994, AJ, 108, 1382
Mesa-Delgado, A., Esteban, C., García-Rojas, J., et al. 2009a, MNRAS, 395, 855
Mesa-Delgado, A., López-Martín, L., Esteban, C., García-Rojas, J., & Luridiana, V. 2009b, MNRAS, 394, 693
Mesa-Delgado, A., Núñez-Díaz, M., Esteban, C., López-Martín, L., & García-Rojas, J. 2011, MNRAS, 417, 420
Morse, J. A., Hartigan, P., Cecil, G., Raymond, J. C., & Heathcote, S. 1992, ApJ, 399, 231
Morse, J. A., Heathcote, S., Cecil, G., Hartigan, P., & Raymond, J. C. 1993, ApJ, 410, 764
Muench, A. A., Lada, E. A., Lada, C. J., & Alves, J. 2002, ApJ, 573, 366
Munch, G., & Wilson, O. C. 1962, ZA, 56, 127
Nutter, D., & Ward-Thompson, D. 2006, MNRAS, 374, 143
O'Dell, C. R. 2000, AJ, 119, 2311
O'Dell, C. R. 2001, ARA&A, 39, 99
O'Dell, C. R., & Doi, T. 2003a, AJ, 125, 277
O'Dell, C. R., & Doi, T. 2003b, AJ, 125, 2753
O'Dell, C. R., Ferland, G. J., Henney, W. J., & Peimbert, M. 2013a, AJ, 145, 92
O'Dell, C. R., Ferland, G. J., Henney, W. J., & Peimbert, M. 2013b, AJ, 145, 170
O'Dell, C. R., & Harris, J. A. 2010, AJ, 140, 985
O'Dell, C. R., Hartigan, P., Bally, J., & Morse, J. A. 1997a, AJ, 114, 2016
O'Dell, C. R., Hartigan, P., Lane, W. M., et al. 1997b, AJ, 114, 730
O'Dell, C. R., & Henney, W. J. 2008, AJ, 136, 1566
O'Dell, C. R., Henney, W. J., Abel, N. P., Ferland, G. J., & Arthur, S. J. 2009, AJ, 137, 367
O'Dell, C. R., Muench, A., Smith, N., & Zapata, L. 2008, in Handbook of Star Forming Regions: The Northern Sky, Vol. 1, ed. B. Reipurth (San Francisco, CA: ASP), 544
O'Dell, C. R., Valk, J. H., Wen, Z., & Meyer, D. M. 1993, ApJ, 403, 678
O'Dell, C. R., Walter, D. K., & Dufour, R. J. 1992, ApJL, 399, L67
O'Dell, C. R., & Wen, Z. 1994, ApJ, 436, 194
O'Dell, C. R., & Wong, S.-K. 1996, AJ, 111, 846
O'Dell, C. R., & Yusef-Zadeh, F. 2000, AJ, 120, 382
Olivares, J., Sánchez, L. J., Ruelas-Mayorga, A., et al. 2013, AJ, 146, 106
Osterbrock, D. E., & Ferland, G. J. 2006, Astrophysics of Gaseous Nebulae and Active Galactic Nuclei (2nd ed.; Mill Valley, CA: Univ. Science Books)
Plambeck, R. L., Wright, M. C. H., Friedel, D. N., et al. 2009, ApJL, 704, L25
Prisinzano, L., Micela, G., Flaccomio, E., et al. 2008, ApJ, 677, 401
Raga, A. C., & Noriega-Crespo, A. 2013, RMxAA, 49, 363
Reipurth, B., Bally, J., Graham, J. A., Lane, A. P., & Zealy, W. J. 1986, A&A, 164, 51
Ricci, L., Robberto, M., & Soderblom, D. R. 2008, AJ, 136, 2136
Rivilla, V. M., Martín-Pintado, J., Sanz-Forcada, J., Jiménez-Serra, I., & Rodríguez-Franco, A. 2013, MNRAS, 434, 2313
Robberto, M., Beckwith, S. V. W., Panagia, N., et al. 2005, AJ, 129, 1534
Robberto, M., Soderblom, D. R., Bergeron, E., et al. 2013, ApJS, 207, 10
Rodríguez, L. F., Poveda, A., Lizano, S., & Allen, C. 2005, ApJL, 627, L65
Rodríguez-Ledesma, M. V., Mundt, R., & Eisloeffel, J. 2009, A&A, 502, 883
Rosado, M., de la Fuente, E., Arias, L., & le Coarer, E. 2002, RMxAA, 13, 90
Schmid-Burgk, J., Guyesten, R., Mauersberger, R., Schulz, A., & Wilson, T. 1990, ApJL, 362, L25
Schultz, A. S. B., Colgan, S. W. J., Erickson, E. F., Kaufman, M. J., & Hollenbach, D. J. 1999, ApJ, 511, 282
Schulz, N. S., Canizares, C., Huenemoerder, D., et al. 2001, ApJ, 549, 441
Shuping, R., Bally, J., Morris, M., & Throop, H. 2003, ApJL, 587, L109
Simon, M., Close, L. M., & Beck, T. L. 1999, AJ, 117, 1375
Smith, N., Bally, J., Shuping, R. Y., Morris, M., & Hayward, T. L. 2004, ApJ, 610, 117
Stanke, T., McCaughrean, M. J., & Zinnecker, H. 2002, A&A, 392, 239
Takami, M., Usuda, T., Sugai, J., et al. 2002, ApJ, 566, 910
Tan, J. C. 2004, ApJL, 607, L47
Throop, H. B., Bally, J., Esposito, L. W., & McCaughrean, M. J. 2001, Sci, 292, 1686
Tobin, J. J., Hartmann, L., Furesz, G., Mateo, M., & Megeath, T. 2009, ApJ, 697, 1103
van Altena, W. F., Lee, J. T., Lee, J. F., et al. 1988, AJ, 95, 1744
van der Werf, P., Goss, W. M., & O'Dell, C. R. 2013, ApJ, 762, 101
Vannier, L., Lemaire, J. L., Field, D., et al. 2001, A&A, 366, 651
Vitrichenko, E. A. 2002, AstL, 28, 324
Walsh, J. R. 1982, MNRAS, 201, 561
Walter, D. K. 1994, PASP, 106, 106
Walter, D. K., O'Dell, C. R., Hu, X., & Dufour, R. J. 1995, PASP, 107, 686
Zapata, L. A., Ho, P. T. P., Rodríguez, L. F., et al. 2006, ApJ, 653, 398
Zapata, L. A., Loinard, L., Schmid-Burgk, J., et al. 2011, ApJL, 726, L12
Zapata, L. A., Rodríguez, L. F., Ho, P. T. P., et al. 2005, ApJL, 630, L85
Zapata, L. A., Rodríguez, L. F., Kurtz, S. E., & O'Dell, C. R. 2004a, AJ, 127, 2252
Zapata, L. A., Rodríguez, L. F., Kurtz, S. E., O'Dell, C. R., & Ho, P. T. P. 2004b, ApJL, 610, L121
Zapata, L. A., Rodríguez, L. F., Schmid-Burk, J., et al. 2012, ApJL, 754, L17
Zapata, L. A., Schmid-Burk, J., Ho, P. T. P., Rodríguez, L. F., & Menten, K. M. 2009, ApJL, 704, L48
Zapata, L. A., Schmid-Burk, J., Muders, D., et al. 2013, A&A, 510, A2
Zuckerman, B. 1973, ApJ, 183, 863